Aerodynamic Control of a Vehicle with Flexible Longitudinal Mode

by

Edward Kenneth Walters II

Submitted to the Department of Aeronautics and Astronautics
in partial fulfillment of the requirements for the degree of

Master of Science in Aeronautics and Astronautics

at the

MASSACHUSETTS INSTITUTE OF TECHNOLOGY

May 1993

Author .....
Department of Aeronautics and Astronautics
May 7, 1993

Certified by .....
Eugene E. Covert
T. Wilson Professor of Aeronautics
Thesis Supervisor

Certified by .....
Dr. Michael Judd
Work Supervisor
Thesis Supervisor

Accepted by .....
Professor Harold Y. Wachman
Chairman, Departmental Committee on Graduate Students

Aerodynamic Control of a Vehicle with Flexible Longitudinal Mode

by

Edward Kenneth Walters II

Submitted to the Department of Aeronautics and Astronautics
on May 7, 1993, in partial fulfillment of the
requirements for the degree of
Master of Science in Aeronautics and Astronautics

Abstract

The use of flexible mode control implemented through the use of aerodynamic surfaces is examined for two case vehicles: a magnetically levitated vehicle and a towed aerodynamic vehicle. A summary of the aerodynamics of trapezdoial and annular wings is presented first, followed by an analysis of the modal characteristics of the test vehicles. LQR design methods using the flexible mode and its rate as states are then applied to both cases, with damping of the flexible mode as the result. Modal control is concluded to be an effective and viable method controlling the flexibility of a vehicle.

Thesis Supervisor: Eugene E. Covert
Title: T. Wilson Professor of Aeronautics

Thesis Supervisor: Dr. Michael Judd
Title: Work Supervisor

Acknowledgements

There are a number of people that I would like to thank for their help with this work:

Professor Covert, whose sage advice and realistic view kept me upon the straight and narrow path.

All of the staff at the Aerospace Engineering Group at Lincoln Laboratory, for all their gracious help and support, and for giving me the opportunity to intern there in the first place.

Jamie Burnside, without whom I would not have a clue as to modelling the dynamics of the maglev vehicle, and for his helpful technical support.

Dr. Michael Judd, for his patience with me and care taken in the proofreading of this document.

To my mother, father, and sister, for all their wonderful support and understanding.

And finally, to Kathy, for putting up with me all this time.

Contents

List of Figures

List of Tables

List of Symbols

A	Effective Center of Gravity of Lumped Mass Aft Body
A	Roll Moment of Inertia
$\mathbf{A}$	System State Matrix
A_n	Circulation Distribution Constant
AR	Aspect Ratio
AR_n	$= 8r/\pi c$, Modified Annular Aspect Ratio
a	Vortex Radius
a_f	Forward Acceleration Due to Slope or Curve
a_h	Horizontal Acceleration Due to Slope or Curve
a_v	Vertical Acceleration Due to SLope or Curve
a_0	Radius of Vortex Location at $x = 0$
B	Complete Vehicle Pitch Moment of Inertia About CG
$\mathbf{B}$	Control Transmission Matrix
B_A	Pitch Moment of Inertia of Aft Body About P
B_1	$= B_1 + m_A c_1 c_3$, Net Aft Body Pitch Inertia
b	Wing Span
b_a	Distance Between Downwash Vortex Pair
b_n	Propulsion Coil Gap Deviation of n_{th} Magnet
C	Cable Attachment Point for Towed Body
C	Yaw Moment of Inertia
$\mathbf{C}$	Output Transmission Matrix
C_D	Coefficient of Drag

C_{D_i} Coefficient of Induced Drag

C_{L_α} $= \frac{dC_L}{d\alpha}$, Lift-Curve Slope

$C_{L_{\alpha B}}$ Body Lift-Curve Slope

C_l Sectional Lift Coefficient

c Wing Chord

c_f Flap Chord Length

c_r Root Chord Length

c_s Local Chord Length

c_t Tip Chord Length

c_1 Distance Between Cable Attachment Point and CG

c_2 Distance Between CG and Flexible Point

c_3 Distance Between Flexible Point and Aft Body CG

D_A Aerodynamic Drag

D_M Magnetic Drag

D_v Net Towed Vehicle Steady Drag

d Distance from Vortex to Wing

d_n Distance from n_{th} Vortex to Subject Vortex

dN Incremental Normal Lift on Strip

F Towing Force

G Non-Deformed Body Center of Gravity

$\mathbf{G}$ LQR Gain Matrix

g Acceleration Due to Gravity

h Distance Between Downwash Vortex Pair

h_n Levitation Coil Gap Deviation of n_{th} Magnet

h_0 Nominal Levitation Coil Gap

J Quadratic Cost Functional

$\mathbf{K}$ CARE Solution Matrix

k Torsional Spring Constant

k_{DL} Magnetic Lift-to-Drag Ratio at Reference Velocity

L	Lift
$\mathbf{L}$	Disturbance Transmission Matrix
L_A	Aerodynamic Roll Moment
L_M	Magnetic Roll Moment
L_v	Net Towed Vehicle Steady Lift
l_b	Center of Lift Distance from the CG for the Body
l_w	Wing Surface Moment Arm
l_{wr}	Wing Surface Roll Moment Arm
l_{xcn}	Relative x-Position of n_{th} Levitation Magnet
l_{xc0}	Relative x-Position of n_{th} Levitation Magnet from Center
l_{xpn}	Relative x-Position of n_{th} Propulsion Magnet
l_{xc0}	Relative x-Position of n_{th} Levitation Magnet from Center
l_y	Distance From Center of Body to AHS
l_z	Distance From Center of Body to APVS/ASVS
l_1	Average Moment Arm for Modified Aerodynamic Model
l_2	Roll Moment Arm for Modified Aerodynamic Model
M	Aerodynamic Pitching Moment
M_A	Aerodynamic Pitch Moment
M_A	Aft Body Aerodynamic Pitching Moment About P
$M_{A_{aft}}$	Aft Body Aerodynamic Moment About CG
M_C	Aft Body Control Induced Moment About CG
M_M	Magnetic Pitch Moment
$M_{M_{aft}}$	Aft Body Magnetic Moment About CG
M_S	Torsional Spring-Induced Torque
m	Complete Vehicle Mass
m_A	Aft Body Mass
m_0	Two-Dimensional Lift-Curve Slope
m_{0s}	Local Lift-Curve Slope
N_A	Aerodynamic Yaw Moment

N_M Magnetic Yaw Moment

n_L Number of Lift Magnets

n_P Number of Propulsion Magnets

P Effective Center of Rotation for Bending Mode

p Roll Rate

p_0 Roll Rate Command

$\mathbf{Q}$ State Weighting Matrix

q Pitch Rate

q_0 Pitch Rate Command

R Body Radius

R Magnetic Center Radius

$\mathbf{R}$ Control Weighting Matrix

r Yaw Rate

r Annular Wing Radius

r_n Radius from n_{th} Vortex to Subject Vortex

r_0 Yaw Rate Command

S Effective Wing Surface Area

S_B Body Reference Area

S_R Aerodynamic Body Reference Area

S_w Wing Surface Area

s Wing Half-Span

s Distance from Magnetic Center to CG

s_A Distance from Magnetic Center to Aerodynamic Center

T Total Magnetic Propulsive Thrust

T_0 Nominal Forward Propulsion Control Force

u x-Direction (Forward) Velocity

$\mathbf{U}$ Control Vector

u_R Reference Longitudinal Velocity

u_g Forward Gust Velocity

u_i Tangential Velocity Induced by i_{th} Vortex

u_n Tangential Velocity Induced by n_{th} Vortex

u_0 Forward Velocity Command

V Annular Wing Strip Virtual Velocity

V_{in} Normal Downstream Vortex Induced Velocity

V_{it} Tangential Downstream Vortex Induced Velocity

V_n Normal Velocity

V_∞ Free Stream Velocity

v Lateral Velocity

v_g Lateral Gust Velocity

v_i Induced Sidewash Velocity

v_0 Lateral Velocity Command

w z-Direction (Vertical) Velocity

w_F Towed Vehicle Gust Velocity

w_g Vertical Gust Velocity

w_i Induced Downwash Velocity

w_0 Vertical Velocity Command

X Lumped x-Direction Aerodynamic Force

x Forward Position

x Downstream (Chordwise) Coordinate

$\mathbf{x}$ State Vector

x_0 Downstream Location

Y_A Aerodynamic Lateral Force

Y_M Magnetic Lateral Force from Lift Magnets

Y_{mk} Magnetic Lateral Force from Magnetic Keel

y Lateral Position

y Spanwise Coordinate

$\mathbf{y}$ Output Vector

y_t Lateral Track Roughness

y_0 Spanwise Lift Location

y_0 Distance Vortex Moves in y-Direction

yb_n Lateral Displacement of n_{th} Propulsion Magnet

Z Lumped z-Direction Aerodynamic Force

Z_A Aerodynamic Lift

Z_M Magnetic Lift

z Vertical Position

z_T Vertical Track Roughness

z_p Vertical Propulsion Roughness

z_0 Distance Vortex Moves in z-Direction

α Angle of Attack

α_T Wing Twist Distribution

α_a Absolute Angle of Attack

α_i Induced Angle of Attack

α_n Actual Angle of Attack

α_p Angle of Pitch Moment Control Surface

α_{ro} Angle of Roll Moment Control Surface

α_y Angle of Lateral Force Control Surface

α_{ya} Angle of Yaw Moment Control Surface

α_z Angle of Vertical Force Control Surface

α_{0l} Zero Lift Angle of Attack

Γ Circulation

Γ_n Strength of n_{th} Vortex

Γ_s Circulation at Wing Center

Γ_0 Downwash Circulation Strength

γ Angle Between Absolute Horizontal and Cable Direction

δ Angular Deflection of Aft Body Relative to Vehicle Centerline

ϵ Induced Angle of Attack

ϵ_L Levitation Stiffness Coefficient

ϵ_P Propulsion Stiffness Coefficient

η Dimensionless Spanwise Coordinate

η Control Surface Deflection

η_f Flap Angle

θ Pitch Angle

θ Annular Wing Strip Angle

θ Span-wise Angle

θ Vortex Angle

θ_{cn} Angle of n_{th} Levitation Magnet Off of Centerline

θ_c Scalar Angle of Magnet Off of Centerline

λ $= c_t/c_r$, Taper Ratio

λ_f Flap-Chord Ratio

μ Monoplane Equation Coefficient

ν Deflection Rate

ξ Flexible Mode Control Surface Deflection

ρ Ambient Aerodynamic Density

τ Flap Effectiveness Factor

ϕ Roll Angle

ϕ Annular Wing Strip Virtual Angle of Attack

ϕ Trapezoidal Wing Spanwise Angle

ϕ Vortex Complementary Angle

ϕ_0 Roll Angle Command

ψ Yaw Angle

ψ Angle at which Induced Velocity Acts

ω_B Natural Bending Frequency of Maglev Vehicle

Chapter 1

Introduction

1.1 Background

An important problem that aerospace engineers have been facing within recent years is the problem of controlling a vehicle that is not considered to be a rigid body, i.e. possesses one or more flexible modes. Several approaches have been devised to attempt to take this into account when designing the control system, such as considering the wings of an aircraft to be a series of masses and connecting weights and springs, where the control system takes the modes of these structural dynamics into account [1], [2], or trying to uncouple the flutter dynamics of an aircraft from its pitching mode [3]. A large and expanding range of applications have been considered and used. At the simplest level, the control system stability margins can be improved. At a higher level, the response of flexible wings to gusts and turbulence can be alleviated, with reduction of fatigue stresses and improvement in pilot and passenger ride comfort. At a sophisticated level, all these factors can be combined at the aircraft design stage to produce a minimum weight structure and optimal mission performance. This involves a large number of state space variables and a method for incorporating design variables into the control cost function. However, it is possible to investigate the subject of modal control and observe its basic properties without resorting to unwieldy models and massive numerical analysis by considering the basic modal properties of a simple system, and applying a modern feedback control methodology that takes the

modes into account [4]. It is the aim of this thesis to show that this is feasible by applying an optimal controller to two examples that differ in application, but have modal properties that are similar.

1.2 Optimal Control

During the past ten years, a number of new control techniques have been devised that enable the engineer to influence phenomena that would otherwise have remained unchecked. Such techniques include the use of state-space formulations to reduce equations involving large numbers of degrees-of-freedom into a form conducive to computational analysis, the use of optimal control theory to find a "best" method of controlling phenomena, the use of robust control theory to allow a control system to function in the presence of modelling errors [5], and the use of $\mathcal{H}_\infty$ design to enable a system to react to unknown disturbances in a causal manner [6]. Optimal control is one aspect of this set of theories that possesses the ability to regulate states with a minimum of effort on the part of the control system. The optimal control design methodology used here is the Linear Quadratic Regulator (LQR) design method. A controller obtained using this technique operates upon a state-space system to bring all of the state values to zero from non-zero initial states and in the presence of disturbances. This effect is produced through the formulation of a quadratic cost function that weights the effects of different states and controls, and uses this function to obtain the optimum gains from the states to the controls [5]. The LQR methodology presents itself as an ideal method for modal control because it forces the deflections to go to zero if they are considered among the states, thus damping the vibrations present in the system that are caused by the flexible modes.

1.3 Modal Control Considerations in Flexible Vehicles

In many control situations, it is adequate to consider only the rigid body dynamics. However, often the vehicle in question is flexible enough to raise concerns about the degree of deformation and the effect it has on the structure and dynamics of the vehicle. This is where the application of a modal control system can be advantageous. A modal control system can be defined as a control system that takes into account, i.e. includes among its states, the flexible modes of a vehicle or body. In many modern aerospace and transportation applications, the bodies in question have one dimension that is much greater than the other two. Examples of such configurations include slender missles and high aspect ratio aircraft wings. The deflection that the bodies undergo takes place normal to the longest axis. If the frequency of the flexible mode or modes is near that of the rigid body modes and within the control system frequency bandwidth, the feedback gain and phase margins could be significantly reduced. Therefore, the need for a modal control system for the control of certain vehicles becomes an important consideration when dealing with these types of bodies.

An implication of modal control is that all of the stated variables must be observable (or at least detectable), and that the vehicle has the actuators for independent control of these states. Also, an important point to address with respect to modal control concerns how many modes need to be incorporated into the control system. In many cases only the primary mode need be considered, as the higher order modes possess negligible deflections or are excited at frequencies that are outside of the operating bandwidth of the vehicle and are lightly damped. An LQR controller requires full state feedback, and it may not be possible to measure all of the higher-order modes and their rates with a limited number of sensors. In addition, the effects of flexible modes can sometimes be mitigated by the use of a passive filter on the feedback loop. As a result it was decided that only the lowest order flexible mode would be considered, and the resulting deflection and its rate would be incorporated into the state-space vector used in the control system design.

The LQR technique is applied here in two applications, both of which are characterized by slender bodies with a longitudinal flexible mode. The first application is the improvement of passenger ride quality for a high speed magnetically levitated ground transport vehicle. The second relates to the maneuverability of an aerodynamic body being towed behind an aircraft. The general geometry of each vehicle is presented in Chapter 2. In both applications, aerodynamic control surfaces are used, and the first part of the thesis (Chapter 3) presents the assessments made of their aerodynamic properties. Chapter 3 also contains analyses concerning the modal properties of each vehicle, along with a summary of the controller design technique. Chapter 4 presents a summary of the simulations that were run to determine the validity of the modal control systems, while Chapter 5 contains the results of these tests. Chapter 6 provides a summary of the work performed and any conclusions reached.

Chapter 2

Practical Examples

There are many examples of vehicles that would benefit from the use of modal control, but most of the work performed in this thesis dealt with two example vehicles: a magnetically levitated high speed ground transport (maglev) vehicle, and a towed aerodynamic vehicle. In both these examples, the aerodynamic characteristics of the vehicle were dominant in providing system damping and in providing the force and moment mechanisms (through control surfaces) in the feedback control loops. Therefore, the aerodynamic properties were first evaluated for inclusion in the control, design, and simulation stages and comparison with existing aerodynamic models.

2.1 Magnetically Levitated Vehicle

The majority of the work performed on this type of vehicle was applied to a specific configuration: the Magneplane vehicle [4]. However, the work can be easily generalized to any ground vehicle that uses the same mode of propulsion and includes aerodynamic surfaces for purposes of stability augmentation. The Magneplane vehicle is a high speed train that is propelled above its track using a series of levitation and propulsion coils. The levitation system consists of a magnetically repulsive system where the vehicle rides roughly six inches above a rounded track bed. The vehicle is propelled forward by an electromagnetic travelling wave that originates at the departing station and is boosted periodically by coils distributed along the track. Therefore,

during the time when the vehicle is moving, the bottom of the vehicle never comes into physical contact with the track. As a result, if no external forces are added, the only damping forces that act on the vehicle are those produced by the magnetic interactions with the track and those produced aerodynamically by the body motions. It was found that although the system is stable, these damping interactions were not sufficient to keep vibrations caused by track roughness, wind gusts, etc. below accepted ISO standards, and it was determined that additional damping using airfoils and rate feedback was needed [4].

The airfoils on the Magneplane vehicle (see Figure 2-1) were designed to provide an additional degree of stability to the vehicle while insuring that the amount of propulsive energy needed by the vehicle was not increased by an exorbitant amount. The lifting surfaces on the Magneplane vehicle consisted of a full-wing at the fore end of the vehicle, a half-wing extending out of the top of the fore end of the vehicle, and a box wing at the aft end of the vehicle. These lifting surfaces were located far from the center of gravity of the vehicle so as to maximize their dampening effect on the vehicle angular dynamics.

In addition, the dimensions of the vehicle and the location of the magnetic supports results in a low bending frequency (see Figure 2-1 again), indicating that a certain amount of modal control might be needed to control the deflections of the vehicle. The implementation of such a control scheme would also require the use of the airfoils mentioned above, with the possibility that an additional control surface would be needed to compensate for the presence of another state and ensure that the system was stabilizable.

The design of such a control system for the rigid vehicle was carried out using a six degree-of-freedom computer simulation developed by Burnside [4]. The simulation performed the following tasks: using track and disturbance data as input, the simulation derived linear state-space equations from the original non-linear equations of motion, and applied LQR theory to obtain a compensator that would regulate all of the perturbation states. As the track and disturbance inputs were time-varying, the simulation made "snapshots" of the dynamics of the system, reevaluating them

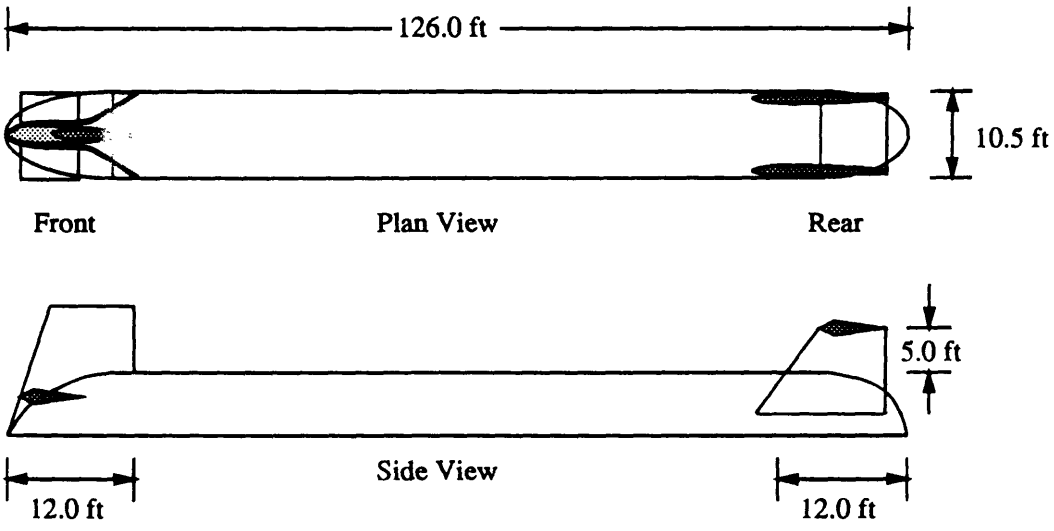

Figure 2-1: Magneplane Vehicle

for each time step, and using the resulting states to determine the states at the next time step. Although this model proved to be quite adequate for the purposes it was created for, there were certain aspects of it that required further work to insure that the control system would be adequate for the final vehicle.

The first modification that was required was a re-examination of the aerodynamic properties assumed for the control surfaces. In the first model, the control surfaces were present as lumped parameters with simplified aerodynamic representations. More complex aerodynamic theory might help give a more accurate picture of the control surface capabilities. It was thus decided that the work detailed here should begin with a summary of the aerodynamics of the different control surfaces of the vehicle, with an emphasis on obtaining relatively simple closed-form expressions that could be eventually incorporated into the model. These closed form expressions could also be used in a more general sense, where they could be applied to any arrangement of lifting surfaces.

The second modification required redesigning the simulation to include regulation

of the longitudinal flexible mode in the control scheme. This would be accomplished by extending the scope of the simulation from six to seven degrees-of-freedom, and providing tests and special cases to determine whether or not the system was needed, or if so, whether or not it managed to control the extra state, reduce the vehicle response to track roughness, and improve ride quality. An additional topic concerning the simulation also involved the addition of the analytic expressions concerning the aerodynamics that were derived in the first step to the model dynamics. As it was decided that this modification would only make a complex model more complex, the analytical results instead would be compared to the aerodynamic terms present in the simulation to determine their accuracy.

2.2 Towed Aerodynamic Vehicle

The towed flight vehicle was another example of a vehicle configuration that could profit from both a re-analysis of its aerodynamics properties and the application of modal control. The towed vehicle (see Figure 2-2) possessed a layout similar to that of the maglev vehicle in that it was a long, thin cylinder with lifting surfaces positioned on the fore and aft parts of the body. The difference between the two was in the application: while the maglev vehicle was designed as a ground-based vehicle, the towed vehicle was designed as a lifting body that was propelled by being pulled from an aircraft. The lifting surfaces of the towed vehicle would be used to maneuver the body in relation to the aircraft. The aerodynamic characteristics of the body were required for use in the design of the control system to modify the towed body stability and its maneuverability.

The basic aerodynamics of the towed vehicle were needed in analytical form so they could be included in the control simulation. Although the original configuration of the towed vehicle involved cruciform wings, it was decided that an annular wing configuration, as seen in Figure 2-2, would provide superior aerodynamic performance; the aerodynamic analysis performed on the towed vehicle would consist exclusively of an annular wing analysis.

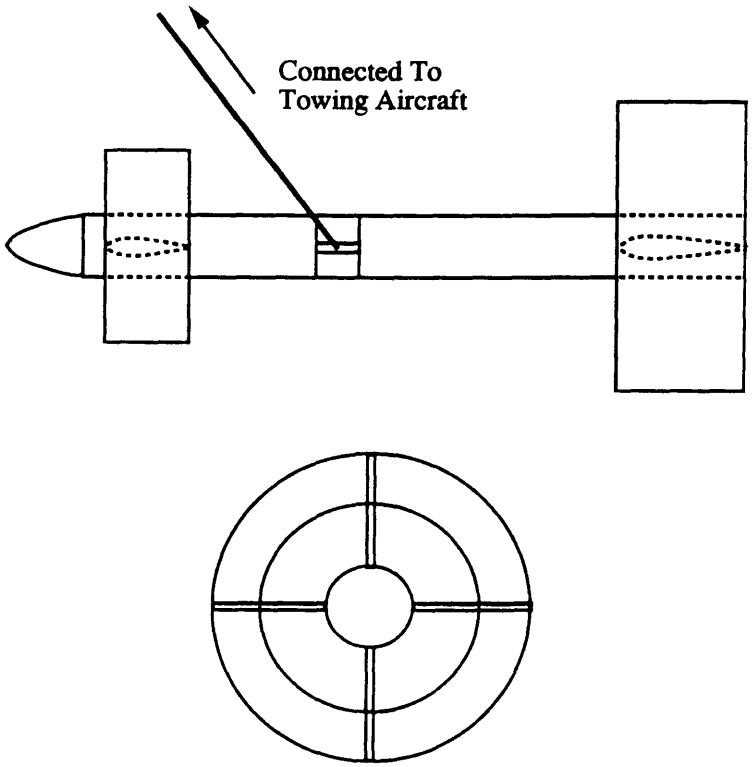

Figure 2-2: Towed Vehicle

Due to its long, thin body and the location of the lifting surfaces, it was also felt that a modal control analysis would be appropriate for the towed vehicle. The resulting control system design would be of the same form, i.e. a Linear Quadratic Regulator, and would be implemented directly using the linearized state-space model of the system, as opposed to being incorporated into a large-scale non-linear simulation like the that of the Magneplane.

Chapter 3

Analysis and Theoretical Background

3.1 Introduction

The majority of the preliminary work performed on this thesis was composed of a detailed analysis of several aspects of vehicle aerodynamics and modal control considerations. Although not all of this analysis was explicitly incorporated into the simulations, it provided a valuable check on the accuracy of the expressions that were utilized within the control simulation.

3.2 Aerodynamic Analysis

The aim of the aerodynamic analysis was to obtain reasonably accurate expressions for the lifting characteristics of pertinent lifting surfaces without using computationally intensive methods. For the vehicles concerned, the two categories of lifting surfaces that were investigated encompassed trapezoidal (including rectangular) wings, generalized to box wings, and annular wings. Analysis procedures for each type of wing are detailed below.

General assumptions for the aerodynamic analysis were that the lifting surfaces in question were uncambered and untwisted, and the incident flow was considered

inviscid and incompressible. Justification for the flow assumptions came from the fact that the design speeds of both vehicles were sufficiently below the speed of sound, i.e. in the range of 150 m/s for the Magneplane and 100 m/s for the towed vehicle.

3.2.1 Trapeziodal and Box Wings

Three different types of analysis were performed on the trapezoidal wing configurations: a survey of the lifting characteristics of each wing, with the assumption that each wing was all-movable; a study of some of the wing-body and downwash interactions; and a summary of the effects of the addition of flaps to the structure of the wings. One important point to note, especially with respect to the box wings, was that interactions between the different sections of the box wing were not taken into effect, i.e. the three sections of the box wing were considered separately, ignoring interference effects. It was felt that this was a conservative position because the lift capability of each surface is underestimated as a result of neglecting the end plate effect.

Lifting Characteristics

When dealing with the trapezoidal surfaces present on the vehicles in question, there were two types of wing configurations that required attention: full wings and half wings. As can be seen in Figure 3-1, when considering the full wing, the body effect was ignored. As a result of this, the wing was considered to extend continuously through the body, and the effects of root gaps were ignored, i.e. the lifting surfaces were considered to be flush with the body, even if the surfaces could be adjusted to different angles of attack.

All of the trapezoidal wings dealt with in this analysis were of low aspect ratio (less than three), so it was decided that the following formula, obtained from [7] should be used to determine the lift curve slope C_{L_α} of each wing:

$$C_{L\alpha} = \frac{dC_L}{d\alpha} = m_0 \frac{AR}{AR\sqrt{1 + (m_0/\pi AR)^2} + m_0/\pi} \tag{3.1}$$

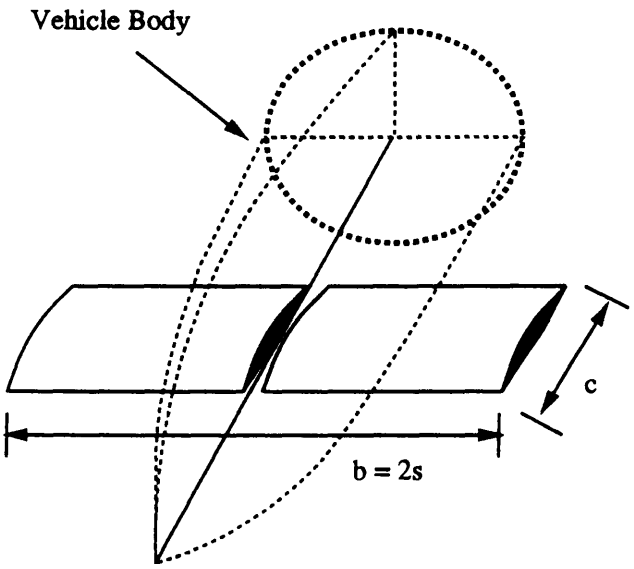

Figure 3-1: Full Wing

where AR is the aspect ratio and m_0 is the two-dimensional lift-curve slope, with a thin wing value of 2π. If the zero-lift line of the wing corresponds with the chord line of the wing, then the lift produced by each wing is given by

$$L = \frac{1}{2}\rho V_\infty^2 \mathcal{S} \frac{dC_L}{d\alpha}\alpha \tag{3.2}$$

where ρ is the ambient aerodynamic density, V_∞ is the free stream velocity, and the effective wing surface area is $\mathcal{S} = cs$.

These equations enable one to obtain the amount of lift produced by each lifting surface. However, in order to obtain the moments induced by each lifting surface, the location of the lift along the surface of each wing must be calculated so its location relative to the center of gravity of the vehicle, and therefore the moments, may be determined. In this analysis, two applications of lifting-line theory methods were used to find the lift locations: one pertaining to rectangular wings, and one pertaining to trapezoidal wings.

Rectangular Lifting Surfaces The rectangular wings considered here possess moderate aspect ratios, and conventional lifting-line theory can be used to compute coefficients of lift and induced drag with reasonably accurate results. The distribution of circulation over these surfaces must obey certain boundary conditions regardless of the shape of the wing; it must approach zero at the tips of the wing, and reach a maximum at the centerline of the wing. The arbitrary circulation distribution of lifting-line theory, as derived in [8], obeys these constraints, so it was deemed that the circulation of these moderate aspect-ratio surfaces could be considered to be of the same form as that of lifting-line theory in order to find the location of the lift along the span of the wing.

For purposes of the analysis here, the circulation Γ along the wing was considered to be continuous along the span (even if the two lifting surfaces were at different angles of attack) and of the form [8]:

$$\Gamma = \frac{1}{2} m_0 c V_\infty \sum_{n=1}^{\infty} A_n \sin(n\theta)$$

where y is the spanwise coordinate with its origin at the center of the wing, and $y = s\cos\theta$ (See Figure 3-2).

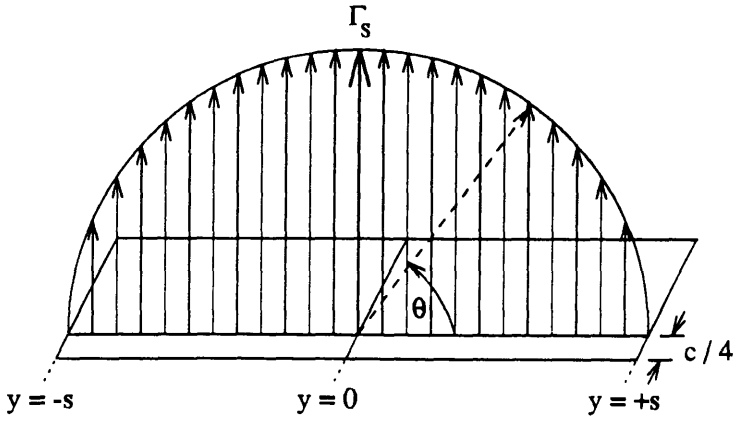

Figure 3-2: Elliptical Circulation Distribution

The absolute angle of attack along the span corresponding to this circulation distribution is

$$\alpha_a(\theta) = \frac{1}{m_0 c}\sum_{n=1}^{\infty} m_{0_s} c_s A_n \sin(n\theta) + \frac{1}{4b}\sum_{n=1}^{\infty} m_{0_s} c_s n A_n \frac{\sin(n\theta)}{\sin\theta}$$

where m_{0_s} is the local lift-curve slope and c_s is the local chord length. For rectangular lifting surfaces, $m_{0_s} = m_0 = 2\pi$ and $c_s = c$, and for an untwisted, uncambered wing, the expression reduces to

$$\alpha = \sum_{n=1}^{\infty} A_n \sin(n\theta) + \frac{2\pi c}{4b}\sum_{n=1}^{\infty} n A_n \frac{\sin(n\theta)}{\sin\theta} \tag{3.3}$$

In order to compute the circulation and therefore the lift distribution, the values of the constants A_n must be determined by evaluating the above equation at different stations along the span of the wing. In this analysis, only four constants will be computed (A_1, A_3, A_5, and A_7: assumed symmetric loading causes the even terms to disappear), so four stations will be taken. The stations are located at $\theta = \pi/8, \pi/4, 3\pi/8, \pi/2$.

If the four equations are generated by evaluating Equation (3.3) along each station are rearranged to be in matrix form, the result is

$$\mathbf{DA} = \alpha \tag{3.4}$$

where $\mathbf{D}$ is a j x n matrix, the terms of which are

$$D_{jn} = \left(1 + \frac{n\pi}{2AR\sin\theta_j}\right)\sin n\theta_j$$

where $j = 1, \ldots, 4$, $n = 1, 3, 5, 7$, and $\mathbf{A}$ and α are represented by

$$\begin{aligned} \mathbf{A} &= [A_1\ A_3\ A_5\ A_7]' \\ \alpha &= \alpha[1\ 1\ 1\ 1]' \end{aligned}$$

If $\mathbf{D}$ is not singular, then the solution to this equation is provided by

$$\mathbf{A} = \mathbf{D}^{-1}\alpha \tag{3.5}$$

Otherwise, if $\mathbf{D}$ is singular, then pseudo-inverse methods must be used to find an approximate solution.

The spanwise location of the lift is obtained from the equation

$$\frac{y_0}{s} = \frac{1}{C_L}\int_0^1 C_l \frac{y}{s} d\left(\frac{y}{s}\right)$$

where, y_0 is the spanwise lift location, and C_l is the sectional lift coefficient as given in [8]

$$\begin{aligned} C_l &= \frac{m_{0s}}{c} c_s \sum_{n=1}^{\infty} A_n \sin n\theta \\ &= 2\pi \sum_{nodd}^{7} A_n \sin n\theta \\ &= 2\pi\{A_1 \sin\theta + A_3 \sin 3\theta + A_5 \sin 5\theta + A_7 \sin 7\theta\} \end{aligned}$$

Now that C_l is known, the integral can be evaluated as follows

$$\begin{aligned} y &= \frac{1}{2} b \cos\theta \\ \frac{y}{s} &= \frac{\frac{1}{2}b}{s} \cos\theta = \cos\theta \\ d\left(\frac{y}{s}\right) &= -\sin\theta \end{aligned}$$

so,

$$\frac{y_0}{s} = \frac{2\pi}{C_L}\int_0^{\pi/2} (A_1 \sin\theta + A_3 \sin 3\theta + A_5 \sin 5\theta + A_7 \sin 7\theta)\cos\theta \sin\theta d\theta$$

The exact solution to this integral is

$$\frac{y_0}{s} = \frac{2\pi}{C_L}\left[\frac{A_1}{3} + \frac{A_3}{5} - \frac{A_5}{21} + \frac{A_7}{45}\right] \tag{3.6}$$

where C_L is the lift coefficient for an arbitrary symmetrical circulation, as given in [8]

$$\begin{aligned} C_L &= \frac{m_{0_s} c_s \pi b}{4s} A_1 \\ &= \frac{\pi^2}{2} A_1 \end{aligned}$$

Lifting-line theory also assumes that the lift acts at the quarter chord.

In summary, for the rectangular wings, the lift of each surface is given by the expression

$$L = \frac{1}{2}\rho V_\infty^2 S \frac{dC_L}{d\alpha}\alpha \tag{3.7}$$

and the lift is located at

$$x_0 = \frac{c}{4} \tag{3.8}$$

$$y_0 = \frac{4s}{\pi A_1}\left[\frac{A_1}{3} + \frac{A_3}{5} - \frac{A_5}{21} + \frac{A_7}{45}\right] \tag{3.9}$$

where x_0 is measured from the front of the wing, and y_0 is measured from the center of the wing. Numerically, if only the first term of the series for y_0 is considered, then the lift is located at $y_0 = 4s/3\pi = .424s$ from the center of the full wing. This result agrees with intuition, as it gives a lift position closer to the center than the wing end, in accordance with the circulation distribution described above.

Trapezoidal Wings The magnitude of the lift produced by the trapezoidal wings is given by the same expression as that of the rectangular wings, except that now the chord is a function of span and the spanwise variable θ.

A general configuration of the trapezoidal wing is given in Figure 3-3. According to lifting-line theory as given in [9], the chord-wise location of the lift is $c/4$, where the chord is a function of the spanwise coordinate. The spanwise location, on the other hand, is given by a form of the monoplane equation as given in [9]. The procedure used is as follows:

First, the spanwise coordinate must be redefined as $\frac{y}{s} = -\cos\phi$ for the sake of

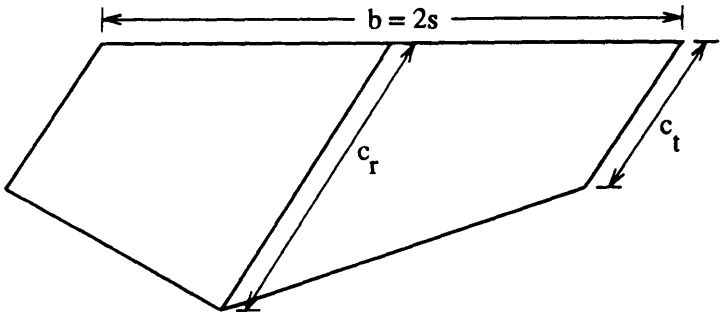

Figure 3-3: Trapezoidal Wing

convenience, and the general monoplane equation gives

$$\mu(\alpha - \alpha_{0l})\sin\phi = \sum_{n=1}^{\infty} A_n(\mu n + \sin\phi)\sin n\phi \tag{3.10}$$

where,

$$\mu = \frac{c(\phi)m_0}{8s}$$

and α_{0l} is the zero-left angle, which is assumed zero for an untwisted, uncambered wing. Now an expression for μ must be derived. The following terms are quantified in terms of the geometric quantities of the trapezoidal wing

$$\begin{aligned} AR &= \frac{2b}{c_r + c_t} \\ s &= \frac{c_r AR}{4}(1+\lambda) \end{aligned}$$

where λ is the taper ratio c_t/c_r. So, the expression for the chord as a function of the spanwise coordinate is

$$c(\phi) = c_r[1 + (\lambda - 1)\cos\phi]$$

and the resulting expression for μ is

$$\mu = \frac{m_0 c(\phi)}{8s}$$

$$= \frac{m_0}{2(1+\lambda)AR}[1 + (\lambda - 1)\cos\phi]$$

As with the example of the rectangular wing, the monoplane equation must be evaluated at a number of stations equal to the number of coefficients desired. In much the same way, four coefficients will be used, at the same stations as those used with respect to the rectangular wing. The equations take the form

$$\mu_j(\phi_j)\alpha \sin\phi_j = \sum_{n\ odd}^{7} A_n(n\mu_j + \sin\phi_j)\sin n\phi_j \tag{3.11}$$

and the resulting matrix equation is:

$$\mathbf{C}\alpha = \mathbf{B}\mathbf{A} \tag{3.12}$$

or,

$$\mathbf{A} = \mathbf{B}^{-1}\mathbf{C}\alpha \tag{3.13}$$

where,

$$\begin{aligned} C_j &= \mu_j \sin\phi_j \\ B_{jn} &= (n\mu_j + \sin\phi_j)\sin n\phi_j \\ A_n &= A_n \end{aligned}$$

from this one can obtain $A_1, \ldots, A_7$.

Now, from lifting-line theory and [9], it is known that the lift coefficient may be expressed in terms of these A_n's as

$$C_L = A_1 \pi AR \tag{3.14}$$

so, one has to return to the same equation that was used for the rectangular wing to determine where along the span the lift is located

$$\frac{y_0}{s} = \frac{1}{C_L}\int_0^{-1} C_l \frac{y}{s} d\left(\frac{y}{s}\right) \tag{3.15}$$

and from the transformation used above, it is known that

$$\begin{aligned} \frac{y}{s} &= -\cos\phi \\ d\left(\frac{y}{s}\right) &= \sin\phi d\phi \end{aligned}$$

so, the above equation becomes

$$\begin{aligned} \frac{y_0}{s} &= \frac{1}{C_L}\int_{\pi/2}^{0} -C_l \cos\phi \sin\phi d\phi \\ &= \frac{1}{C_L}\int_{0}^{\pi/2} C_l \cos\phi \sin\phi d\phi \end{aligned}$$

where, from [9]

$$\begin{aligned} C_l &= 2(AR)(1+\lambda)\frac{c_r}{c}\sum_{n=1}^{4} A_{2n-1}\sin(2n-1)\phi \\ &= \frac{2AR(1+\lambda)}{1+(\lambda-1)\cos\phi}\sum_{n=1}^{4} A_{2n-1}\sin(2n-1)\phi \end{aligned}$$

and the final result for the location along the span is

$$\begin{aligned} \frac{y_0}{s} &= \frac{2AR(1+\lambda)}{C_L}\int_{0}^{\pi/2}\frac{1}{1+(\lambda-1)\cos\phi}\sum_{n=1}^{4} A_{2n-1}\sin(2n-1)\phi\cos\phi\sin\phi d\phi \\ &= \frac{2}{\pi}(1+\lambda)\left[I_1(\phi)+\frac{A_3}{A_1}I_3(\phi)+\frac{A_5}{A_1}I_5(\phi)+\frac{A_7}{A_1}I_7(\phi)\right] \end{aligned}$$

where,

$$I_n(\phi) = \int_{0}^{\pi/2}\frac{\sin\phi\sin n\phi\cos\phi}{1+(\lambda-1)\cos\phi}d\phi$$

which must be integrated numerically. This expression gives the location of the lift along the span of the trapezoidal wing. Chordwise, the lift is located at $x = c/4$, where the value of c is dictated by the spanwise location of the lift. Specific numerical results can be found in the Results Section, but a typical numerical result, say for a wing with a taper ratio of $\lambda = .77$, and neglecting higher order terms, produces an $I_1 = .3859$, and a lift location of $y_0/s = .4348$ from the wing centerline.

Downwash Interactions

There are several miscellaneous effects that will have an effect on the aerodynamics of the body that were not taken into account by the above analysis. One of the most notable and easiest to account for is the interaction between the trailing vortices given off by the forward wing and the rear wing or wings. The interactions between the vortices and the body of the vehicle were also considered. The analytical procedure is as follows.

First of all, for purposes of determining the motion of the vortex without the effect of the body, the wing will considered to be complete and symmetrical with respect to its central axis, i.e. it will be a complete wing. It is assumed that the rear wings to be dealt with are far enough away from the front wing that the vortex sheet shed by the front wing has has more than enough time to roll up. Therefore, the rear wings will only see a line vortex, and that vortex will be considered locally straight with respect to the rear wings, i.e. the vortex-image and vortex-body interactions will change the inclination of the vortex and its location in the $y - z$ plane, but it can be considered perpendicular to the span of any wing being influenced by it. It was assumed that this roll-up has occured because the rear wings were several wing span-lengths in back of the front wing, and the available data from [10] suggests that this is a reasonable assumption.

As there is a complete wing present, a vortex of strength Γ_0 will be shed by each half-wing, and the distance between the two vorticies is given by h. These two quantities can be determined for each specific configuration later. Now, the vortex on each half-wing will be pushed down by the induced velocity of its mirror on the other side of the wing, and each vortex will be pushed down an equal amount, as they are of equal strength. The location of these vortices will vary in the $y - z$ plane as a function of x, and so will the downwash induced by these vortices. As can be seen in Figure 3-4, each vortex can be considered as semi-infinite, with the location being a function of x, the lengthwise coordinate.

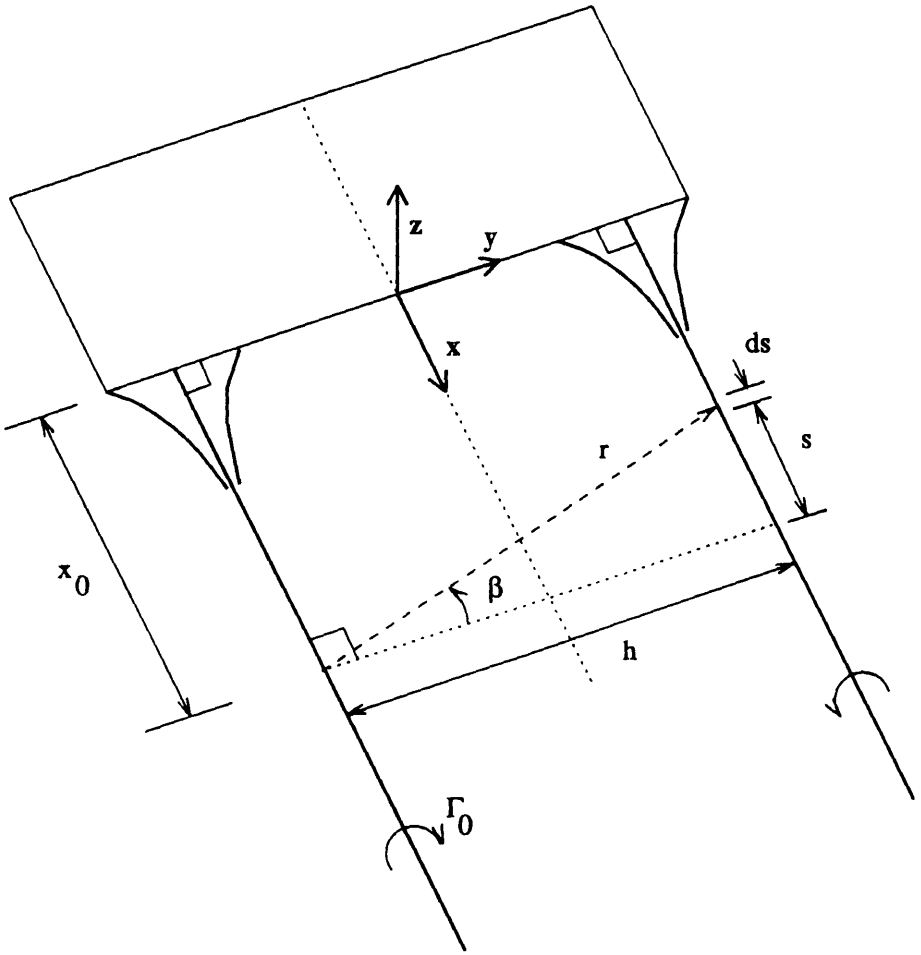

Figure 3-4: Downwash Vortex Geometry

For a semi-infinite vortex, the velocity w_i induced at the other vortex is given by:

$$x = 0, w_i = -\frac{\Gamma_0}{4\pi h}$$

and, for an infinite vortex, it is given by:

$$x = \infty, w_i = -\frac{\Gamma_0}{2\pi h}$$

For a section of the $y - z$ plane located at x_0, the velocity induced by the other vortex is:

$$w_i = -\frac{\Gamma_0}{4\pi} \int_{-\infty}^{x_0} \frac{\cos\beta}{r^2} ds \tag{3.16}$$

If we define, as in Figure 3-4,

$$\begin{aligned} r &= h\sec\beta \\ s &= h\tan\beta \\ ds &= h\sec^2\beta d\beta \end{aligned}$$

the resulting downwash velocity obtained through integration is:

$$\begin{aligned} w_i &= -\frac{\Gamma_0}{4\pi h}\left(1+\sin(\tan^{-1}\frac{x_0}{h})\right) \\ &= -\frac{\Gamma_0}{4\pi h}\left(1+\frac{x_0}{\sqrt{x^2+h^2}}\right) \end{aligned} \tag{3.17}$$

Another quantity to be considered is the distance that each vortex is pushed downward (in the $-z$ direction) due to the action of its mirror vortex. For the vortex to be aligned with the total flow direction, this distance can be approximated by the equation:

$$\epsilon = \frac{w_i(x)}{V_\infty} \approx \frac{dz}{dx} \tag{3.18}$$

with $z = 0$ when $x = 0$, and then:

$$\begin{aligned} z(x) &= \int_0^x \frac{dz}{dx_0}dx_0 \\ &= -\frac{\Gamma_0}{4\pi h V_\infty}\left[(x-h)+\sqrt{x^2+h^2}\right] \end{aligned} \tag{3.19}$$

The next step to take is analysis of the effect of the body on the behavior of the vortex. There are two configurations that can occur: asymmetric effect, which is due to the presence of a body and half wing, such as the foreward vertical control surface of the maglev vehicle, and, symmetric effect, which is due to the presence of a full wing and the body in the center of the wing.

The method that will be used to analyze the path of the vortex as it leaves the fore wing will be a method of circular images, as can be found in [11], [12]. A brief summary of the basic ideas of this theory follows.

Half Wing-Body Interactions In order to adapt this analysis to the form of a half-wing configuration, the coordinates will be altered so the vortex moves with respect to both the y- and z-axis as a function of downstream location. This will facilitate the use of Equation (3.17) to describe the vortex behavior for the example of the Magneplane vehicle. Equation (3.17) can be used for any vortex pair provided h is interpreted as the distance between the vortices, Γ_0 is the strength of the vortex which is inducing the velocity, and $w_i(x)$ is the velocity induced normal to the plane containing the vortices.

As can be seen in Figure 3-5, for this configuration there is a single wing extending in the $+z$-direction that produces a single vortex of strength Γ_0. The location of the vortex will change as a function of the x-coordinate as the vortex runs down the length of the body. The change in this position is caused by the effect of the vortex image system. The body is taken to have a circular cross-section and the origin for the y- and z-axes is on the centerline. In the method of images [11], [12], the body is modelled as two vortices: one that is of equal magnitude but opposite direction and located at the inverse point of the circle, and another that is of the same strength and direction as the first and located in the center of the body. The image vortex pair have zero net circulation and the real and image vortices together satisfy the velocity boundary condition at the cylinder wall. As can be seen in Figure 3-5, at the cylinder wall, the relation between the distances of the vortices from the center is given for all x by:

$$r_1 r_2 = R^2 \tag{3.20}$$

where r_1 is the distance between the central vortex and the inverse point vortex, r_2 is the distance between the central vortex and the real vortex, and R is the body radius.

In general, the velocities induced by the image vortices will cause the real vortex to move. As a result, the edge image vortex will also have to move to oppose the real vortex and preserve the body shape. The resulting interactive motions can be described using differential equations, which are derived as follows. General forms

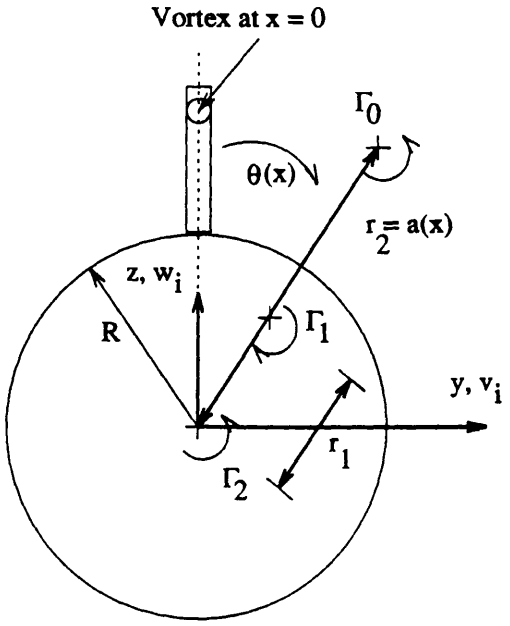

Figure 3-5: Half Wing-Body Configuration

will be used, but it can be seen from Figure 3-5 that the velocity induced on the external vortex must be purely tangential, and hence r_1 and r_2 will not vary with x.

The two variables, $a(x) = r_2$ and $\theta(x)$, are defined in Figure 3-5. The velocity induced by the n_{th} vortex on the point occupied by the real vortex is given by:

$$u_n = \frac{\Gamma_0}{4\pi d_n}\left(1 + \frac{x}{\sqrt{x^2 + d_n^2}}\right) \tag{3.21}$$

where d_n is the distance between the n_{th} vortex and the real vortex. If vortex Γ_1 and vortex Γ_2 are defined as in the Figure, the resulting d_1 and d_2 are given by:

$$\begin{aligned} d_1 &= a(x) - r_1 \\ d_2 &= a(x) \end{aligned}$$

and, from above,

$$\begin{aligned} r_1 a(x) &= R^2 \\ r_1 &= R^2/a(x) \end{aligned}$$

so,

$$d_1 = \frac{1}{a(x)}\left[a(x)^2 - R^2\right]$$

As a result, the tangential velocities induced at the external vortex have magnetudes given by:

$$u_1 = \frac{a\Gamma_0}{4\pi(a^2 - R^2)}\left(1 + \frac{x}{\sqrt{x^2 + (a^2 - R^2)/a^2}}\right) \tag{3.22}$$

$$u_2 = \frac{\Gamma_0}{4\pi a}\left(1 + \frac{x}{\sqrt{x^2 + a^2}}\right) \tag{3.23}$$

These velocities must be broken into their y and z components:

$$\begin{aligned} v_i(x) &= (u_1 - u_2)\cos\theta \\ w_i(x) &= -(u_1 - u_2)\sin\theta \end{aligned}$$

with Γ_0 positive in the counter-clockwise direction shown in Figure 3-5.

Once the velocities can be separated into their components, the differential equations for the vortex motion can be obtained using the equation for downwash:

$$\frac{dz}{dx} \doteq \frac{w_i(x)}{V_\infty} \tag{3.24}$$

and the equation for sidewash:

$$\frac{dy}{dx} \doteq \frac{v_i(x)}{V_\infty} \tag{3.25}$$

so, the resulting differential equations of motion are:

$$\frac{dy}{dx} = \frac{1}{V_\infty}(u_1 - u_2)\cos\theta \tag{3.26}$$

$$\frac{dz}{dx} = -\frac{1}{V_\infty}(u_1 - u_2)\sin\theta \tag{3.27}$$

The equations are converted using the transformations

$$\begin{aligned} y &= a\sin\theta \\ z &= a\cos\theta \end{aligned}$$

to obtain the polar forms:

$$\frac{da}{dx} = 0 \tag{3.28}$$

$$\frac{d\theta}{dx} = \frac{1}{V_\infty}(u_1 - u_2) \tag{3.29}$$

These are the equations of motion of the vortex produced by a half-wing taking the body of the vehicle into account. These equations can also be non-dimensionalized for scaling purposes, using $\bar{a} = a/R$, to make the substitutions:

$$\begin{aligned} \bar{d}_1 &= \frac{1}{\bar{a}}(\bar{a}^2 - 1) \\ \bar{d}_2 &= \bar{a} \\ \nu &= \frac{\Gamma_0}{4\pi R V_\infty} \end{aligned}$$

with the nondimensional equations becoming:

$$\frac{d\bar{a}}{d\bar{x}} = 0 \tag{3.30}$$

$$\frac{d\theta}{d\bar{x}} = \frac{\nu}{\bar{a}}\left(\frac{1}{\bar{d}_1}\left[1 + \frac{\bar{x}}{\sqrt{\bar{x}^2 + \bar{d}_1^2}}\right] - \frac{1}{\bar{d}_2}\left[1 + \frac{\bar{x}}{\sqrt{\bar{x}^2 + \bar{d}_2^2}}\right]\right) \tag{3.31}$$

Equation (3.30) confirms that $\bar{a}$ is a constant, so that the vortex will just move around the body at a constant radius. There are no forces to oppose the tangential movement of the vortex, so, if the body is long enough, the vortex will eventually spiral around the body. An interesting consequence of this is that the vortex could possibly miss the rear set of wings by a substantial distance, thus contributing nothing to the downwash

effects. It is up to tests of the actual configurations to determine whether or not this will be the case.

Full Wing-Body Interactions When the wing is considered to extend out of both sides of the body, the problem becomes slightly more complex. The movement of both vortices that are shed must be traced, but if the body and the wings are symmetric the problem reduces to finding the path of one of the votex, as the other will follow a path that is symmetric with respect to the $z - x$ plane.

In this analysis, the wing to be considered will be a full wing extending in the $\pm y$ direction, as can be seen in Figure 3-6. Each wing will shed a vortex of strength Γ_0 but of opposite direction at a distance $h/2$ from the $z - x$ plane. The procedure for deriving the equations of motion for the vortices is very similar to that of the half-wing analysis above, again using the method of images. Each real external vortex has two image vortices, located as before at the center of the body and at the inverse point. However, because the external vortices have equal but opposite directions, the image vortices at the center of the body cancel each other and have no influence.

As before, the velocities induced by the virtual vortices will cause the real vortices to move as one proceeds downstream. This will, in turn, force the virtual vortices to move to the corresponding inverse points in order to preserve the shape of the body. These motions are the basis for the differential equations that describe the motions of the vortex system.

Unlike the above half-wing system, each real vortex will feel the induced velocities of three other vortices: its mirror vortex inside the body, the other real vortex on the opposite side of the body, and the mirror vortex of the other real vortex, also located within the body. Once again the two variables that will be used to describe the motion are $a(x)$ and $\theta(x)$, and as before, the velocity induced on one of the real vortices by the n_{th} other vortex is given by the expression:

$$u_n = \frac{\Gamma_0}{4\pi d_n}(1 + \frac{x}{\sqrt{x^2 + d_n^2}}) \tag{3.32}$$

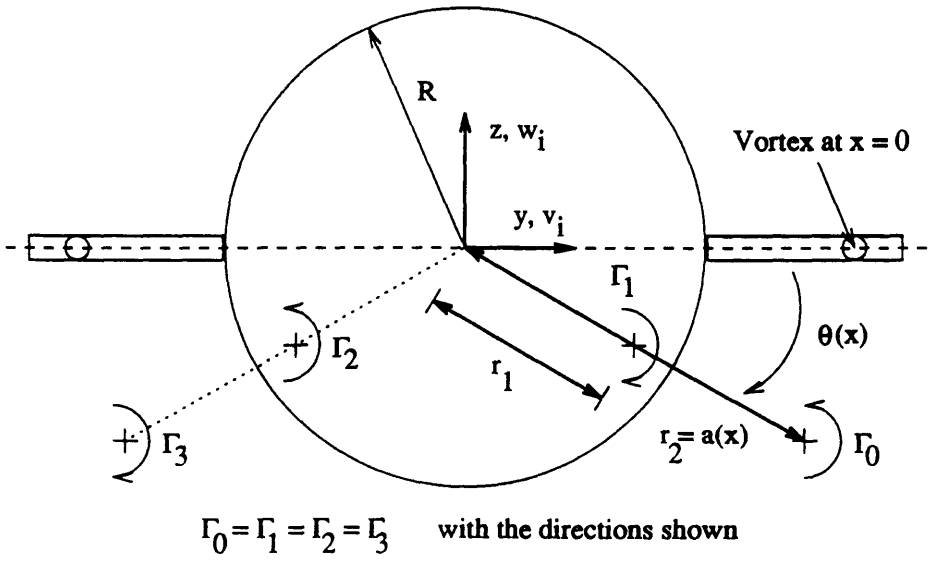

Figure 3-6: Full Wing-Body Configuration

where d_n is the distance between the subject real vortex and the n_{th} vortex. The vortices are designated Γ_1, Γ_2, and Γ_3 as in the figure, and the corresponding distances are:

$$\begin{aligned} d_1 &= a - r_1 \\ d_2 &= \sqrt{(a - r_1)^2 + 4ar_1 \cos^2\theta} \\ d_3 &= 2a\cos\theta \end{aligned}$$

and, if these distances are subject to the constraint $r_1 a = R^2$, the expressions become:

$$\begin{aligned} d_1 &= \frac{1}{a}(a^2 - R^2) \\ d_2 &= \left[\frac{1}{a^2}(a^2 - R^2)^2 + 4R^2\cos^2\theta\right]^{1/2} \\ d_3 &= 2a\cos\theta \end{aligned}$$

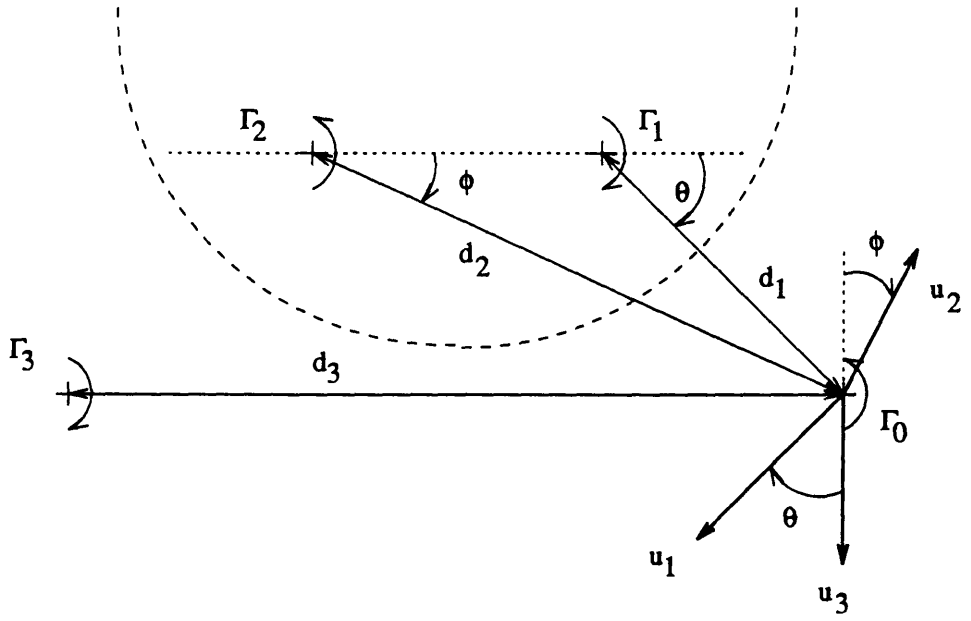

Figure 3-7: Velocities for Full Wing-Body Configuration

The velocities must then be resolved into their components as in Figure 3-7:

$$
\begin{aligned}
v_i &= = u_1 \sin\theta + u_2 \sin\phi \\
w_i &= -u_1 \cos\theta + u_2 \cos\phi - u_3
\end{aligned}
$$

where the angle ϕ is defined from Figure 3-7 as

$$
\begin{aligned}
\sin\phi &= \frac{a - r_1}{d_2} \sin\theta \\
&= \frac{1}{a} \frac{a^2 - R^2}{d_2} \sin\theta
\end{aligned}
$$

The distances and ϕ can also be non-dimensionalized by dividing by R, obtaining:

$$
\begin{aligned}
\bar{d}_1 &= \frac{1}{\bar{a}}(\bar{a}^2 - 1) \\
\bar{d}_2 &= \{\frac{1}{\bar{a}^2}(\bar{a}^2 - 1)^2 + 4\cos^2\theta\}^{1/2}
\end{aligned}
$$

$$= \{\bar{d}_1^{\,2} + 4\cos^2\theta\}^{1/2}$$

$$\bar{d}_3 = 2\bar{a}\cos\theta$$

$$\sin\phi = \frac{\bar{d}_1}{\bar{d}_2}\sin\theta$$

and, using the equations for sidewash and downwash discussed in the section dealing with half-wings, the following non-dimensional equations of motion can be obtained:

$$\frac{d\bar{z}}{d\bar{x}} = -\nu\left(1+\frac{\bar{x}}{\sqrt{\bar{x}^2+\bar{d}_1^{\,2}}}\right)\frac{\cos\theta}{\bar{d}_1} + \nu\left(1+\frac{\bar{x}}{\sqrt{\bar{x}^2+\bar{d}_2^{\,2}}}\right)\frac{\cos\phi}{\bar{d}_2}$$
$$- \nu\left(1+\frac{\bar{x}}{\sqrt{\bar{x}^2+\bar{d}_3^{\,2}}}\right)\frac{1}{\bar{d}_3}$$

$$\frac{d\bar{y}}{d\bar{x}} = \nu\left[-\left(1+\frac{\bar{x}}{\sqrt{\bar{x}^2+\bar{d}_1^{\,2}}}\right)\frac{\sin\theta}{\bar{d}_1} + \left(1+\frac{\bar{x}}{\sqrt{\bar{x}^2+\bar{d}_2^{\,2}}}\right)\frac{\sin\phi}{\bar{d}_2}\right]$$

Converting these equations to polar coordinates in much the same way gives the final equations of motion:

$$\frac{d\bar{a}}{d\bar{x}} = -\bar{u}_2\sin(\theta-\phi) + \bar{u}_3\sin\theta \tag{3.33}$$

$$\frac{d\theta}{d\bar{x}} = \frac{1}{\bar{a}}\left(\bar{u}_1 - \bar{u}_2\cos(\theta-\phi) + \bar{u}_3\cos\theta\right) \tag{3.34}$$

where, for $i = 1,..,3$,

$$\bar{u}_i = \frac{\nu}{\bar{d}_i}\left(1+\frac{\bar{x}}{\sqrt{\bar{x}^2+\bar{d}_i^{\,2}}}\right)$$

The general effect of these vortices on the rear wings is to induce both forces and moments on the wing. This effect is, however, highly configuration-dependent, so specific results can only be determined after the wing-body configuration is known.

Flap Effects

The analysis of the lifting surfaces detailed above was based on the assumption that the surfaces were all-movable, i.e. the surfaces consisted of one piece that pivoted about the root of the wing to provide lift. This surfaces extends some of the theories

above to include expressions for stationary wings with flaps.

The question to be answered by this analysis is what is the effect of a change in flap angle on the lift. The flap effect manifests itself in the coefficient of lift C_L, making it possible to substitute easily the expressions obtained here into the equations derived in the previous sections. The new expression for C_L is, assuming small angles

$$\begin{aligned} C_L &= \frac{\partial C_L}{\partial \alpha}\alpha + \frac{\partial C_L}{\partial \eta_f}\eta_f \\ &= \frac{\partial C_L}{\partial \alpha}(\alpha + \tau\eta_f) \end{aligned}$$

where $\tau = \partial\alpha/\partial\eta_f$ is the flap effectiveness factor, η_f is the flap angle measured from the wing chordline, and $\partial C_L/\partial\alpha$ is the low aspect ratio lift-curve slope derived above.

Now, for the analysis to result in useful-closed form expressions that can be implemented immediately in a program, there are a number of assumptions that must be made. First of all, the wing shall be considered infinite for purposes of determination of the induced angle of attack, so strip theory will be the prevalent aerodynamic theory. Second of all, the flap itself will run the length of the wing so as to maximize its effect on the angle of attack, and its chord c_f shall be constant along the span of the wing.

If the above assumptions are adhered to, according to [13] the expression for flap effectiveness factor is

$$\tau = \frac{2}{\pi}(\sqrt{\lambda_f(1-\lambda_f)} + \sin^{-1}\sqrt{\lambda_f}) \tag{3.35}$$

where λ_f is the flap-chord ratio, defined by:

$$\lambda_f = \frac{c_f}{c(\eta)}$$

and $\eta = y/s$, the dimensionless spanwise coordinate. Now, for a trapezoidal wing, the chord varies as η as follows

$$c(\eta) = c_r[1 - (\lambda - 1)\eta]$$

where λ is the taper ratio. Putting this expression into the ones for the flap-chord ratio and the induced angle of attack change gives for a constant flap chord c_f:

$$\lambda_f(\eta) = \frac{c_f}{c_r}\frac{1}{1-(\lambda-1)\eta}$$

$$\tau(\eta) = \frac{2}{\pi}(\sqrt{\lambda_f(\eta)(1-\lambda_f(\eta))} + \sin^{-1}\sqrt{\lambda_f(\eta)})$$

so, if strip theory is used, the flap effectiveness factor along the entire wing can be obtained by summing the contributions of each wing section located at η, giving

$$\tau = \int_0^1 \tau(\eta)d\eta \tag{3.36}$$

There are two cases that can be solved for here: that of the rectangular wing and that of the trapezoidal wing. The rectangular wing case is very simple, as c is not a function of η, so $\lambda_f = c_f/c$ and

$$\tau = \frac{2}{\pi}(\sqrt{\lambda_f(1-\lambda_f)} + \sin^{-1}\sqrt{\lambda_f})$$

and the lift for a rectangular wing with a full-length flap can be found from this expresssion.

The expression for a trapezoidal wing is much more complex, but the integral can be solved analytically. Inserting the expression for λ_f as a function of η into the expression for τ gives

$$\tau = \frac{2}{\pi}\left(\int_0^1 \left[\sqrt{\frac{c_f}{c_r}\frac{1}{1-(\lambda-1)\eta}\left(1-\frac{c_f}{c_r}\frac{1}{1-(\lambda-1)\eta}\right)} + \sin^{-1}\sqrt{\frac{c_f}{c_r}\frac{1}{1-(\lambda-1)\eta}}\right]d\eta\right)$$

This can be simplified for purposes of integration by substituting $k_1 = c_f/c_r$ and $k_2 = \lambda - 1$, giving

$$\tau = \frac{2}{\pi}\left(\int_0^1 \sqrt{\frac{k_1(1-k_2\eta-k_1)}{(1-k_2\eta)^2}}d\eta + \int_0^1 \sin^{-1}\sqrt{\frac{k_1}{1-k_2\eta}}d\eta\right)$$

$$= \frac{2}{\pi}(I_1(\eta) + I_2(\eta))$$

The evaluation of the two integrals $I_1(\eta)$ and $I_2(\eta)$ can be performed numerically or analytically. The unsimplified analytical results are:

$$I_1 = 2\left[\frac{\sqrt{k_1(1-k_1)-k_1k_2\eta}}{k_2} - \frac{k_1}{k_2}\tan^{-1} - \frac{\sqrt{k_1(1-k_1)-k_1k_2\eta}}{k_1k_2}\right]_0^1$$

$$I_2 = \frac{k_1}{k_2}\left[\frac{1}{x^2}\sin^{-1}x + \frac{1}{2x}\sqrt{1-x^2}\right]_{x_0}^{x_1}$$

where $x_0 = \sqrt{k_1}$ and $x_1 = \sqrt{k_1(1-k_2)}$.

Numerical values for these expressions may be obtained by evaulating k_1 and k_2 in terms of c_r,c_t, and λ. For a rectangular wing, if $c = 6$ft and $c_f = 2$ft, then $\lambda_f = 1/3$, and $\tau = .6919$. For a trapezoidal wing, if $c_t = 8.5$ft, $c_r = 10.2$ft, and $c_f = 2$ft, then $k_1 = 1/3$, $k_2 = -1.667$, $I_1 = 2$, $I_2 = -.39$, and $\tau = 1.025$.

3.2.2 Annular Wings

Although there had previously existed a number of analyses concerning the lifting characteristics of annular wings ([14], [15], [16], [17]) , it was decided that a full re-analysis of the characteristics of annular wings should be performed in order to generalize the results found in [14] and [15] to include provisions for twisted and cambered annular lifting surfaces. Two types of analysis were performed to determine said lifting characteristics. The first, a strip theory analysis, was performed to give a rough estimate of the lifting charcteristics. The second, a lifting-line analysis, was performed to give a more accurate model of the aerodynamic properties of the wing. The lifting-line analysis also included a section concerning the downwash of the fore wing and its interaction with the vehicle body and the aft wing. The results of each evaluation were then compared with experimental results and other analyses.

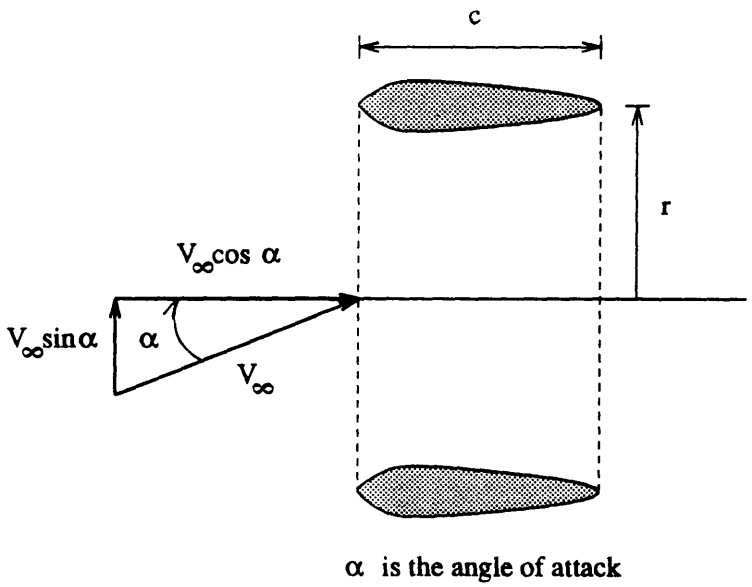

Figure 3-8: Side View of Annular Wing at Angle of Attack

Strip Theory

For the strip theory analysis, the flow was considered incompressible and inviscid, and the wing was considered to be uncambered and untwisted.

If an annular wing of radius r and chord c is travelling at speed V_∞ at an angle of attack α, then the incoming velocity can be reduced to its components as per Figure 3-8. Strip theory states that each infinitesimal strip of the annular wing may be considered as a separate two-dimensional lifting surface, ignoring any interactions with the surfaces surrounding it and ignoring the effects of the trailing vortex system, i.e. is the case where $r \gg c$. Therefore, the annular wing may be modelled as a series of these infinitesimal surfaces. If θ is defined as the angle between the positive y-axis and the strip in question, then it can be seen in Figure 3-9 that the velocity normal to a strip located at angle θ is defined by:

$$V_n = V_\infty \sin \alpha \sin \theta$$

So, for each specific strip there is a component of velocity $V_\infty \cos \alpha$ parallel to the

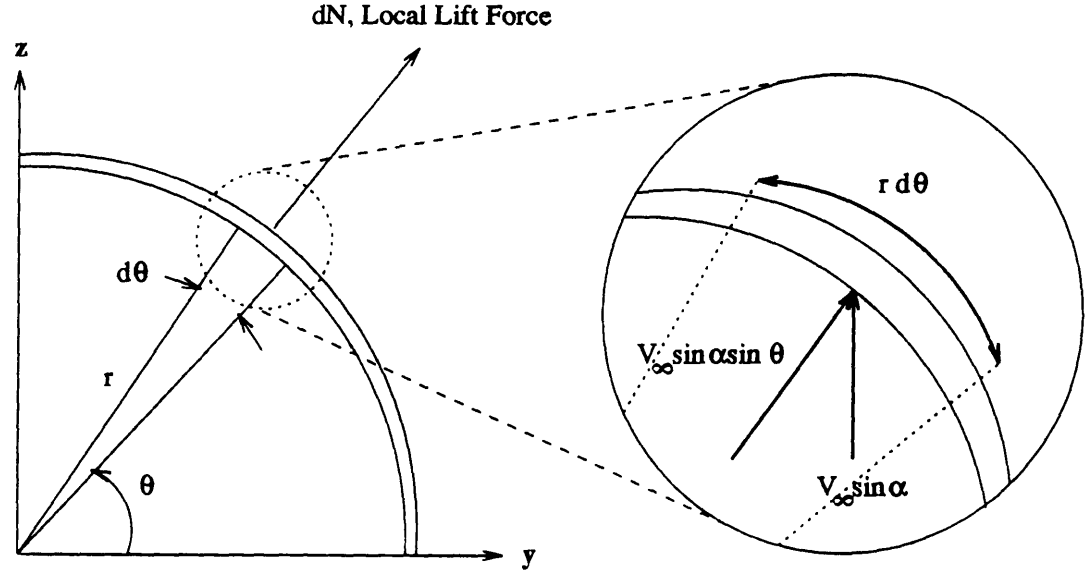

Figure 3-9: Annular Wing Strip Element

strip and a component $V_\infty \sin\alpha \sin\theta$ perpendicular to the strip.

Using these two components of velocity, it is possible to define a virtual angle of attack ϕ and virtual incoming velocity V for each strip. These are represented by:

$$\tan\phi = \frac{V_\infty \sin\alpha \sin\theta}{V_\infty \cos\alpha} = \tan\alpha \sin\theta$$

$$V^2 = V_\infty^2 \cos^2\alpha + V_\infty^2 \sin^2\alpha \sin^2\theta$$

It will be assumed that ϕ is small because α is small, so $\tan\phi \cong \phi$, $\phi \cong \alpha \sin\theta$, and $V \cong V_\infty$.

If thin-wing theory is then assumed for this model, the incremental lift produced is on the strip is:

$$dN = \frac{1}{2}\rho V_\infty^2 C_L dS$$

and, if $C_L = m_0\phi$ where m_0 is the two-dimensional lift-curve slope and $dS = crd\theta$, the lift becomes:

$$dN(\theta) = \frac{1}{2}\rho V_\infty^2 crm_0\phi(\theta)d\theta$$

Note that the component of lift expressed here is that component normal to the surface of the ring wing. In order to obtain the net vertical lift, the vertical component of this lift, $dN \sin\theta$, must be used. This results in the expression:

$$dN = \frac{1}{2}\rho V_\infty^2 c r m_0 \phi(\theta) \sin\theta d\theta$$

This expression can be integrated around the circumference of the ring to give:

$$L = \pi^2 \rho V_\infty^2 c r \alpha \tag{3.37}$$

Finally, if one converts the lift to C_L by means of

$$C_L = \frac{L}{\frac{1}{2}\rho V_\infty^2 S} \tag{3.38}$$

and inserts $S = 2rc$, the resulting expression is the strip theory expression for the coefficient of lift for an annular wing:

$$C_L = \pi^2 \alpha \tag{3.39}$$

This result is the limiting case for $r \gg c$.

Lifting-Line Theory

A more thorough examination of the lifting properties of an annular wing requires the use of a theory that takes into account the three-dimensional interactions present. This analysis of the annular wing will utilize lifting-line theory to obtain expressions for the lifting characteristics.

Once again, we have our angular wing incident to the flow as seen in Figure 3-8. If general lifting-line theory is utilized, the circulation around the wing will be concentrated as a vortex ring located at the quarter-chord line. As can be seen in Figure 3-10, conservation of vorticity dictates that the ring vortex will shed a trailing

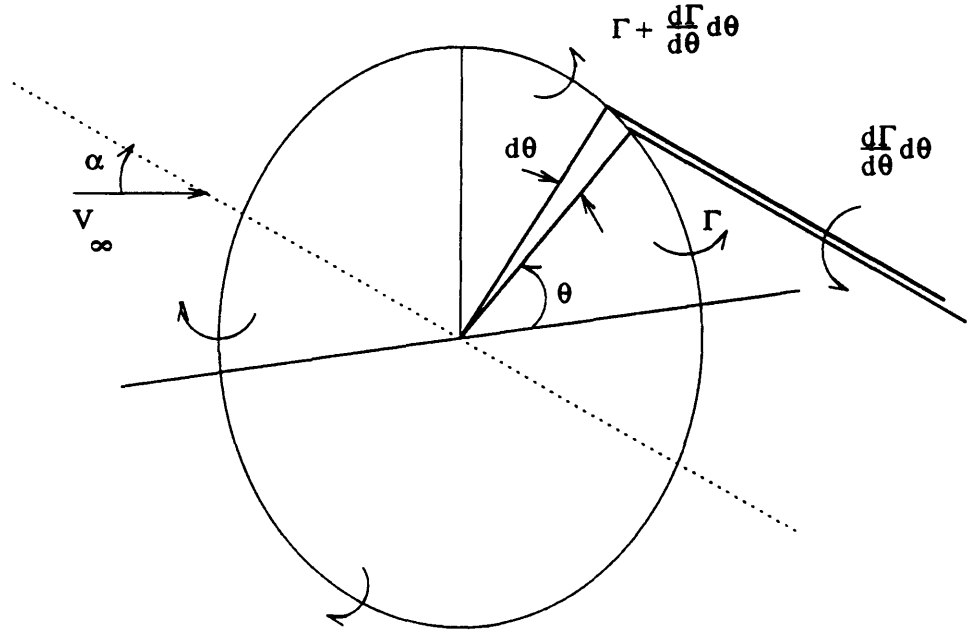

Figure 3-10: Vortex Shedding by Annular Wing

vortex of magnitude:

$$\frac{d\Gamma}{d\theta}d\theta$$

The first objective of this analysis will be to find the velocity u_i induced along the wing by the ring vortex. The normal incident velocity on an arbitrary strip of the wing located a θ is given, as in the previous section, by the expression:

$$V_n \cong V_\infty \left(\alpha \sin\theta + \alpha_T(\theta)\right))$$

where now $\alpha_T(\theta)$ is the wing twist distribution. Now, an expression for the induced velocity due to the circulation can be derived as follows: As can be seen in Figure 3-11, what needs to be calcuated is the velocity du_i induced at point Q at angle ϕ due to the semi-infinite vortex of strength $(d\Gamma/d\theta)d\theta$ shed at point R.

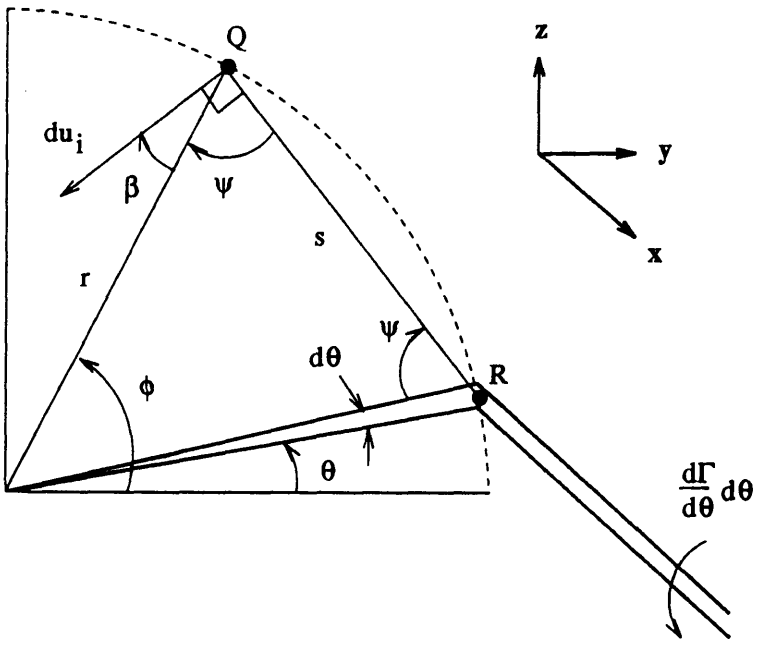

Figure 3-11: Annular Wing Induced Velocity

According to the Biot-Savart Law,

$$du_i = \frac{1}{4\pi s}\frac{d\Gamma}{d\theta}d\theta$$

where s is the distance between Q and R.

This du_i is the component of the 'inwash' perpendicular to the line segment s, and what is desired is the component of the velocity directed radially inward. In order to obtain this, β, ϕ and θ need to be related, as seen in Figure 3-11, by the equation:

$$\phi - \theta + 2\psi = \pi$$

$$\psi = \pi/2 - (\phi - \theta)/2$$

where ψ is defined in the Figure. From this, it can be seen that

$$\beta = \frac{\phi - \theta}{2}$$

so,

$$du = du_i \cos\frac{\phi - \theta}{2} \tag{3.40}$$

The induced velocity can be obtained by integrating with respect to θ from 0 to 2π in the following form:

$$u_i = \int_0^{2\pi} \frac{1}{4\pi s} \cos\frac{\phi - \theta}{2} \left(\frac{d\Gamma}{d\theta}\right) d\theta \tag{3.41}$$

and, since, $s = 2r \sin\frac{\phi-\theta}{2}$ the expression becomes

$$u_i = \int_0^{2\pi} \frac{1}{8\pi r} \cot\frac{\phi - \theta}{2} \left(\frac{d\Gamma}{d\theta}\right) d\theta \tag{3.42}$$

Now, a general form of the distribution of Γ is required. Due to symmetry constraints and for twist of the form $\alpha_T(\theta - \pi) = \alpha_T(\theta)$, the $\Gamma(\theta)$ that will be chosen must be of the form:

$$\Gamma(\pi - \theta) = \Gamma(\theta)$$

A distribution that satisfies this condition is of the form:

$$\Gamma(\theta) = A_n \sin n\theta$$

where n is an odd integer. To complete the procedure, the distribution must be inserted into the velocity equation to obtain the coefficients A_n. The assumed circulation will be of the form:

$$\Gamma(\theta) = \sum_{n=1}^{\infty} A_n \sin n\theta \tag{3.43}$$

where $n = 1, 3, 5, \ldots$ so, the derivative is:

$$\frac{d\Gamma}{d\theta} = \sum_{n=1}^{\infty} nA_n \cot n\theta \tag{3.44}$$

Putting this into the integral gives:

$$u_i = \frac{1}{8\pi r} \int_0^{2\pi} \cot\frac{\phi - \theta}{2} \sum_{n=1}^{\infty} nA_n \cos n\theta d\theta \tag{3.45}$$

or

$$-u_i = \frac{1}{8\pi r}\sum_{n=1}^{\infty} nA_n \int_0^{2\pi} \cos n\theta \cot\frac{\theta-\phi}{2} d\theta \tag{3.46}$$

$$= \frac{1}{8\pi r}\sum_{n=1}^{\infty} nA_n I_n \tag{3.47}$$

where,

$$I_n = \int_0^{2\pi} \cos n\theta \cot\frac{\theta-\phi}{2} d\theta \tag{3.48}$$

The evaluation of this integral is very similar to one presented in [14]), but the limits are different for this application, so a summary of the integration procedure is given in Appendix A. The final expression for the integral is:

$$I_n = -2\pi \sin n\phi \tag{3.49}$$

where n must be odd. Putting I_n into the velocity expression gives:

$$-u_i = \frac{1}{8\pi r}\sum_{n=1}^{\infty} nA_n(-2\pi \sin n\phi) \tag{3.50}$$

or,

$$4ru_i = \sum_{n=1}^{\infty} nA_n \sin n\phi \tag{3.51}$$

For the sake of completeness, it is possible to consider an even more general form of circulation distribution:

$$\Gamma(\theta) = \sum_{n=0}^{\infty}[A_n \sin(2n+1)\theta + B_n \cos 2n\theta] \tag{3.52}$$

$$\frac{d\Gamma}{d\theta} = \sum_{n=1}^{\infty}[(2n+1)A_n \cos(2n+1)\theta - 2nB_n \sin 2n\theta] \tag{3.53}$$

Please note the change in the indicial notation. Inserting this into Equation (3.42) gives:

$$-u_i = \frac{1}{8\pi r}\int_0^{2\pi} \cot\frac{\theta-\phi}{2} \sum_{n=0}^{\infty}\{(2n+1)A_n \cos(2n+1)\theta$$

$$
\begin{aligned}
& -2nB_n \sin 2n\theta\} d\theta \\
= \; & \frac{1}{8\pi r}\{\sum_{n=0}^{\infty}(2n+1)A_n \int_0^{2\pi} \cot\frac{\theta-\phi}{2}\cos(2n+1)\theta d\theta \\
& -\sum_{n=0}^{\infty} 2nB_n \int_0^{2\pi} \cot\frac{\theta-\phi}{2}\sin 2n\theta d\theta\}
\end{aligned}
$$

It is known fron the integral evaluated in Appendix A that

$$
\int_0^{2\pi} \cot\frac{\theta-\phi}{2}\cos(2n+1)\theta d\theta = -2\pi\sin(2n+1)\phi
$$

however, the other integral requires a short amount of analysis as follows:

If

$$
I(\theta) = \int_0^{2\pi} \cot\frac{\theta-\phi}{2}\sin 2n\theta d\theta
$$

and the following definitions are made:

$$
\begin{aligned}
\theta - \phi &= x \\
d\theta &= dx
\end{aligned}
$$

then the integral may be expressed as:

$$
I'(x) = \int_{-\phi}^{2\pi-\phi} \cot\left(\frac{x}{2}\right)\sin 2n(x+\phi)dx
$$

and this integral is evaluated as follows:

$$
\begin{aligned}
I'(x) &= \int_{-\phi}^{2\pi-\phi} \sin 2nx\cos 2n\phi\cot\left(\frac{x}{2}\right)dx + \int_{-\phi}^{2\pi-\phi}\cos 2nx\sin 2n\phi\cot\left(\frac{x}{2}\right)dx \\
&= \cos 2n\phi\int_{-\phi}^{2\pi-\phi}\sin 2nx\cot\left(\frac{x}{2}\right)dx + \sin 2n\phi\int_{-\phi}^{2\pi-\phi}\cos 2nx\cot\left(\frac{x}{2}\right)dx \\
&= 2\pi\cos 2n\phi
\end{aligned}
$$

where the two integrals are the same as I_1 and I_2 found in the Appendix. Inserting

the results of this integral into the velocity equation obtains:

$$\begin{aligned} -u_i &= \frac{1}{8\pi r}\left[\sum_{n=0}^{\infty}(2n+1)A_n(-2\pi\sin(2n+1)\phi) - \sum_{n=0}^{\infty}2nB_n(2\pi\cos 2n\phi)\right] \\ u_i &= \frac{1}{4r}\left[\sum_{n=0}^{\infty}(2n+1)A_n\sin(2n+1)\phi + 2nB_n\cos 2n\phi\right] \end{aligned} \tag{3.54}$$

This expression is more general that those found in [14] and [15], for it will hold for an annular wing with a general twist distribution. The corresponding circulation distribution is given by Equation (3.52). The values of the A_n and B_n coefficients must be determined by relating the local angle of attack to the wing section lift properties and equating coefficients of $\sin n\phi$ and $\cos n\phi$ or by an equivalent process.

The actual angle of attack at each point on the wing as a function of θ will be:

$$\alpha_n(\theta) = \alpha_a - \alpha_i \tag{3.55}$$

where,

$$\begin{aligned} \alpha_a &= \alpha\sin\theta + \alpha_T(\theta) \\ \alpha_i &= \frac{u_i(\theta)}{V_\infty} \end{aligned}$$

Now, using the Kutta-Joukouwski Theorem, as explained in [8], the lifting-line theory expression for the circulation can be obtained. The theory states that the lift per unit span is related by

$$\rho V_\infty \Gamma(\theta) = \frac{1}{2}\rho V_\infty^2 c C_L \tag{3.56}$$

where c is the chord (constant) and,

$$C_L = m_0\alpha_n(\theta)$$

and m_0 is the section lift-curve slope. Substitution using Equations (3.42), (3.54),

and (3.56) gives:

$$\left(1+\frac{m_0 c}{8r}\right)\sum_{n=0}^{\infty}\left[A_n \sin(2n+1)\theta + B_n \cos 2n\theta\right] = \frac{V_\infty c m_0}{2}\left[\alpha \sin\theta + \alpha_T(\theta)\right] \qquad (3.57)$$

For the untwisted wing, all of the coefficients except A_0 are zero and A_0 is given by:

$$(1+\frac{m_0 c}{8r})A_0 = \frac{V_\infty m_0 c}{2}\alpha$$

so, for $m_0 = 2\pi$,

$$\begin{aligned} A_0 &= \frac{1}{1+\pi c/4r}\pi V_\infty c\alpha \\ &= \frac{4r/\pi c}{1+4r/\pi c}\pi V_\infty c\alpha \end{aligned}$$

and the expression for the circulation is given by:

$$\Gamma(\theta) = \frac{4r/\pi c}{1+(4r/\pi c)}\pi V_\infty c\alpha \sin\theta \qquad (3.58)$$

which corresponds exactly to the results found in [14] and [15].

The lift that results from this circulation can be found by using the expression

$$\begin{aligned} L &= \int_0^{2\pi} \rho V_\infty \Gamma(\theta) r \sin\theta d\theta \\ &= \frac{4r/\pi c}{1+4r/\pi c}\rho V_\infty^2 \pi^2 r c\alpha \end{aligned}$$

and the lift coefficient is

$$\begin{aligned} C_L &= \frac{L}{\frac{1}{2}\rho V_\infty^2 \mathcal{S}} \\ &= \frac{2AR/\pi}{1+2AR/\pi}\pi^2\alpha \end{aligned} \qquad (3.59)$$

where $\mathcal{S} = 2rc$, as before, and $AR = 2r/c$. As an additional check on the theory, and because of the elliptical distribution of the annular wing, the coefficient of drag was

also computed using

$$D_i = \int_0^{2\pi} \rho u_i(\theta)\Gamma(\theta) r d\theta$$

to give

$$\begin{aligned} C_{D_i} &= \frac{C_L^2}{2\pi AR} \\ &= \frac{2\pi AR}{(1+2AR/\pi)^2}\alpha^2 \end{aligned} \tag{3.60}$$

Downwash Interactions

As the forward annular wing produces a downwash that will affect the aerodynamic properties of the rear annular wing, it is necessary to examine the downwash interactions of the annular wings. This would normally be a complex procedure for non-planar wakes, but fortunately numerical experiments [18] show that it is reasonable to assume that the wake produced by the fore annular wing rolls up into two line vortices located on or near the y-axis, parallel to the x-axis. This allows one to integrate over the wing circulation to find the strength of the vortex and its location, then use the methods defined in the section concerning trapezoidal wings to obtain the behavior of the vortex with respect to the body.

The primary question to be answered concerns the strength of the twin vortices shed by the annular wing and their location along the y-axis. The magnitude of the circulation around the annular wing is given by the expression

$$\begin{aligned} \Gamma(\theta) &= \frac{4r/\pi c}{1+(4r/\pi c)}\pi V_\infty c\alpha \sin\theta \\ &= A_0 \sin\theta \end{aligned}$$

The strength Γ_0 of each line vortex that is shed from half of the annular wing can be obtained from the formula

$$\Gamma_0 = \int_{-\pi/2}^{\pi/2} \frac{d\Gamma}{d\theta} d\theta \tag{3.61}$$

so, inserting $d\Gamma/d\theta = A_0 \cos\theta$ gives

$$\begin{aligned}\Gamma_0 &= \int_{-\pi/2}^{\pi/2} A_0 \cos\theta d\theta \\ &= 2A_0\end{aligned}$$

The spanwise location of each vortex with respect to the x-axis is designated by b_a, and is given approximately by

$$b_a = \frac{\int_0^r y\frac{d\Gamma}{dy}dy}{\int_0^r \frac{d\Gamma}{dy}dy} \tag{3.62}$$

The problem now reduces to finding an expression for $d\Gamma/dy$ and integrating it over y. First of all, through the chain rule

$$\frac{d\Gamma}{dy} = \frac{d\Gamma}{d\theta}\frac{d\theta}{dy}$$

and, as $y = r\cos\theta$, its derivative results in the expression

$$\begin{aligned}\frac{dy}{d\theta} &= -r\sin\theta \\ \frac{d\theta}{dy} &= -\frac{1}{r}\csc\theta\end{aligned}$$

and, combined with the above expression

$$\frac{d\Gamma}{d\theta} = A_0\cos\theta = A_0\frac{y}{r}$$

gives the desired formula

$$\frac{d\Gamma}{dy} = -\frac{y}{r^2}A_0\csc\theta$$

The expression for $\csc\theta$ can also be expressed in terms of y and r as

$$\csc\theta = \pm\frac{r}{\sqrt{r^2 - y^2}}$$

so, taking the negative part, one obtains

$$\frac{d\Gamma}{dy} = -\frac{y}{r}\frac{A_0}{\sqrt{r^2 - y^2}} \tag{3.63}$$

Putting this into the integrals for b_a gives

$$\begin{aligned}
\int_0^r y\frac{d\Gamma}{dy}dy &= -\frac{A_0}{r}\int_0^r \frac{y^2}{\sqrt{r^2 - y^2}}dy \\
&= -\frac{A_0}{r}[-\frac{y}{2}\sqrt{r^2 - y^2} + \frac{r^2}{2}\sin^{-1}\frac{y}{r}]_0^r \\
&= -A_0 r\frac{\pi}{4}
\end{aligned}$$

and,

$$\begin{aligned}
\int_0^r \frac{d\Gamma}{dy}dy &= -\frac{A_0}{r}\int_0^r \frac{dy}{\sqrt{r^2 - y^2}} \\
&= -\frac{A_0}{r}[-\sqrt{r^2 - y^2}]_0^r \\
&= -A_0
\end{aligned}$$

so, the distance from the x-axis of each vortex is given by

$$\frac{b_a}{r} = \frac{\pi}{4} \tag{3.64}$$

This information can also be used as a lifting-line approximation to the distance between vortices coming from a trapezoidal wing [13], i.e. $b_a = \frac{1}{2}h$ for a trapezoidal wing.

Comparison With Experiment

The expressions dealt with in the section concerning trapezoidal lifting surfaces had a relatively large base of experimental results for comparisons ([8], [9], [10], [13]). However, there has not been nearly as much experimental work done with annular wings, so it was decided that a comparison with available analyses concerning annular wings would be beneficial by displaying the validity of the expressions that were

derived for the lifting characteristics.

The theory developed in [14] concerns channel wings, and the theory obtained in [15] is slightly less general than that presented here. However, both theories give results in the limit of untwisted annular wings which agree with the results obtained here.

The following comparison compares the strip and lifting-line theories derived above with an modified lifting-line theory solution [16], [17] and experimental data [19]. In this modified theory, the vortex strength is calculated by satisfying the downwash condition at the three-quarter chord point, whereas here and in [14], [15], the vortex strength is obtained by using the sectional lift properties. The theories to be compared are summarized as follows:

Strip theory:

$$C_l = \pi^2 \alpha$$

$$C_{D_i} = 0$$

Lifting-Line Theory:

$$C_L = \frac{2AR/\pi}{1 + 2AR/\pi} \pi^2 \alpha$$

$$C_{D_i} = \frac{2\pi AR}{(1 + 2AR/\pi)^2} \alpha^2$$

Alternate Lifting-Line Theory (Weissinger and McCormick):

$$\begin{aligned} C_L &= \frac{\pi}{2} \left(\frac{dC_L}{d\alpha} \right)_{elliptic} \alpha \\ &= \frac{\pi}{2} \left[\frac{2\pi AR_n}{AR_n + 2(AR_n + 4)/(AR_n + 2)} \right] \alpha \end{aligned}$$

where, as before $AR = 2r/c$, this expression has $AR_n = 8r/\pi c$. No expression for C_{D_i} was available in [17].

As the paper that contained the experimental data [19] displays data for specific sets of aspect ratios, the following comparisons will be made using the theories stated

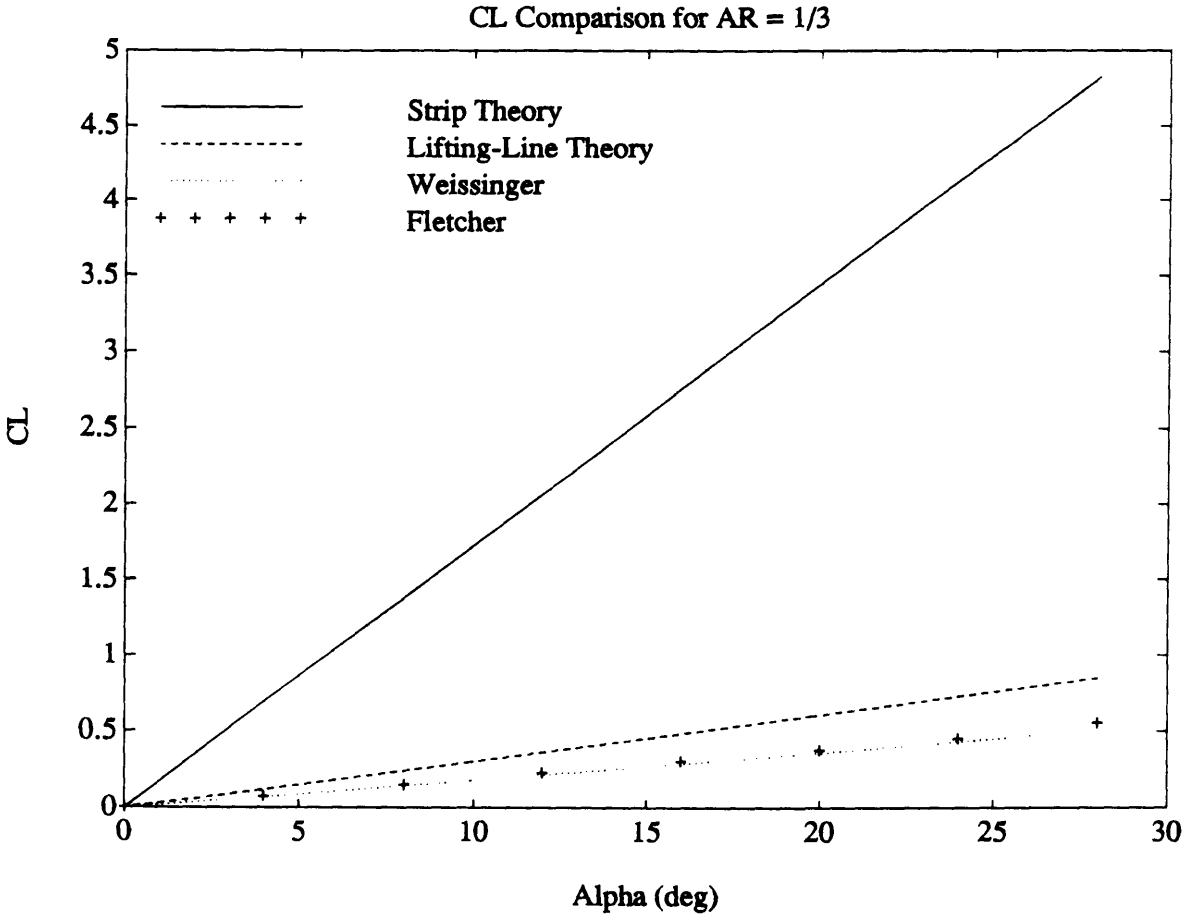

Figure 3-12: CL Comparison for AR = 1/3

above: a C_L comparison for all three theories and the data, and an induced drag coeffiecient C_{D_i} comparison between the lifting-line theory derived above and the experimental data. Each comparison shall be performed for five aspect ratios: $AR = \frac{1}{3}, \frac{2}{3}, 1, 1.5, 3$, which, most importantly, encompasses the aspect ratio range that the applications discussed later fall into. The C_L comparisons are shown in Figures 3-12 - 3-16, and the C_{D_i} comparisons are shown in Figures 3-17 - 3-21. For the experimental data, C_{D_i} was obtained by subtracting the C_D value at zero angle of attack.

Examination of these comparisons reveals many salient points about the behavior of the theories derived above. An important point to note is that the angle of attack range that each comparison covers is progressively less with increasing aspect ratio. This is due to the fact that the data from [19] showed that the lower the aspect ratio, the greater is the angle of attack for flow separation. The largest angle of attack chosen for each comparison is one that is just below flow separation. The theories

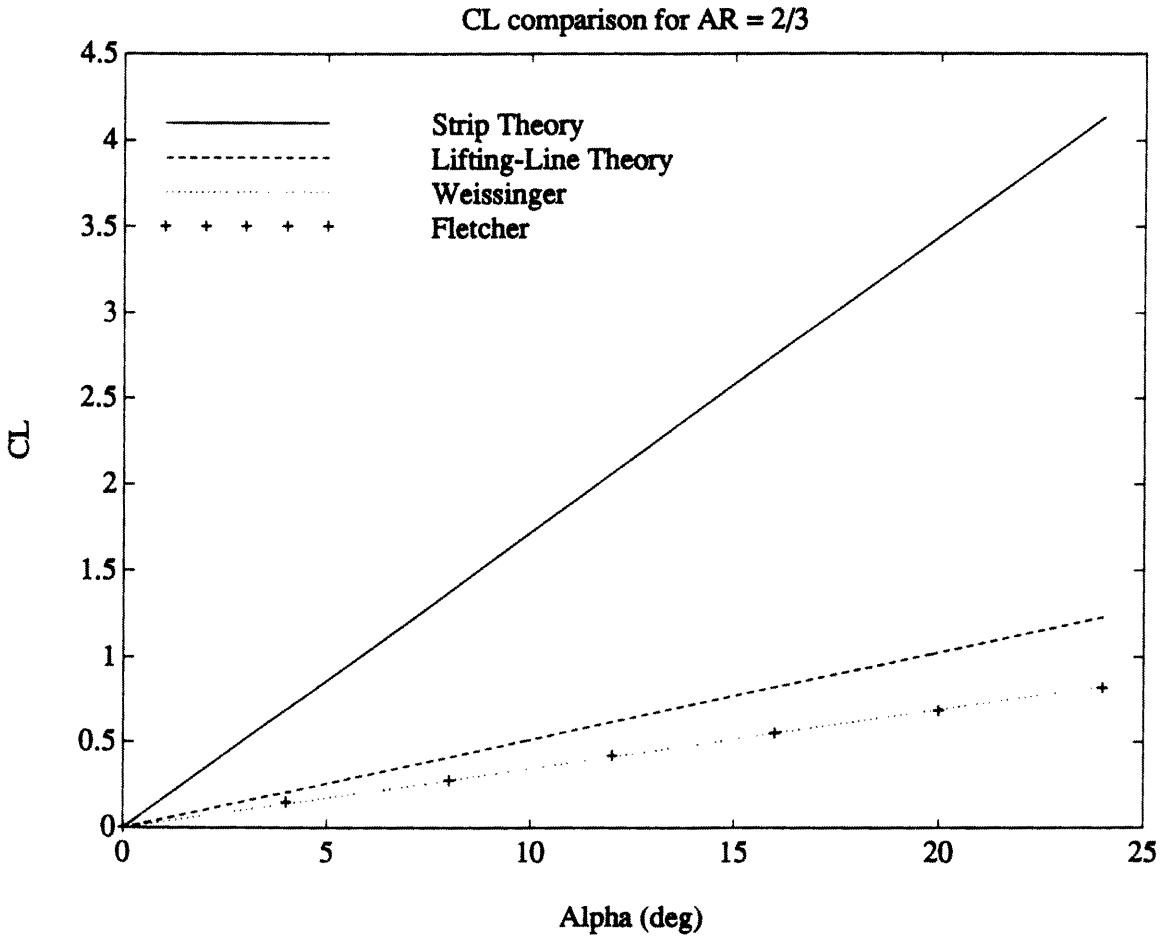

Figure 3-13: CL Comparison for AR = 2/3

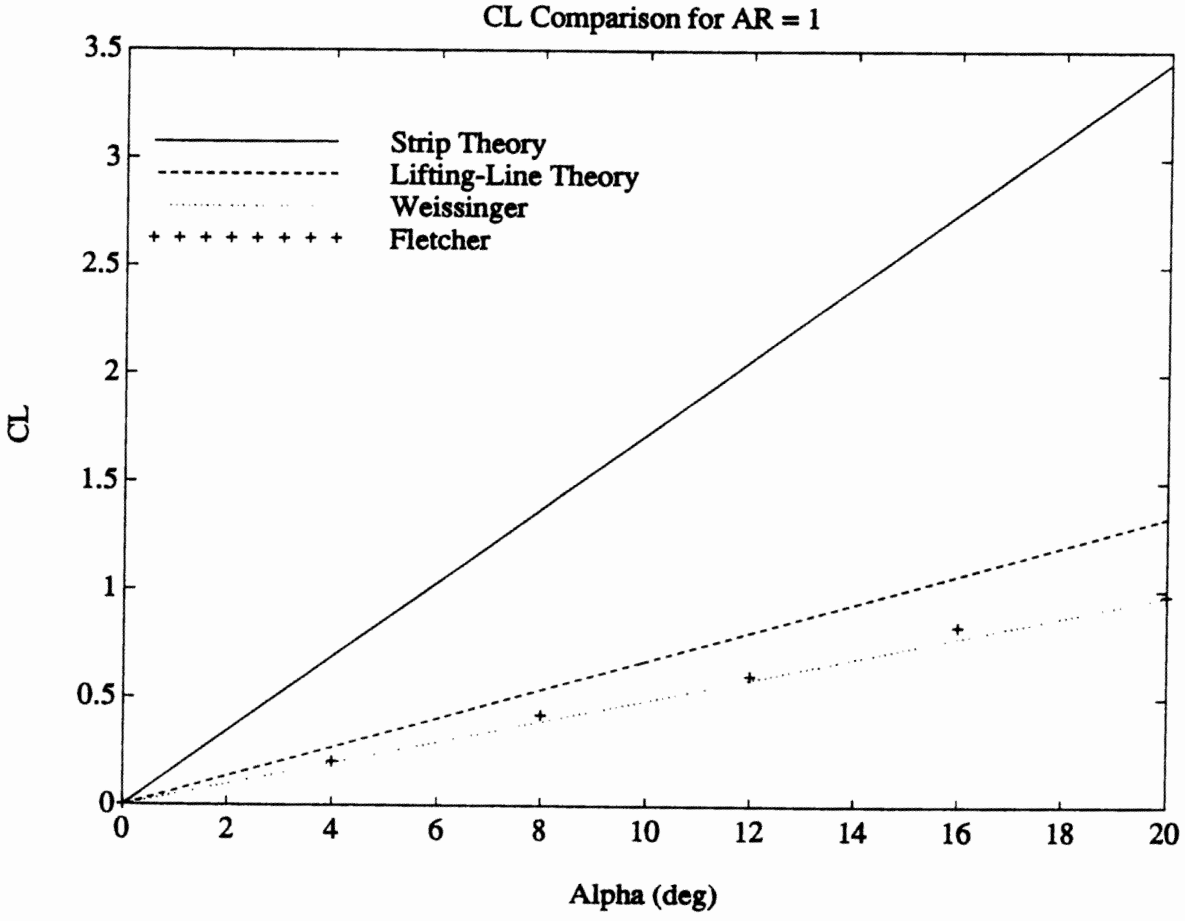

Figure 3-14: CL Comparison for AR = 1

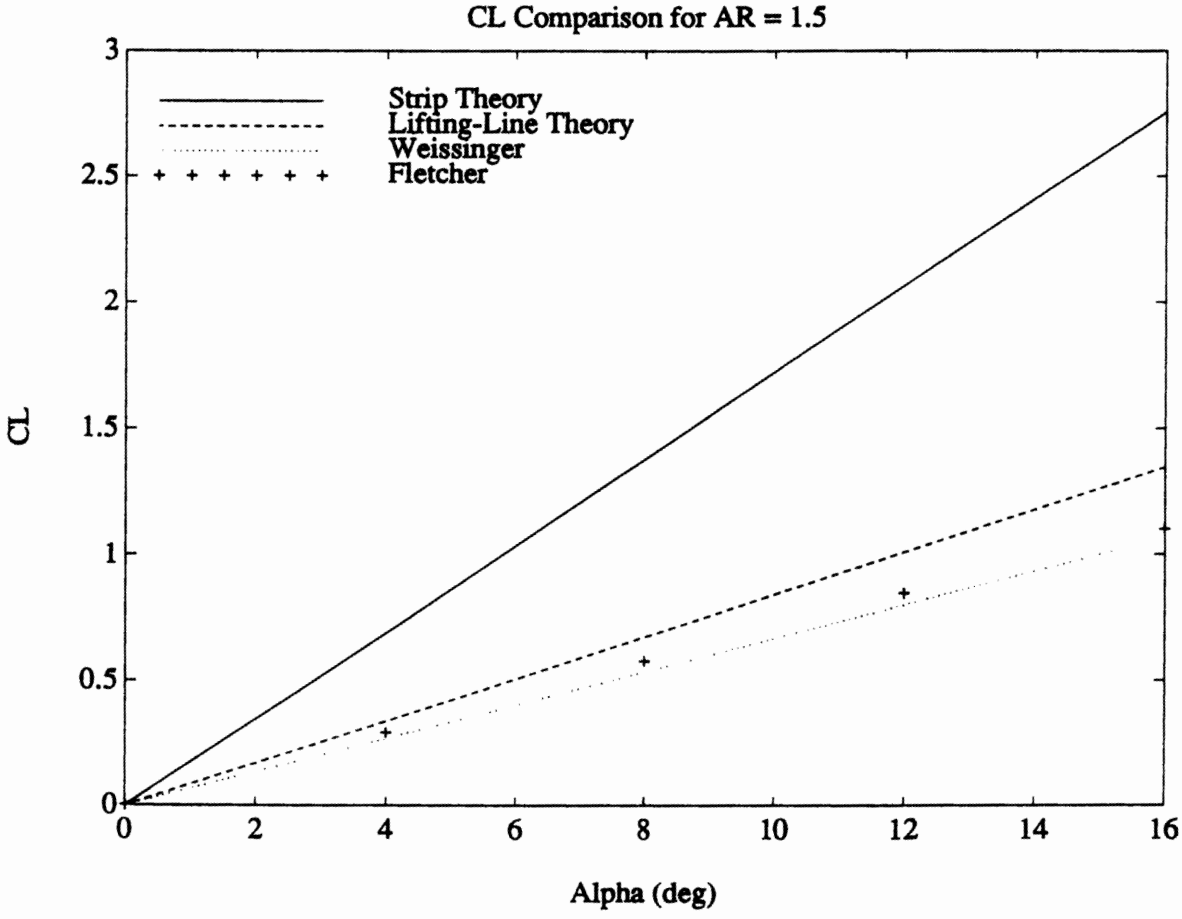

Figure 3-15: CL Comparison for AR = 1.5

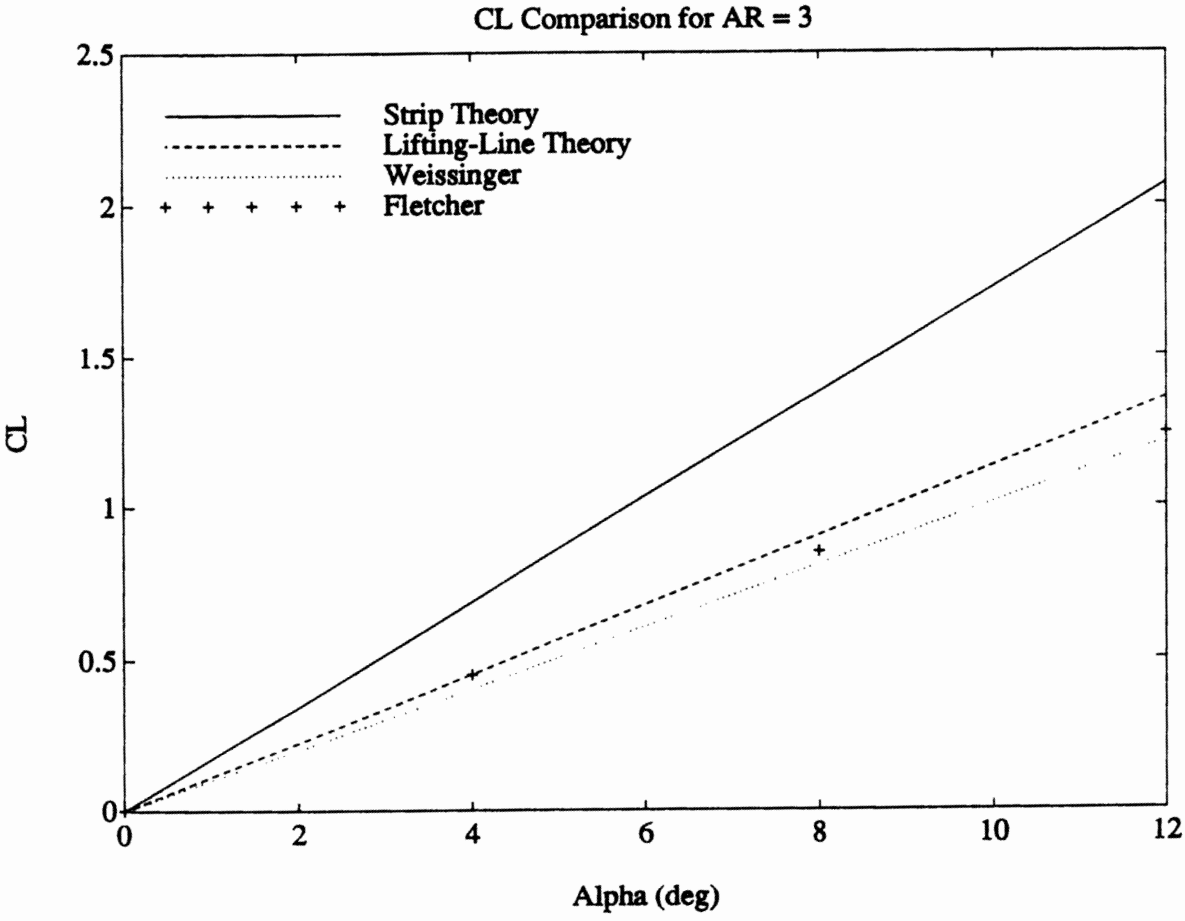

Figure 3-16: CL Comparison for AR = 3

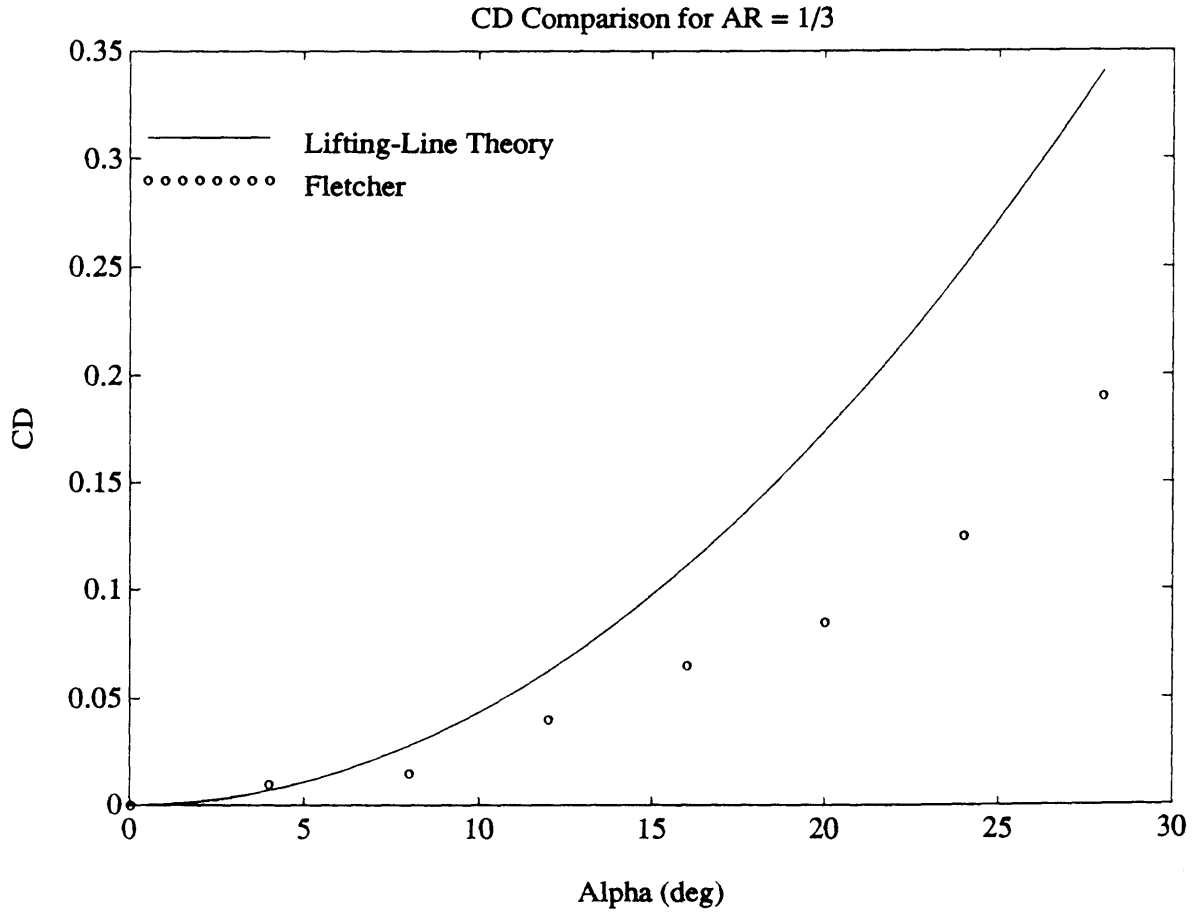

Figure 3-17: CD Comparison for AR = 1/3

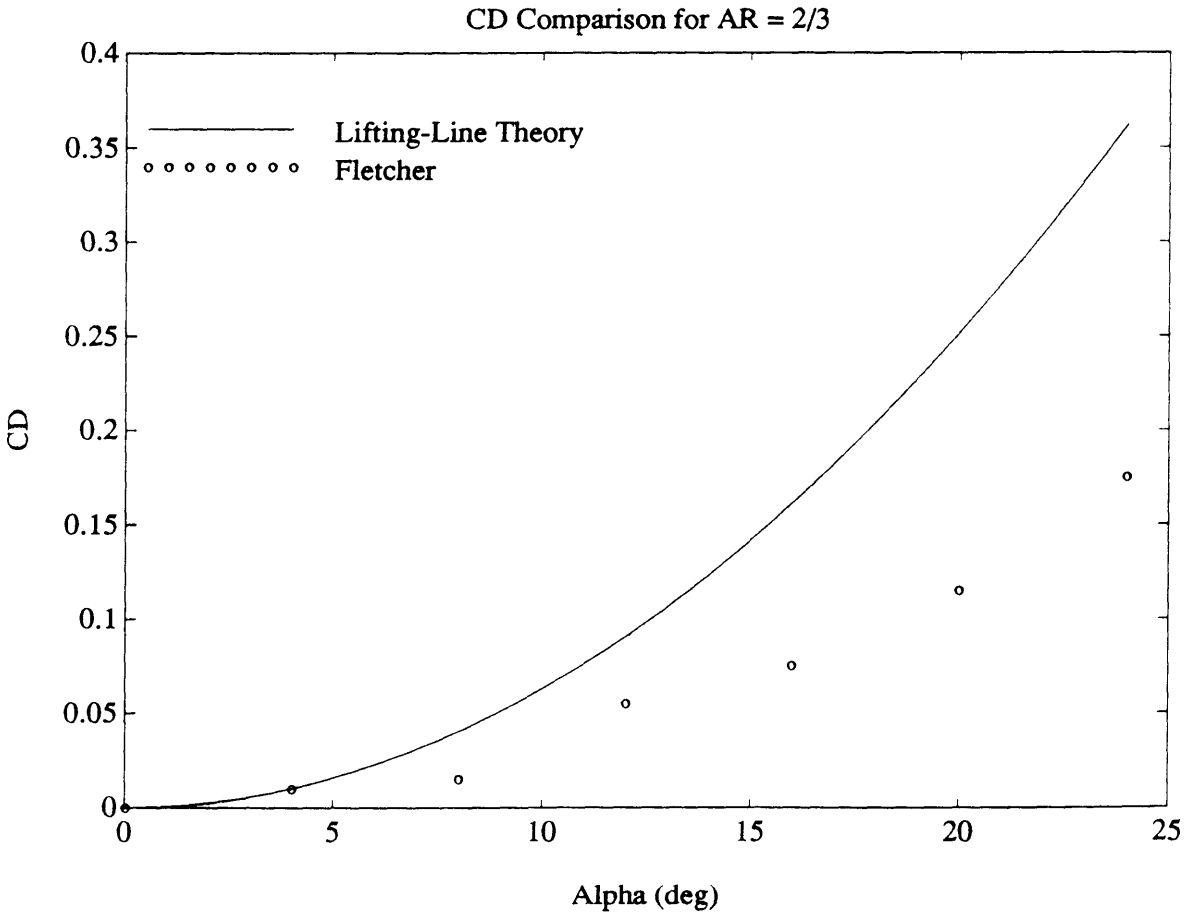

Figure 3-18: CD Comparison for AR = 2/3

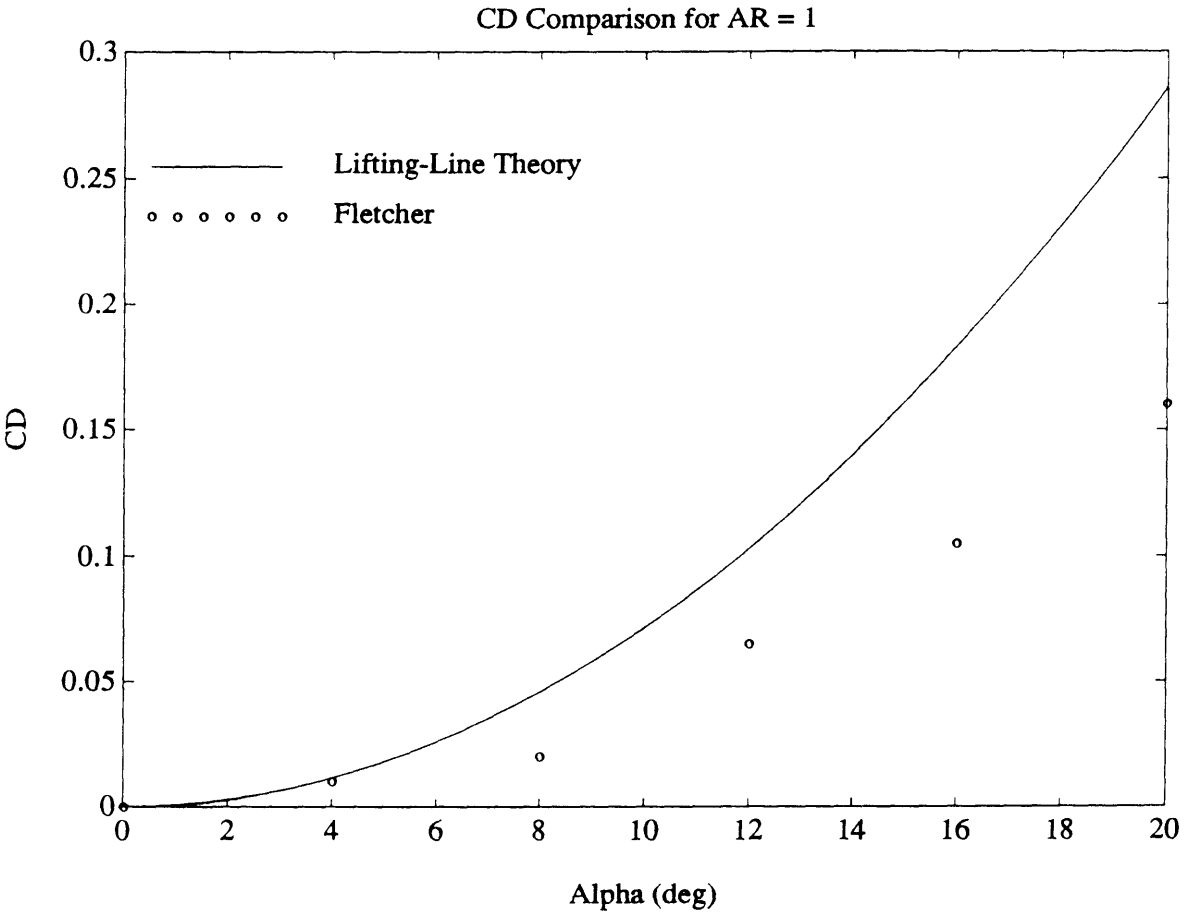

Figure 3-19: CD Comparison for AR = 1

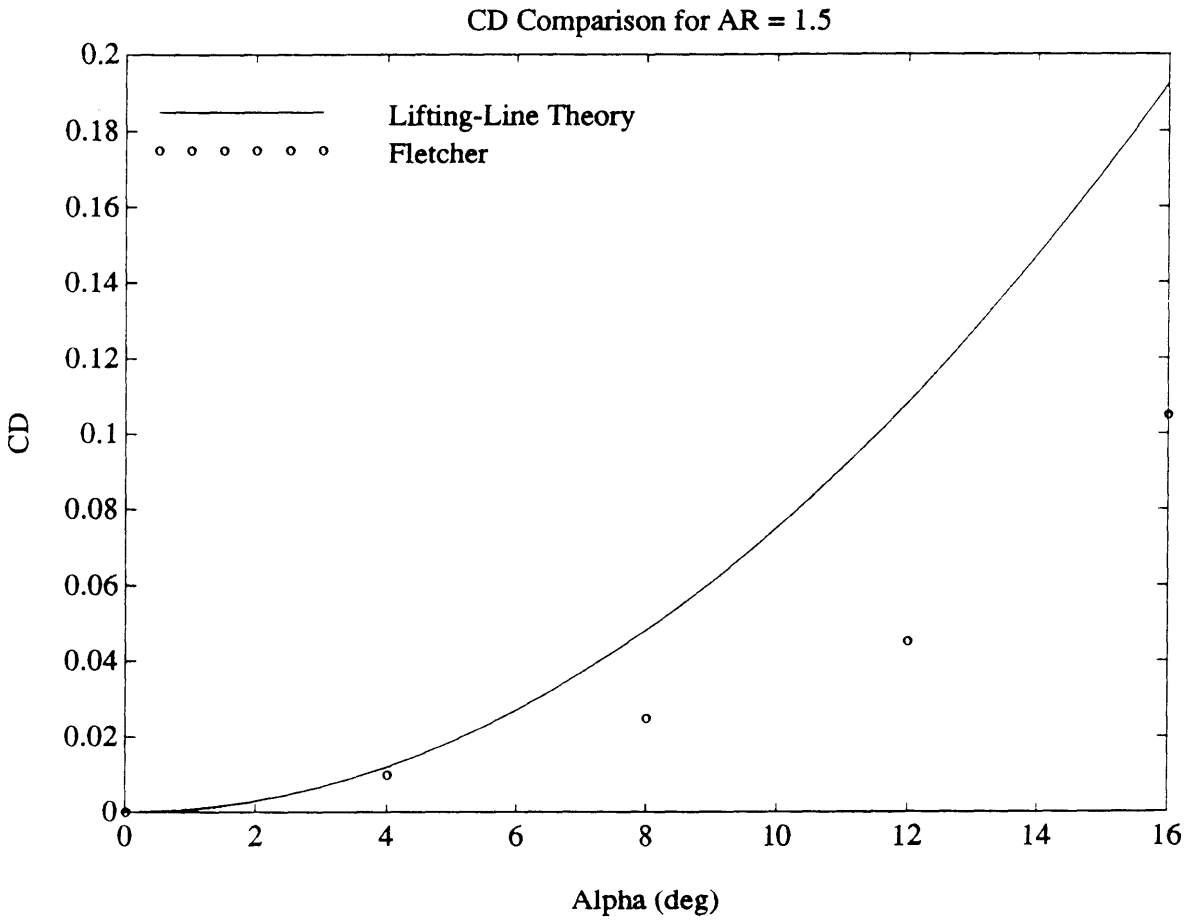

Figure 3-20: CD Comparison for AR = 1.5

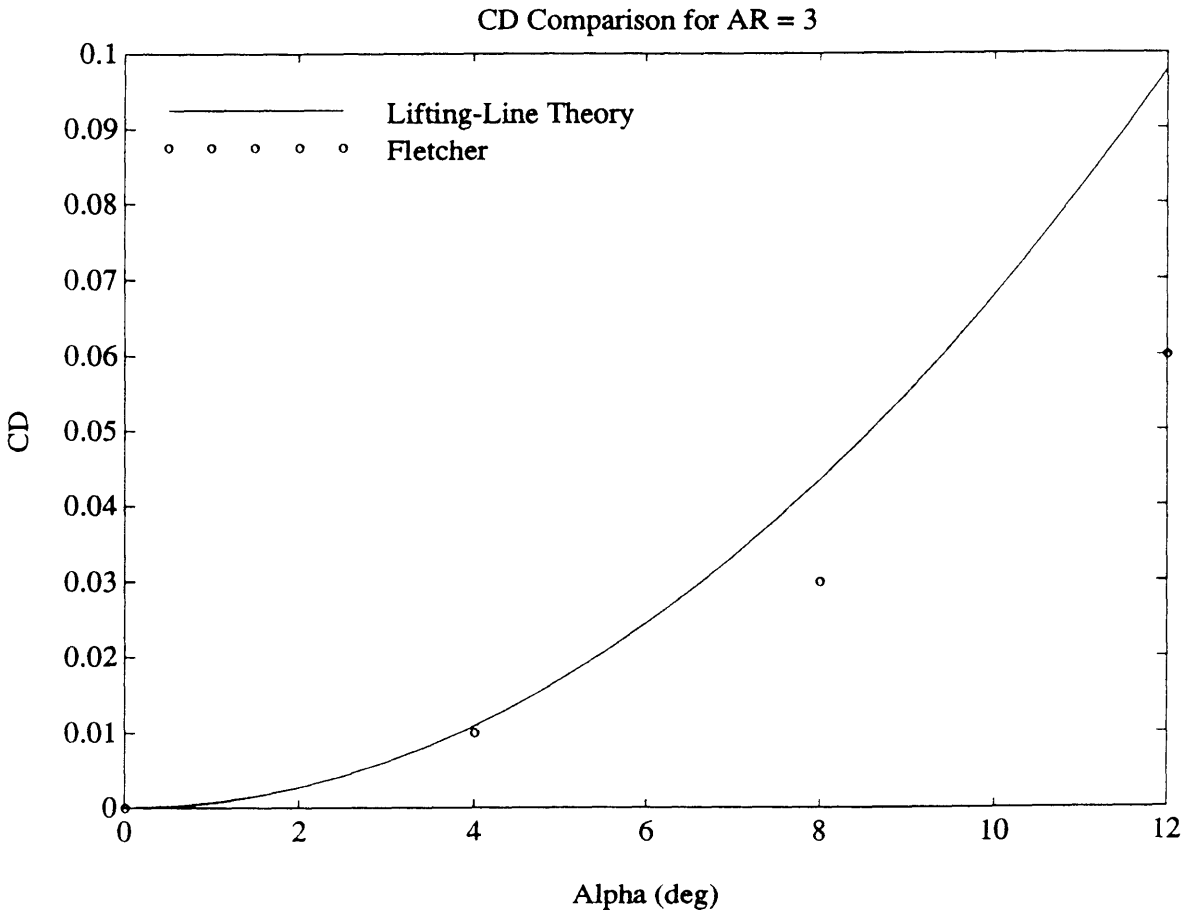

Figure 3-21: CD Comparison for AR = 3

become invalid once the flow is separated or stalled.

It can be seen from the C_L comparisons that the lifting-line theory from [16] and [17] is the most accurate. The lifting-line theory derived here and in [14], [15] show consistently larger values than the experimental data, suggesting that the use of the sectional lift properties to determine the vortex strength overestimates the lift compared with that obtained by satisfying downwash conditions at the three-quarter chord point. Another observation to be made is that as the aspect ratio increases, as in Figures 3-15 and 3-16, the lifting-line theories give results that begin to coincide, gradually moving closer to the strip theory measurement. Therefore, increasing aspect ratio moves into the regime where the lifting-line theory derived here is most appropriate, and eventually into the regime where three-dimensional effects can be ignored, so that strip theory is sufficient to describe the lifting characteristics. The lifting-line results are surprisingly good considering the low aspect ratios. Of course, if the aspect ratio had been defined as the circumference divided by the chord (i.e. $2\pi r/c$), its numerical value would have been much larger.

The C_{D_i} comparisons do not convey as much information, except to show that the lifting-line theory gives results that are satisfactory for small angles of attack ($\leq 4^o$), but become progressively worse as angle of attack increases probably due to viscous effects that lifting-line theory cannot include. The effect of aspect ratio is also not as immediately apparent.

The conclusion that can be made from these comparisons is that the lifting-line theory for annular wings derived in this thesis will be adequate to describe the lifting characteristics of the annular wings to be used in the configurations previously detailed in the Examples Chapter, as long as the angle of attack of the surface is not large ($\leq 8^o$), and the aspect ratio is not too small (≥ 0.75).

3.3 Modal Control Analysis

The other aspect of the thesis that required preliminary analysis work dealt with obtaining analytical expressions suitable to represent the first bending mode of the

vehicle. Both practical configurations described in the Examples Chapter required such an analysis, and the resulting equations are very similar. These equations were then to be used to define a control system that would regulate the bending deformation. The procedure for this was slightly different for each configuration, however. The maglev configuration already possessed a non-linear simulation that included a LQR controller, so the equations that defined the simulation and the controller would have to be augmented to include the flexible mode. On the other hand, there was no such simulation to represent the towed vehicle, so all the equations needed would have to be derived, then have a controller applied to them. The modal analysis for each vehicle, and a summary of the controller theory, are presented below.

3.3.1 Modal Analysis of the Towed Vehicle

It was beneficial to perform the analysis work for the towed vehicle first because the primary concern in the analysis of this vehicle was control of the first longitudinal mode, whereas the maglev vehicle simulation incorporated many more factors into its dynamic model. As a result, the equations produced by the modal analysis of the towed vehicle would be simpler, but could be modified and incorporated later into the simulation of the maglev vehicle.

The towed vehicle, as seen in Figure 3-22, is set up as two rigid bodies connected by a hinge that contains a torsional spring. This hinge and spring system allows the system to only deflect in the longitudinal direction. Another constraint on the dynamics of the vehicle is a tow cable attached from the towed vehicle to the aircraft that is pulling the vehicle along. This is represented in the analysis as a tension, F, the towing force that provides the lift for the towed body.

Before the equations of motion are to be formulated, there are some terms defined in Figure 3-22 that require further explanation [20]. The simulation involves only motions in the longitudinal plane, and the flexible mode is represented by a simple torsional stiffness connecting the foreward and aft body sections, as seen in Figure 3-23.

The points G, P, A, and C define the non-deformed body center of gravity, the

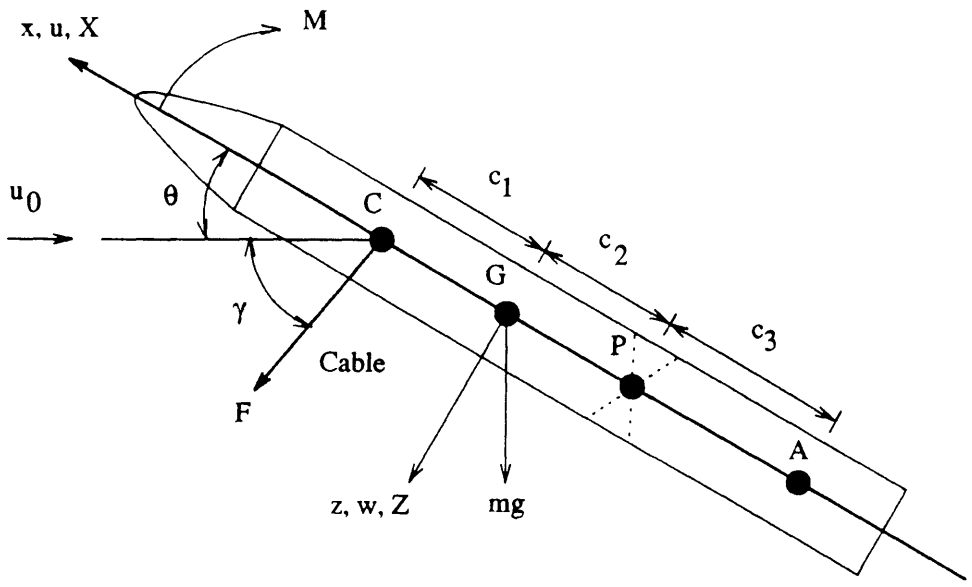

Figure 3-22: Towed Vehicle With Forces and Moments

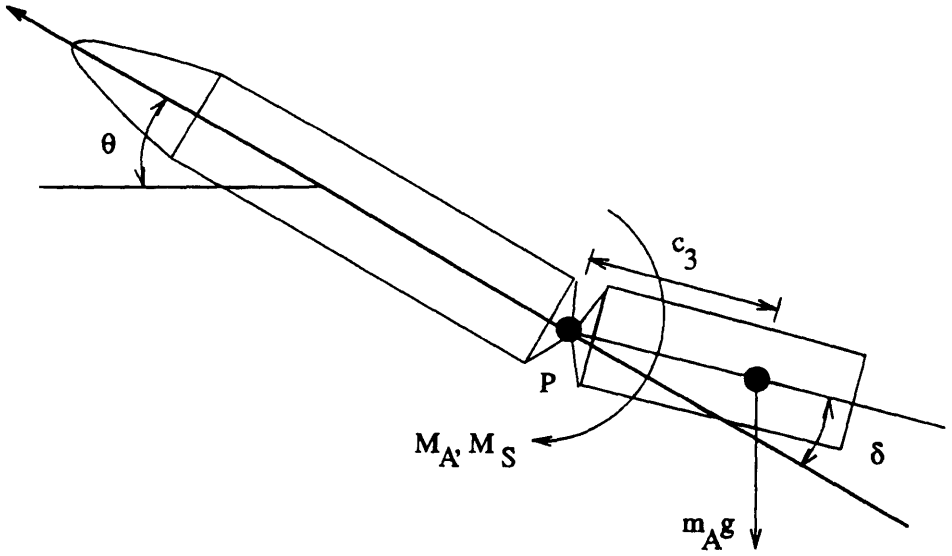

Figure 3-23: Towed Vehicle With Single Bending Mode

effective center of rotation for the bending mode, the center of gravity of the lumped mass aft body, and the cable attachment point, respectively.

The mass and inertia terms are represented by m, which is the complete vehicle mass, m_A, which is the aft body mass, B, which is the pitch moment of inertia for the complete vehicle about its center of gravity, and B_A, which is the pitch moment of inertia for the aft body about P, its center of rotation.

The force and moment terms are represented by X and Z, which are the complete vehicle aerodynamic forces, M, which is the complete vehicle aerodynamic pitching moment about the center of gravity, M_A, which is the aft body aerodynamic moment about the point P, and M_S, which is the torque caused by the effective torsional spring at P.

Other important terms are represented by δ, which is the angular deflection of the aft body relative to the vehicle centerline, as seen in Figure 3-23 and γ, which is the angle between the absolute horizontal and the cable direction.

Using these terms, the complete body equations of motion are ([20], [21]):
In the X-direction

$$m\dot{u} = X + F\cos(\theta + \gamma) - mg\sin\theta \tag{3.65}$$

In the Z-direction

$$m(\dot{w} - uq) = Z + F\sin(\theta + \gamma) + mg\cos\theta + m_A c_3 \ddot{\delta} \tag{3.66}$$

And around the Y-axis

$$B\ddot{\theta} = M - c_2 F\sin(\theta + \gamma) + (B_A + m_A c_1 c_3)\ddot{\delta} \tag{3.67}$$

In these equations, δ is assumed to be a small angle, and $q = \dot{\theta}$. An important point to note in these equations is the presence of additional inertia terms reulting from the motion of the aft body independently of the fore body.

An additional equation is required to determine the deflection angle δ. This is obtained from the torque balance about P for the aft body alone, and the resulting expresssion is

$$B_A(\ddot{\theta} - \ddot{\delta}) = M_A + M_S + m_A c_3 g \tag{3.68}$$

where the spring torque M_S can be related to δ using

$$M_S = k\delta$$

The spring constant k can be obtained by assuming a natural frequency for the bending mode, as will be shown later.

The equations can now be simplified by making the assumptions that θ is small, and the body is being towed at its center of gravity, i.e. $c_2 = 0$. Applying these assumptions produces the equations

$$\begin{aligned}
m\dot{u} &= X + F(\cos\gamma - \theta\sin\gamma) - mg\theta \\
m(\dot{w} - u_0 q) &= Z + F(\sin\gamma + \theta\cos\gamma) + mg + m_A c_3 \ddot{\delta} \\
B\ddot{\theta} &= M + (B_A + m_A c_1 c_3)\ddot{\delta} \\
q &= \dot{\theta} \\
B_A(\ddot{\theta} - \ddot{\delta}) &= M_A + k\delta + m_A c_3 g
\end{aligned}$$

Now, in order to apply a linear controller to the equations, they must be linearized about a trim point. This must be done by substituting into the equations the steady-state (trim) and perturbation values of the angles, forces and moments:

$$\begin{aligned} X &= X_0 + \bar{X} \\ Z &= Z_0 + \bar{Z} \\ \theta &= \theta_0 + \bar{\theta} \\ \delta &= \delta_0 + \bar{\delta} \\ M &= M_0 + \bar{M} \\ M_A &= M_{A0} + \bar{M}_A \end{aligned}$$

where the zero subscript denotes a trim value and bar denotes a pertubation quantity.

Using these equations, and the further assumption that the cable dynamics are uncoupled so that F and γ are invariant, gives the steady conditions as

$$\begin{aligned} X_0 + F(\cos\gamma - \theta_0 \sin\gamma) - mg\theta_0 &= 0 \\ Z_0 + F(\sin\gamma + \theta_0 \cos\gamma) - mg &= 0 \\ M_0 &= 0 \\ M_{A0} + k\delta_0 + m_A c_3 g &= 0 \end{aligned}$$

so, the dynamic, linear equations become

$$\begin{aligned} m\dot{u} &= \bar{X} - \bar{\theta}(F\sin\gamma + mg) \\ m(\dot{w} - u_0 q) &= \bar{Z} + \bar{\theta} F\cos\gamma + m_A c_3 \ddot{\bar{\delta}} \\ B\ddot{\bar{\theta}} &= \bar{M} + (B_A + m_A c_1 c_3)\ddot{\bar{\delta}} \\ q &= \dot{\bar{\theta}} \\ B_A(\ddot{\bar{\theta}} - \ddot{\bar{\delta}}) &= \bar{M}_A + k\bar{\delta} \end{aligned}$$

Now, using the definitions

$$L_v = F \sin\gamma + mg$$

as the net vehicle steady lift,

$$D_v = F \cos\gamma$$

as the net vehicle steady drag, and

$$B_1 = B_A + m_A c_1 c_3$$

as the net aft vehicle inertia, and dropping the bar notation for perturbation quantities, the equations may be summarized as

$$\begin{aligned} m\dot{u} &= X - \theta L_v \\ m(\dot{w} - u_0 q) &= Z + \theta D_v + m_A c_3 \ddot{\delta} \\ B\dot{q} &= M + B_1 \ddot{\delta} \\ q &= \dot{\theta} \\ B_A(\dot{q} - \ddot{\delta}) &= M_A + k\delta \end{aligned}$$

and, if the rate of deflection is designated as $\nu = \dot{\delta}$, the equations can be rearranged into a final form as

$$m\dot{u} = X - \theta L_v \tag{3.69}$$

$$m\dot{w} = mu_0 q + Z + \theta D_v + m_A c_3 G \tag{3.70}$$

$$\dot{\theta} = q \tag{3.71}$$

$$B\dot{q} = M + B_1 G \tag{3.72}$$

$$\dot{\delta} = \nu \tag{3.73}$$

$$\dot{\nu} = G \tag{3.74}$$

where,

$$G = \frac{B_A M - B(M_A + k\delta)}{(B - B_1)B_A}$$

The next step is to break up the aerodynamic terms into their derivatives in the following manner

$$\begin{aligned} X &= X_u u + X_w w \\ Z &= Z_u u + Z_w w + Z_\delta \delta \\ M &= M_w w + M_q q + M_\delta \delta + M_\nu \nu + M_\eta \eta + M_\xi \xi \\ M_A &= M_{Aw} w + M_{Aq} q + M_{A\delta} \delta + M_{A\nu} \nu + M_{A\xi} \xi \end{aligned}$$

where $X_u = \frac{\partial X}{\partial u}$, $X_w = \frac{\partial X}{\partial w}$, etc., and η and ξ are the control surface deflections. The η control surface is implemented directly using the control flaps within the annular wings, while the ξ control surface is specifically dedicated to damping the flexible mode by using the same control surfaces η, but deflecting them in opposing directions to exert moments on the center of the vehicle.

Another modification that should be made to the equations accounts for the presence of vertical wind gust disturbances. These disturbance terms are of the form $D_w = Z_w w_F$ and $D_q = M_w w_F$, representing the vertical force and pitching moment, respectively, induced by a gust of velocity w_F. The force and moment terms must then be added to Equations (3.70) and (3.72) to ensure that gust disturbances can be input into the state-space system.

If the states are then defined as u, w, θ, q, δ, and ν, the above equations of motion can be arranged in state-space form, suitable for control system analysis.

Rearranging the equations in state-space form gives:

$$\dot{\mathbf{x}} = \mathbf{A}\mathbf{x} + \mathbf{B}\mathbf{u} + \mathbf{L}w_F \tag{3.75}$$

or

$$\begin{bmatrix} \dot{u} \\ \dot{w} \\ \dot{\theta} \\ \dot{q} \\ \dot{\delta} \\ \dot{\nu} \end{bmatrix} = \begin{bmatrix} a_{11} & a_{12} & a_{13} & 0 & 0 & 0 \\ a_{21} & a_{22} & a_{23} & a_{24} & a_{25} & a_{26} \\ 0 & 0 & 0 & a_{34} & 0 & 0 \\ 0 & a_{42} & 0 & a_{44} & a_{45} & a_{46} \\ 0 & 0 & 0 & 0 & 0 & a_{56} \\ 0 & a_{62} & 0 & a_{64} & a_{65} & a_{66} \end{bmatrix} \begin{bmatrix} u \\ w \\ \theta \\ q \\ \delta \\ \nu \end{bmatrix} + \begin{bmatrix} 0 & 0 \\ b_{21} & b_{22} \\ 0 & 0 \\ b_{41} & b_{42} \\ 0 & 0 \\ b_{61} & b_{62} \end{bmatrix} \begin{bmatrix} \eta \\ \xi \end{bmatrix} + \begin{bmatrix} 0 \\ l_2 \\ 0 \\ l_4 \\ 0 \\ 0 \end{bmatrix} w_F$$

where the matrix terms are defined by

$$\begin{aligned}
a_{11} &= \frac{1}{m} X_u \\
a_{12} &= \frac{1}{m} X_w \\
a_{13} &= -\frac{1}{m} L_v \\
a_{21} &= \frac{1}{m} Z_u \\
a_{22} &= \frac{1}{m} Z_w + \frac{m_A}{m} c_3 \left[\frac{B_A M_w - B M_{Aw}}{(B - B_1) B_A} \right] \\
a_{23} &= \frac{1}{m} D_v \\
a_{24} &= u_0 + \frac{m_A}{m} c_3 \left[\frac{B_A M_q - B M_{Aq}}{(B - B_1) B_A} \right] \\
a_{25} &= \frac{1}{m} Z_\delta + \frac{m_A}{m} c_3 \left[\frac{B_A M_\delta - B(M_{A\delta} + k)}{(B - B_1) B_A} \right] \\
a_{26} &= \frac{m_A}{m} c_3 \left[\frac{B_A M_\nu - B M_{A\nu}}{(B - B_1) B_A} \right] \\
a_{34} &= 1 \\
a_{42} &= \frac{M_w}{B} + \frac{B_1}{B} \left[\frac{B_A M_w - B M_{Aw}}{(B - B_1) B_A} \right] \\
a_{44} &= \frac{M_q}{B} + \frac{B_1}{B} \left[\frac{B_A M_q - B M_{Aq}}{(B - B_1) B_A} \right] \\
a_{45} &= \frac{M_\delta}{B} + \frac{B_1}{B} \left[\frac{B_A M_\delta - B(M_{A\delta} + k)}{(B - B_1) B_A} \right] \\
a_{46} &= \frac{M_\nu}{B} + \frac{B_1}{B} \left[\frac{B_A M_\nu - B M_{A\nu}}{(B - B_1) B_A} \right] \\
a_{56} &= 1
\end{aligned}$$

$$
\begin{aligned}
a_{62} &= \frac{B_A M_w - B M_{Aw}}{(B - B_1)B_A} \\
a_{64} &= \frac{B_A M_q - B M_{Aq}}{(B - B_1)B_A} \\
a_{65} &= \frac{B_A M_\delta - B M_{A\delta}}{(B - B_1)B_A} \\
a_{66} &= \frac{B_A M_\nu - B M_{A\nu}}{(B - B_1)B_A} \\
b_{21} &= \frac{m_A}{m} c_3 \frac{M_\eta}{(B - B_1)} \\
b_{41} &= \frac{M_\eta}{(B - B_1)} \\
b_{61} &= \frac{M_\eta}{(B - B_1)} \\
b_{22} &= \frac{m_A}{m} c_3 \left[\frac{B_A M_\xi - B M_{A\xi}}{(B - B_1)B_A} \right] \\
b_{42} &= \frac{M_\xi}{B} + \frac{B_1}{B} \left[\frac{B_A M_\xi - B M_{A\xi}}{(B - B_1)B_A} \right] \\
b_{62} &= \frac{B_A M_\xi - B M_{A\xi}}{(B - B_1)B_A} \\
l_2 &= \frac{Z_w}{m} \\
l_4 &= \frac{M_w}{B}
\end{aligned}
$$

Obtaining the stability derivatives requires slightly more work. They are configuration dependent, but are essential to the analysis, so the general expressions for the towed vehicle stability derivatives will be derived here, while numerical values will be given in the Results Chapter.

To make the calculations easier, Figure 3-24 defines a number of geometric parameters that will be used in evaluating the stability derivatives. Geometric parameters for the fore annular wing include the radius R_F, the chord c_F, the reference surface area $S_F = 2R_F c_F$, and the aspect ratio $A_F = 2R_F/c_F$. Geometric parameters for the aft annular wing include the radius R, the chord c, the reference surface area $S = 2Rc$, and the aspect ratio $A = 2R/c$. Also defined in the figure are the distances from the wing center of gravity to the vehicle center of gravity for each wing, where l_F pertains to the fore wing and l pertains to the aft wing.

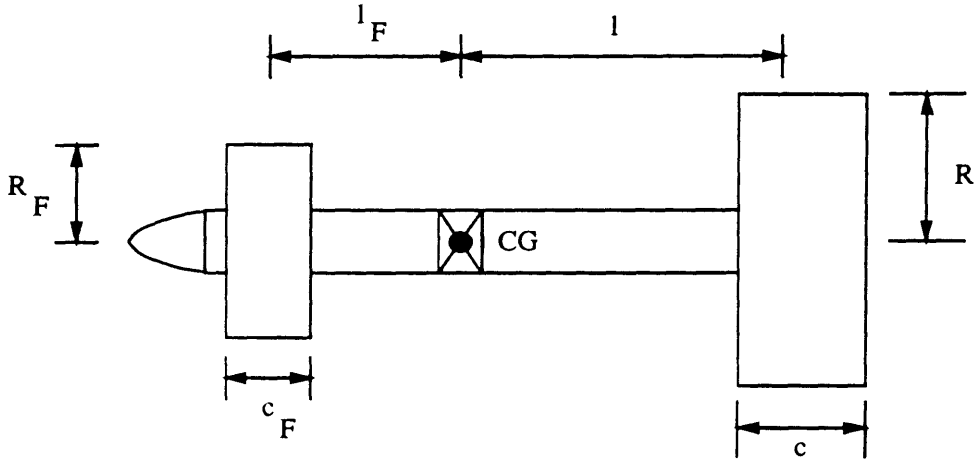

Figure 3-24: Towed Body Geometry

Other assumptions must be made about some of the modal quantities defined above. It will be assumed that the tow point of the vehicle is located at the vehicle center of gravity ($c_1 = 0$), and the flexible joint of the vehicle is located at the center of gravity ($c_2 = 0$). However, non-zero terms do persist in the form of c_3, the aft body center of gravity location, m, the total body mass, and m_A, the aft body mass [20].

Now, if the body contribution to the lift is neglected and the lift is given by L_v as defined above, then the vehicle coefficient of lift is given as

$$C_{L_v} = \frac{L_v}{\frac{1}{2}\rho U_0^2 \mathcal{S}}$$

and, defining subscripts as $()_v$ for the complete vehicle, $()_A$ for the aft wing, and $()_F$ for the fore wing, then, for the entire vehicle,

$$\left(\frac{\partial C_L}{\partial \alpha}\right)_v = \frac{\pi^2 A}{(\frac{\pi}{2} + A)} + \frac{\mathcal{S}_F}{\mathcal{S}} \frac{\pi^2 A_F}{\frac{\pi}{2} + A_F}$$

Also for the complete vehicle,

$$C_{D_v} = C_{D_0} + \frac{C_{L_v}^2}{\pi A}$$

Using these quantities, the resulting stability derivatives are [22]

$$\begin{aligned}
X_u &= -\rho U_0 S C_{D_v} \\
X_w &= \frac{1}{2}\rho U_0 S \left[C_{L_v} - \left(\frac{\partial C_D}{\partial \alpha} \right)_v \right] \\
Z_u &= -\rho U_0 S C_{L_v} \\
Z_w &= -\frac{1}{2}\rho U_0 S \left[\left(\frac{\partial C_L}{\partial \alpha} \right)_v + C_{D_v} \right] \\
Z_\delta &= \frac{1}{2}\rho U_0^2 S \left(\frac{\partial C_L}{\partial \alpha} \right)_A \\
M_w &= -\frac{1}{2}\rho U_0 S l \left[\left(\frac{\partial C_L}{\partial \alpha} \right)_A - \frac{l_F}{l}\frac{S_F}{S} \left(\frac{\partial C_L}{\partial \alpha} \right)_F \right] \\
M_q &= -\frac{1}{2}\rho U_0 S l^2 \left[\left(\frac{\partial C_L}{\partial \alpha} \right)_A + \left(\frac{l_F}{l} \right)^2 \frac{S_F}{S} \left(\frac{\partial C_L}{\partial \alpha} \right)_F \right] \\
M_\delta &= \frac{1}{2}\rho U_0^2 S l \left(\frac{\partial C_L}{\partial \alpha} \right)_A \\
M_\nu &= \frac{1}{2}\rho U_0 S l^2 \left(\frac{\partial C_L}{\partial \alpha} \right)_A \\
M_{Aw} &= -\frac{1}{2}\rho U_0 S l \left(\frac{\partial C_L}{\partial \alpha} \right)_A \\
M_{Aq} &= -\frac{1}{2}\rho U_0 S l^2 \left(\frac{\partial C_L}{\partial \alpha} \right)_A \\
M_{A\delta} &= M_\delta \\
M_{A\nu} &= M_\nu
\end{aligned}$$

The control surface stability derivative M_η, requires definition of the effective control surface aspect ratio as $A_c = 2R_F/c_F$ and the effective control surface area as $S_\eta = 2R_F c_F$. The lift curve slope of the control surface can be obtained from

$$\frac{\partial C_L}{\partial \eta} = \frac{2\pi A_c}{(2 + A_c)}$$

so, the pitch control derivative is given by

$$M_\eta = \frac{1}{2}\rho U_0^2 \mathcal{S} l \frac{l_F}{l} \frac{S_F}{\mathcal{S}} \frac{\partial C_L}{\partial \eta}$$

The bending mode control derivatives are produced as pure torques at the forward and rear control surfaces by using plain flaps to change the effective section camber. The associated control derivatives are given by:

$$M_\xi = -\frac{1}{2}\rho U_0^2 \mathcal{S} l \frac{\partial C_M}{\partial \xi}$$

where $M_{A\xi} = -M_\xi$.

Each of these stability derivatives is numerically evaluated in the Results Chapter to obtain values for the state-space matrices **A**, **B**, and **L**.

3.3.2 Modal Analysis of the Magnetically Levitated Vehicle

The magnetically levitated vehicle analysis followed a slightly different path than that of the towed vehicle. As a set of dynamic equations was already in place because of the pre-existing nonlinear simulation, the procedure was to modify the original equations by adding in the term produced by a flexible mode, thus increasing the number of degrees of freedom present in the simulation from six to seven. A basic model for this term was obtained from the analysis performed on the towed vehicle, then modified to conform to the configuration of the maglev vehicle.

As the simulation uses the original six degree-of-freedom dynamic model as a basis for comparison, it is beneficial to show the original equations of motion in their full original form. A full description can be found in [4], but some of the terms are defined here. The vehicle is suspended magnetically on four levitation coils and has two propulsion coils, one at the front and one at the back. The gaps between the coils and track can be related to the instantaneous vehicle position and attitude in inertial space, and the track configuration (e.g. banked turn, deflection between supports, roughness, etc.). The resultant magnetic forces are non-linear functions of the gaps

and deviations. These are defined for the n_{th} coil as:

n_{th} levitation coil gap increase:

$$h_n = (z - l_{xcn}\theta - z_{Tn})\cos\theta_{cn} - (y + l_{xcn}\psi - \phi s - y_{Tn})\sin\theta_{cn}$$

n_{th} propulsion coil gap increase:

$$b_n = z - l_{xpn}\theta - z_{pn}$$

n_{th} propulsion coil lateral deviation:

$$yb_n = y + l_{xpn}\psi + (R - s)\phi$$

The six dynamic equations of the rigid body are presented as Equations (3.76) through (3.81). In these equations, subscript A refers to an aerodynamic contribution, subscript M refers to a magnetic term, and subscript G refers to a wing gust input.

X Force Equation:

$$m\dot{u} = -m\dot{u}_0 - D_A - D_M + mg(a_F + \theta\cos\phi_0(t)) \tag{3.76}$$

where,

$$\begin{aligned} D_A &= \frac{1}{2}\rho(u + u_G + u_0)^2 S_R C_D \\ D_M &= k_{DL}\sqrt{\frac{u_R}{u + u_0}}\frac{mg}{n_L}\sum_{n=1}^{n_L}\left(\frac{h_0}{h_0 + h_n}\right)^{\epsilon_L} \\ T &= T_0\sum_{n=1}^{n_P}\left(\frac{b_0}{b_0 + b_n}\right)^{\epsilon_P} \end{aligned}$$

Z Force Equation:

$$m\dot{w} = mu_0 q + Z_M + Z_A - mga_z \tag{3.77}$$

where,

$$\begin{aligned} Z_A &= \frac{1}{2}\rho \mathcal{S}_w C_{L_\alpha}\{(u+u_0)^2\alpha_z + u_0(2u_G + w_G)\} \\ Z_M &= \frac{mg}{n_L \cos\theta_c}\sum_{n=1}^{n_L}\left(\frac{h_0}{h_0+h_n}\right)^{\epsilon_L}\cos\theta_{cn} \\ a_z &= (1-a_V)\cos\phi_0 + a_H \sin\phi_0 \end{aligned}$$

Pitch Moment Equation:

$$B\dot{q} = -B\dot{q_0} + M_M + M_A \tag{3.78}$$

where,

$$\begin{aligned} M_M &= -\frac{mg}{n_L \cos\theta_c}\sum_{n=1}^{n_L}\left(\frac{h_0}{h_0+h_n}\right)^{\epsilon_L} l_{xcn}\cos\theta_{cn} \\ &+ (R\cos\theta_c - s)D_M - (R-s)T \\ M_A &= -(s-s_A)D_A + \frac{1}{2}\rho \mathcal{S}_w l_w C_{L_\alpha}\{(u+u_0)^2\alpha_p + u_0(2u_G + w_G - q l_w)\} \end{aligned}$$

Y Force Equation:

$$m(\dot{v} - u_0 r) = Y_M + Y_A + mg\{a_H\cos\phi_0 - (1-a_V)\sin\phi_0\} \tag{3.79}$$

where,

$$\begin{aligned} Y_A &= \frac{1}{2}\rho(u+u_G+u_0(t))^2 \mathcal{S}_w C_{L_\alpha}\alpha_y + \frac{1}{2}\rho u_0(t) v_G(\mathcal{S}_w C_{L_\alpha} + \mathcal{S}_B C_{L_{\alpha B}}) \\ Y_M &= -\frac{mg}{n_L\cos\theta_c}\sum_{n=1}^{n_L}\left(\frac{h_0}{h_0+h_n}\right)^{\epsilon_L}\sin\theta_{cn} + \sum_{n=1}^{n_p} Y_{mkn} \end{aligned}$$

Yaw Moment Equation:

$$C(\dot{r} + \dot{r_0}) = N_M + N_A \tag{3.80}$$

where,

$$\begin{aligned} N_M &= -\frac{mg}{n_L\cos\theta_c}\sum_{n=1}^{n_L}\left(\frac{h_0}{h_0+h_n}\right)^{\epsilon_L} l_{xcn}\sin\theta_{cn} + \sum_{n=1}^{n_P} Y_{mkn} l_{xpn} \\ N_A &= \frac{1}{2}\rho(u+u_0(t))^2 \mathcal{S}_w l_w C_{L_\alpha}\alpha_{ya} + \frac{1}{2}\rho u_0(t) v_G(\mathcal{S}_w l_w C_{L_\alpha} + \mathcal{S}_B l_B C_{L_{\alpha B}}) \end{aligned}$$

Roll Moment Equation:

$$A(\dot{p} + \dot{p_0}) = L_M + L_A \tag{3.81}$$

where,

$$\begin{aligned} L_M &= \frac{mg}{n_L \cos\theta_c} \sum_{n=1}^{n_L} \left(\frac{h_0}{h_0 + h_n} \right)^{\epsilon_L} s \sin\theta_{cn} + (R - s) \sum_{n=1}^{n_P} Y_{mkn} \\ L_A &= \frac{1}{2}\rho(u + u_0(t))^2 S_w l_{wR} C_{L_a} \alpha_{ro} + \frac{1}{2}\rho u_0(t) v_G S_B s_A C_{L_{aB}} \end{aligned}$$

In these equations, u_0 is the velocity along the track, ϕ_0 is the instantaneous track bank angle, and a_F, a_V, and a_H are the acceleration components resulting when the vehicle exactly follows the track centerline at a constant separation height h_0. The control surface deflections are α_z, α_p, α_y, α_{ya}, and α_{ro}. R is the height of the magnetic center above the track, while s and s_A are the distances of the center of gravity and aerodynamic center, respectively, below the magnetic center. The Y_{mkn} terms are the magnetic side forces due to lateral movement relative to the track, and are non-linear functions of yb_n.

The body attitude angle perturbations must always be small, and the velocities can be related by:

$$\dot{x} = u \tag{3.82}$$

$$\dot{y} = v \tag{3.83}$$

$$\dot{z} = w \tag{3.84}$$

$$\dot{\phi} = p \tag{3.85}$$

$$\dot{\theta} = q \tag{3.86}$$

$$\dot{\psi} = r \tag{3.87}$$

The equations outlined above describe the six degree-of-freedom rigid body dynamics. They are modified for the bending mode using flexibility terms similar to those derived in the analysis of the towed vehicle. The following specifications are used:

The bending mode is represented as a torsional spring connecting the forward and aft body sections.

The torsional spring and center of gravity of the complete vehicle are co-located at the mid-point, and the vehicle is dynamically symmetric about this point.

Bending is assumed only in the pitch plane, i.e. the vehicle is laterally rigid.

θ is the pitch attitude of the forebody and δ is the angle between the fore and aft body reference axes, similar to the definitions shown in Figure 3-23.

The expressions for the levitation and propulsion coil gap changes will be modified. For a layout with four levitation coils ($n_L = 4$) and two propulsion coils ($n_P = 2$), then each set of coils (fore, aft) would be located at a different vertical position on the track if the flexibility at the center were taken into account. The expressions for the gaps of the front coils ($n_L = 1, 2$ and $n_P = 1$) would remain unchanged, as δ is defined as the relative angle made between the rear and front half of the vehicle, but the expressions for the gaps of the rear coils ($n_L = 3, 4$ and $n_P = 2$) would have the following gap change modifications, where the gaps are as defined above:

$$\begin{aligned} h_n &= (z - l_{xc}(\theta - \delta) - z_{Tn})\cos\theta_{cn} - (y + l_{xc}\psi - \phi s - y_{Tn}) \\ b_n &= z - l_{xp}(\theta - \delta) - z_p \\ yb_n &= y + l_{xp}\psi + (R - s)\phi \end{aligned}$$

In addition to these modifications, the flexible mode must be taken into account in the other following ways: some of the expressions dealing with the longitudinal motion of the vehicle (Z-force and pitch moment, X-force remains unchanged) must be modified to include forces and moments induced by flexible motion, and additional equations of motion concerning the deflection and its rate of change must be derived. These changes take the same form as those of the towed vehicle.

The modification to the Z-force equation comes in the form of an extra inertia term

$$m(\dot{w} - u_0(t))q = Z_M + Z_A - mg\{(1 - a_v)\cos\phi_0 + a_H \sin\phi_0\} - \frac{1}{4}ml_w\ddot{\delta} \qquad (3.88)$$

where Z_A and Z_M remain the same.

The modification of the pitch equation requires an additional inertia term in the main equation, and an adjustment to the moments produced by the aerodynamics:

$$B(\dot{q} + \dot{q}_0) = M_M + M_A + \frac{1}{2}B\ddot{\delta} \tag{3.89}$$

where,

$$M_M = -\frac{mg}{n_L \cos\theta_c} \sum_{n=1}^{n_L} \left(\frac{h_0}{h_0 + h_n}\right)^{\epsilon_L} l_{xcn} \cos\theta_{cn} + (R\cos\theta_c - s)D_M - (R - s)T$$

$$M_A = -(s - s_A)D_A + \frac{1}{2}\rho S_w l_w C_{L_\alpha}\{(u + u_0)^2(\alpha_p + \frac{\delta}{2}) + u_0(2u_G + w_G - (q - \frac{\dot{\delta}}{2})l_w)\}$$

The equation of motion for the deflection and its rate of change was obtained by using the torque balance equation about the point G for the aft body alone:

$$B_A(\ddot{\theta} + \ddot{\delta}) = M_{A_{aft}} + M_{M_{aft}} + M_S + M_C \tag{3.90}$$

where $M_{A_{aft}}$ is the aft body aerodynamic moment about G, $M_{M_{aft}}$ is the aft body magnetic moment about G, M_S is the moment induced by the torsional spring, and M_C is the moment induced by a flexible mode control surface. This control surface serves to increase the effect the control system will have upon the flexible mode by applying a stabilizing moment to the vehicle center with the purpose of damping the flexible mode. This surface may be implemented in one of two ways, both of which apply a moment directly to the center of the vehicle: Through the use of flaps in the fore and aft horizontal lifting surfaces, which when deflected in opposing directions serve to apply a moment to the center of gravity of the vehicle, or through the use of an additional horizontal control surface placed at the vehicle center of gravity. The first method has the advantage of using the existing geometry, but the moment produced is not very strong because the entire lifting surface is not dedicated to producing the moment, while the second method will produce a much larger moment, but requires a modification to the existing configuration. Either method is represented in these

equations by the same aerodynamic term, a lifting surface with a control angle of attack of α_B.

Equations (3.89) and (3.90) can be used to separate the $\ddot{\theta}$ and $\ddot{\delta}$ terms. Rearrangment gives, noting that for this configuration, $B_A = B/2$,

$$\ddot{\theta} = \frac{M_M}{B} + \frac{M_A}{B} - \dot{q}_0 + \frac{B_A}{B}\ddot{\delta}$$

and for the deflection equation:

$$\ddot{\delta} = \dot{\nu} = -2\dot{q}_0 + \frac{2}{B}(M_A + M_M) - \frac{4}{B}(M_{A_{aft}} + M_{M_{aft}} + M_S + M_C) \tag{3.91}$$

where M_A and M_M are as defined in the modified pitch equation, and

$$\begin{aligned}
M_{A_{aft}} &= \frac{1}{2}[\frac{1}{2}\rho S_w C_{L_\alpha}\{(u+u_0)^2(\alpha_p+\delta) + u_0(2u_G + w_G - (q-\nu)l_w)\}] \\
M_{M_{aft}} &= -\frac{mg}{\frac{n_L}{2}\cos\theta_c}\sum_{n=n_L/2}^{n_L}\left(\frac{h_0}{h_0+h_n}\right)^{\epsilon_L} l_{xcn}\cos\theta_{cn} \\
M_S &= k\delta = \omega_B^2\frac{B}{4}\delta \\
M_C &= \frac{1}{2}\rho S_w l_w C_{L_\alpha}(u+u_0)^2\alpha_B
\end{aligned}$$

The frequency ω_B is the flexible natural frequency of the vehicle. It will be treated as a parameter to investigate the vehicle dynamic behavior when it is low enough to be comparable with the open loop magnetic suspension natural frequencies.

With these modifications, and the additional equations for $\dot{\nu}$ and $\dot{\delta} = \nu$, the simulation can be modified to take into account the extra degree of freedom. Note that the remaining equations (Y-Force, Rolling Moment, Yawing Moment) remain unaffected, as the deformation produced by the additional degree of freedom remains confined to the longitudinal (x-z) plane. Details as to how the modified equations were incorporated into the simulation can be found in the following chapter.

3.3.3 Control Design Methodology

As stated in the introduction, it was decided that the LQR design methodology would be used to implement the modal control. A brief summary of this design methodology follows to give more insight into the logic behind the modal controller design.

The LQR design methodology is a method of optimal controller design that attempts to construct a stable controller that forces all of the states in a state-space system to go to zero from non-zero initial states. It performs this function though minimization of a predetermined quadratic cost functional that consists of weights on the states and controls. Mathematically, if the system can be expressed in the following state-space form [5]:

$$\begin{aligned} \dot{\mathbf{x}} &= \mathbf{A}\mathbf{x} + \mathbf{B}\mathbf{u} \\ \mathbf{y} &= \mathbf{C}\mathbf{x} \end{aligned}$$

then an LQR controller can be constructed if the matrices $[\mathbf{A}, \mathbf{B}]$, are stabilizable, meaning that if any modes of the system are uncontrollable through the $\mathbf{B}$ matrix, they must be stable, and the matrices $[\mathbf{A}, \mathbf{C}]$ are detectable, meaning that of any modes of the system are unobservable through the $\mathbf{C}$ matrix, they must be stable.

If the above conditions are met, and full state feedback is available, then an LQR controller can be designed using a cost functional of the form

$$J = \int_0^\infty \mathbf{x}^\mathbf{T}\mathbf{Q}\mathbf{x} + \mathbf{u}^\mathbf{T}\mathbf{R}\mathbf{u}\, dt \tag{3.92}$$

where $\mathbf{x}$ and $\mathbf{u}$ are the states and controls, respectively, $\mathbf{Q}$ is the state weighting matrix, and $\mathbf{R}$ is the control weighting matrix. The control that minimizes this function is given by the equation

$$\mathbf{u} = -\mathbf{G}\mathbf{x} = -\mathbf{R}^{-1}\mathbf{B}^\mathbf{T}\mathbf{K}$$

where $\mathbf{K}$ is the positive-definite solution to the time-invariant Control Algebraic Ric-

cati Equation (CARE):

$$\mathbf{KA} + \mathbf{A}^{\mathbf{T}}\mathbf{K} + \mathbf{Q} - \mathbf{KBR}^{-1}\mathbf{B}^{\mathbf{T}}\mathbf{K} = \mathbf{0}$$

A controller produced by this method will regulate (force to zero) the states of the system using the "path of least-resistance" dictated by minimizing the cost functional J. This path represents the way to regulate the system with the least changes in the control and states, and therefore the one requiring the least work by the hardware. The resulting controller is also guaranteed to be stable. The system matrices **A**, **B**, and **C** are dictated by the system itself and the placement of sensors that can detect the states. However, the cost functional matrices **Q** and **R** are a great deal more arbitrary, except that they must be positive semi-definite. This is where the majority of the design work must take place.

Choice of the **Q** and **R** is normally done through processes such as iteration, experimentation, or shaping of the singular values of the system to conform to performance specifications [5]. Except where noted, the method used to determine the weighting matrices in the designs presented here is known as the Bryson Method [23]. The procedure for using this method is as follows: if one has a state-space system as described above, and the maximum control derivations and the maximum tolerable output deviations can be expressed in the form

$$\begin{aligned} -u_{j_{max}} &\leq u_j(t) \leq u_{j_{max}} \\ -y_{k_{max}} &\leq y_k(t) \leq y_{k_{max}} \end{aligned}$$

then the quadratic cost functional may be expressed in the form

$$J = \int_0^\infty \left[\sum_{k=1}^{n} \left(\frac{y_k(t)}{y_{k_{max}}} \right)^2 + \rho \sum_{j=1}^{m} \left(\frac{u_j(t)}{u_{j_{max}}} \right)^2 \right] dt$$

and the **Q** and **R** are expressed as

$$\mathbf{Q} = \mathbf{C}^{\mathbf{T}}\, diag\left(\frac{1}{y_{k_{max}}}\right)^2 \mathbf{C}$$

$$\mathbf{R} = \rho\, diag\left(\frac{1}{u_{j_{max}}}\right)^2$$

This method produces two diagonal positive-definite matrices that provide greater control for the states that vary greatest. Other methods might produce better immediate results, but the Bryson Method produces adequate results for a mimiumum amount of analysis and an excellent starting point for further iteration.

Implementation of these control methodologies can be found in the Results Chapter.

Chapter 4

Simulation

The analyses described in the preceeding chapters were used in simulations to model the control systems, determine optimal feedback gains, and to test the response characteristics of the controllers. The model of the magnetically levitated vehicle provided a computer simulation from which the state-space equations were derived, while the state-space system of the towed vehicle was taken directly from the previous chapter. The results of the tests detailed in this chapter are provided in the Results Chapter.

4.1 Operation of Maglev Simulation

The simulation used to model the dynamics of the magnetically levitated vehicle was originally designed to provide results concerning how the Magneplane vehicle reacted to track disturbances, wind gusts, and to different types of track maneuvers, and the degree to which track roughness would affect the ride quality of the vehicle [4]. While these are all important considerations when dealing with the practical applications of this vehicle, this thesis is mainly concerned with evaluating the performance of the control system when an additional degree of freedom was added.

The original program was designed to have a control system that regulated the perturbations in six degrees of freedom (three translational, three rotational) and their rates about a nominal track path. During the structural design of the vehicle, it was found that the first bending frequency was comparable to the suspension frequencies,

although no modal dynamics had been included in the simulation. The structure and operation of the original simulation are described first, and the incorporation of the approximate bending mode briefly outlined.

The simulation itself is a series of programs written in MATLAB code, combined in the system of layouts shown in Figure 4-1. The primary components are a program that represents the non-linear equations of motion of the vehicle (dof6funa.m), a program that extracts the state-space models from the non-linear equations and produces the corresponding LQR controller (make_system.m), and a modified MATLAB subroutine that takes pre-determined initial conditions, track configurations, and disturbances, and uses the non-linear equations and the linear controller to provide a time simulation of the behavior of the vehicle (ode23a.m).

The twelve non-linear equations represented in 'dof6funa.m' were obtained using the original equations described in Section 3.2.2. The non-linearities arise from the expressions for the aerodynamic forces (due to the fact that $L = \frac{1}{2}\rho V^2 S C_L$ and the components of V are states) and the magnetic spring forces. The numerical values of all of the constants were obtained from a smaller subroutine named 'init_ fun_ params.m', which could be accessed when the controller was derived and when the time simulation was carried out.

The state-space model of the system was derived by 'make_ system', which obtained the state-space matrices by perturbing specified variables about the trim state specified by the numerical values presented in 'init_ fun_ params'. The **A** matrix was derived using subroutine 'makeaa.m' by perturbing the state variables appearing in the non-linear equations, the **B** matrix was obtained using 'makebb.m' by perturbing the control variables, and similarly for the disturbance variables for **G** (makegg.m). The 'LQR' subroutine of MATLAB was then applied to this state-space model to produce an LQR controller using the subroutine 'makekk.m', where the values of the weighing matrices were given by 'makeqq.m' (for **Q**) and 'makerr.m' (for **R**).

A linear simulation of the state-space model could be performed through the use of the 'lsim' subroutine within MATLAB, but in order to perform a fully dynamic non-linear simulation of the system, in was necessary to use the program 'ode23a.m'.

The program's initial inputs consisted of the following: an ideal track vector, which provided the track geometry obtained from the subprogram 'mkcv.m'and ideal speed for the vehicle (so as to ensure coordinated turns, etc.), a disturbance vector, which consisted of aerodynamic gusts, track roughness, and the periodic deflection of the track between supports, and could be made to conform to a specific frequency range (an operational bandwidth) through the use of the program 'mkdst.m'. Other inputs included the open-loop and closed-loop numerical values as dictated in 'init_ fun_ params.m', the name of the function to be integrated, the initial states, the initial and final times, and the desired accuracy. The program operated by taking the initial conditions, integrating them using second and third order Runge-Kutta formulas to obtain the states, applying the LQR controller to them, and taking the result and integrating it upon the next time step. This had the net effect of using a linear controller to control a non-linear system, with the result being a time simulation of the states and outputs.

This set of programs has been thoroughly tested and validated under a number of different test tracks and conditions (see [4] for more details), and it was deemed that the six degree-of-freedom simulation would serve well as a basis for comparison when the seven degree-of-freedom was created from it. The tests performed to confirm this are detailed in the next section. The seven degree-of-freedom model, including the modal deflection equation, was obtained readily from the original model by modifying the non-linear equations of motion to include the deflection, as shown in the modal control analysis in the previous section. This, along with some changes to the sizes of the state-space matrices, was the only change needed in the simulation (now called 'dof7funa.m').

4.2 Validity Tests for the Magnetically Levitated Vehicle

As can be ascertained from the description in the previous sections, the simulation of the dynamics of the magnetically levitated vehicle is a very complex program, made

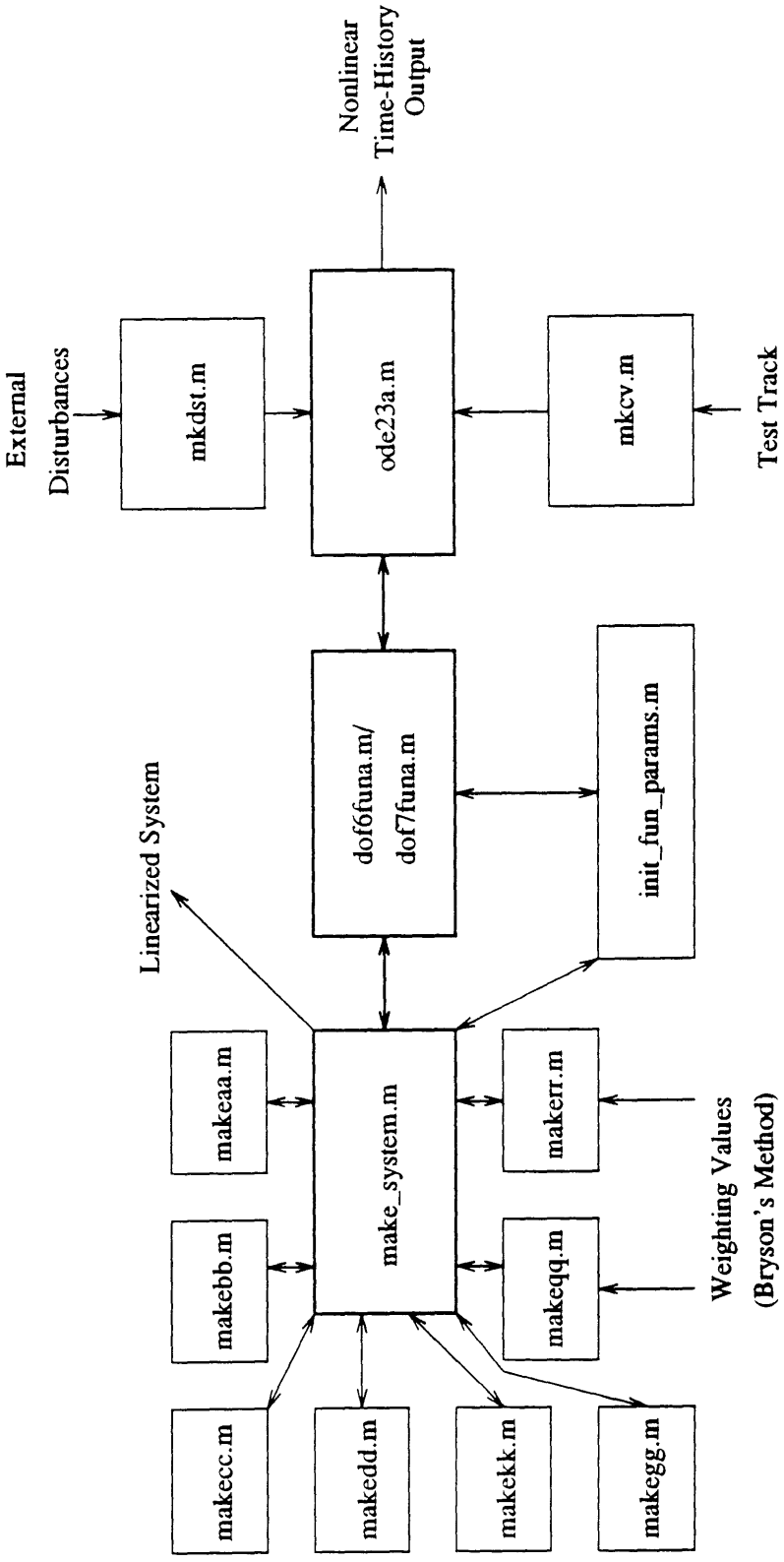

Figure 4-1: Maglev Simulation Diagram

even more complex by the modifications made to increase the degrees-of-freedom. In order to verify that the simulation accurately portrays the dynamics and resultant control of the vehicle, it was necessary to devise test cases. The procedure of the tests is described here, while their exact results are described in the Results Chapter.

The original six degree-of-freedom model had been extensively tested throughout a number of operating conditions [4], so one check on the validity of the seven degree-of-freedom model would be to see if it approached the six degree-of-freedom model under special limiting conditions. The linear equations that would be extracted from the modified simulation could then used as a reasonable approximation to the true dynamics of the flexible vehicle.

The primary special case that was tested was to tighten the torsional spring and observe whether or not the step response of the longitudinal states approached that of the unmodified simulation. The secondary test was to compare the steady-state values of both simulations. The modified non-linear simulation produces new steady states because the controller is a linear regulator working on a non-linear system, and the states are measured at the center of gravity. In the steady state the effect of gravity is to deform the vehicle, i.e. sag in the middle, even if it is by a small amount in practice.

These special cases must be satisfied as a necessary condition for the model to be used for testing the control system. The LQR controller design was implemented for the modified simulation and the performance assessed by comparing the following cases: LQR design without deflection and its rate feedback and without a bending control surface, and LQR design with inclusion of the bending mode control surface, with and without deflection and its rate.

The final measure of performance is the improvement of passenger ride quality when the vehicle is subjected to a range of disturbances such as wind gusts, turbulence, track deflection, and track roughness. To avoid the complexities of such a simulation, it was decided that the frequency response function in the form of Bode plot would provide a quicker, simpler, but equally as effective means of performance comparison.

4.3 Validity Tests for the Towed Vehicle

Unlike the magnetically levitated vehicle, the towed vehicle does not have the benefit of a prior simulation from which results may be compared, so the validity of the model must be ascertained from the behavior of the system in the time and frequency domains. However, the simulation is linear and simpler that that for the maglev vehicle, so the comparison can consist solely of displaying the effect of having two control surfaces, η and ξ, one of which is dedicated to damping the flexible mode (ξ), as opposed to only having one control surface (η). The effect of changing the flexible body mode bending frequency is also investigated.

Chapter 5

Results and Discussion

5.1 Magnetically Levitated Vehicle

The results outlined in this section concern a specific geometry, that of the Magneplane vehicle. The vehicle has six aerodynamic surfaces, three located in the forward part of the vehicle, as shown in Figure 5-1, and three located in the aft part of the vehicle, as shown in Figure 5-2.

The geometric properties of the vehicle are summarized in Table 5.1, with the following abbreviations: the wings consist of the Fore Vertical Stabilizer (FVS), the Fore Port and Starboard Horizontal Stabilizers (FPHS and FSHS), the Aft Horizontal Stabilizer (AHS), and the Aft Port and Starboard Vertical Stabilizers (APVS and ASVS). The properties included in Table 5.1 are the wing type, the wing dimensions (c and s for rectangular wings, c_r, c_t, and s for the trapezoidal wings), the wing surface area, the wing aspect ratio, the wing lift-curve slope, and the distance from the center of the wing where the lift acts. The geometry shown in Figures 5-1 and 5-2 represents the largest possible aerodynamic surfaces that can be used consistent with track and tunnel clearances. In the rigid body simulation used previously [4], smaller surfaces were assumed resulting in a conservative design.

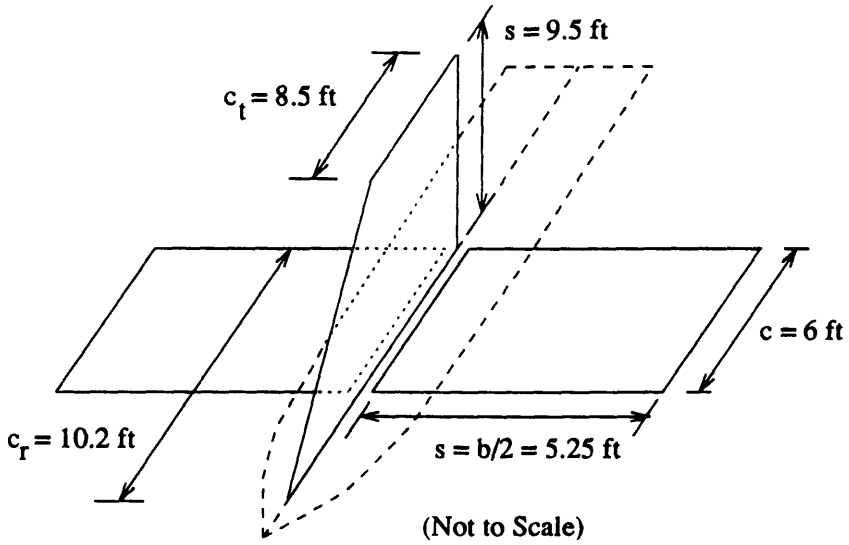

Figure 5-1: Fore Lifting Surfaces of Maglev Vehicle

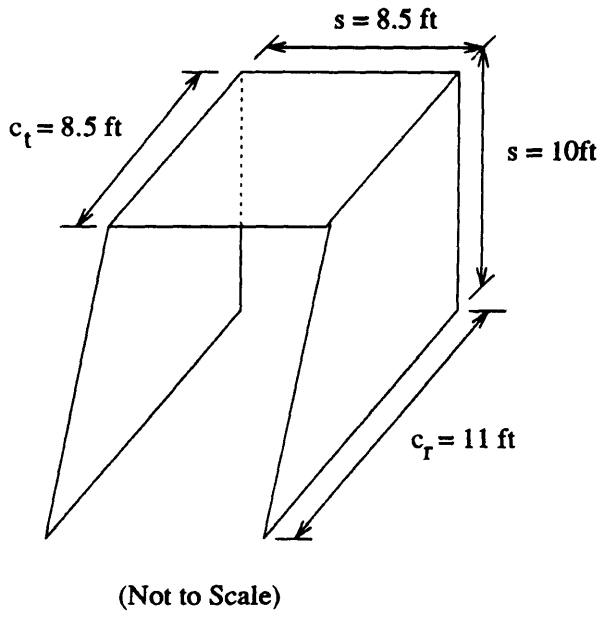

Figure 5-2: Aft Lifting Surfaces of Maglev Vehicle

n	*Wing*	*Type*	*Chord (ft)*	*Span (ft)*	$S\ (ft^2)$	AR	C_{L_α}	$\frac{y_0}{s}$
1	FVS	Trap	$c_r = 10.2\ c_t = 8.5$	9.5	88.9	2.03	2.64	.445
2	FPHS	Rect	6	5.25	31.5	1.75	2.36	.437
3	FSHS	Rect	6	5.25	31.5	1.75	2.36	.437
4	APVS	Trap	$c_r = 11\ c_t = 8.5$	10	97.5	2.05	1.48	.448
5	ASVS	Trap	$c_r = 11\ c_t = 8.5$	10	97.5	2.05	1.48	.448
6	AHS	Rect	8.5	8.5	72.25	1	2.65	0

Table 5.1: Geometric Properties of Maglev Lifting Surfaces

5.1.1 Aerodynamic Comparison

The aerodynamic quantites used in the simulation are lumped approximations of the actual aerodynamic quantities, and most of the expressions derived in Section 3.1.1 for trapezoidal wings were not utilized directly within the simulation. Therefore, it was deemed that a comparison between the aerodynamic terms produced by the control surfaces in the simulation model and the aerodynamic terms produced by the expressions derived in this thesis would be beneficial in establishing the range of possible control authority.

The control surface terms in the simulation represent the lumped aerodynamic angles required to create the particular force or moment after which the angle is named. The control surface terms are as follows: α_z represents the Z-force control angle, α_p represents the pitching moment control angle, α_y represents the Y-force control angle, α_{ya} represents the yawing moment control angle, and α_{ro} represents the rolling moment control angle. Relations between the control angle and the actual angles of attack, where the actual angles of attack of each lifting surface are given by α_n, where n is the first column of Table 5.1, can be derived by examining which lifting surfaces need to be deflected to create specific forces and moments. The relations between the actual wing angles of attack and the demanded control angles are

$$\alpha_1 = \alpha_y + \alpha_{ya}$$

$$\alpha_2 = \alpha_z + \alpha_p + \alpha_{ro}$$

$$\alpha_3 = \alpha_z + \alpha_p - \alpha_{r0}$$

$$\begin{aligned}
\alpha_4 &= \alpha_y - \alpha_{ya} \\
\alpha_5 &= \alpha_y - \alpha_{ya} \\
\alpha_6 &= \alpha_z - \alpha_p
\end{aligned}$$

where the numerical subscripts can be related to the particular surface using Table 5.1. Also note that the maximum value of the α_n is set by its surface stall behavior.

In order to compare the forces and moments produced by each surface, the inverse expressions are required in the form of

$$\begin{aligned}
\alpha_z &= \frac{\alpha_2 + \alpha_3 + 2\alpha_6}{4} \\
\alpha_p &= \frac{\alpha_2 + \alpha_3 - 2\alpha_6}{4} \\
\alpha_y &= \frac{2\alpha_1 + \alpha_4 + \alpha_5}{4} \\
\alpha_{ya} &= \frac{2\alpha_1 - \alpha_4 - \alpha_5}{4} \\
\alpha_{ro} &= \frac{\alpha_2 - \alpha_3}{2}
\end{aligned}$$

Now, one can compare the aerodynamic expressions used in the simulation with the forces and moments that would be produced by the actual lifting surfaces. The simulation aerodynamic expressions are, according to the section concerning modal control of the maglev vehicle,

$$\begin{aligned}
Z_A &= \frac{1}{2}\rho u_0^2 S_w C_{L_\alpha} \alpha_z \\
M_A &= \frac{1}{2}\rho u_0^2 S_w l_w C_{L_\alpha} \alpha_p \\
Y_A &= \frac{1}{2}\rho u_0^2 S_w C_{L_\alpha} \alpha_y \\
N_A &= \frac{1}{2}\rho u_0^2 S_w l_w C_{L_\alpha} \alpha_{ya} \\
L_A &= \frac{1}{2}\rho u_0^2 S_w l_{wr} C_{L_\alpha} \alpha_{ro}
\end{aligned}$$

and the aerodynamic expressions of the real surfaces all take the form:

$$L_n = \frac{1}{2}\rho u_n^2 S_n C_{L_{an}} \alpha_n$$
$$M_n = \frac{1}{2}\rho u_n^2 S_n l_n C_{L_{an}} \alpha_n$$

If one subsitutes the expressions for the angles of attack into the expressions for the control forces, and organizes them according to lifting surface, then a comparison can be made.

Now, numerical values for the various parameters must be provided. The numerical parameters from the simulation are $u_0 = 492.2$ ft/s, $l_w = 164.04$ ft, $l_{wr} = 3.28$ ft, $S_w = 21.53$ ft^2, $\rho = 0.0024$ slug/ft^3, and $C_{L_a} = 4$. The numerical values for the forces and moments for the actual wings require slightly more computation, depending on the surface being considered. The value of ρ is the same, as is the value of the incoming velocity $u_0 = u_n$. The angles of attack, as will be seen in Section 5.1.2, are largely unaffected by the downwash effects. The values of S and C_{L_a} can be determined from Table 5.1. The average distance from the lifting surface to the center of mass is about $l_1 = 50$ ft, and the roll distance l_2 is determined by the wing geometry (y_0/s).

The expressions that result from inserting the equations that come from comparing the angles into the simulation control equations, then reorganizing the equations to correspond to the real surfaces are as follows, where all angles of attack are considered $\alpha_n = 1^o = .017$ rad:

Force due to α_1:

From Simulation:

$$\frac{1}{2}\rho u_0^2 S_w C_{L_a} \frac{\alpha_1}{2}$$

From Thesis:

$$\frac{1}{2}\rho u_0^2 S_1 C_{L_{a1}} \alpha_1$$

Moment due to α_1:

From Simulation:

$$\frac{1}{2}\rho u_0^2 S_w l_w C_{L_a} \frac{\alpha_1}{2}$$

From Thesis:

$$\frac{1}{2}\rho u_0^2 \mathcal{S}_1 l_1 C_{L_{\alpha 1}} \alpha_1$$

Force due to α_2:

From Simulation:

$$\frac{1}{2}\rho u_0^2 \mathcal{S}_w C_{L_\alpha} \frac{\alpha_2}{4}$$

From Thesis:

$$\frac{1}{2}\rho u_0^2 \mathcal{S}_2 C_{L_{\alpha 2}} \alpha_2$$

Moment due to α_2:

From Simulation:

$$\frac{1}{2}\rho u_0^2 \mathcal{S}_w l_w C_{L_\alpha} \frac{\alpha_2}{4} + \frac{1}{2}\rho u_0^2 \mathcal{S}_w l_{wr} C_{L_\alpha} \frac{\alpha_2}{2}$$

From Thesis:

$$\frac{1}{4}\rho u_0^2 \mathcal{S}_2 l_1 C_{L_{\alpha 2}} \alpha_2 + \frac{1}{4}\rho u_0^2 \mathcal{S}_2 l_2 C_{L_{\alpha 2}} \alpha_2$$

Force due to α_3:

From Simulation:

$$\frac{1}{2}\rho u_0^2 \mathcal{S}_w C_{L_\alpha} \frac{\alpha_3}{4}$$

From Thesis:

$$\frac{1}{2}\rho u_0^2 \mathcal{S}_3 C_{L_{\alpha 3}} \alpha_3$$

Moment due to α_3:

From Simulation:

$$\frac{1}{2}\rho u_0^2 \mathcal{S}_w l_w C_{L_\alpha} \frac{\alpha_3}{4} - \frac{1}{2}\rho u_0^2 \mathcal{S}_w l_{wr} C_{L_\alpha} \frac{\alpha_3}{2}$$

From Thesis:

$$\frac{1}{4}\rho u_0^2 \mathcal{S}_3 l_1 C_{L_{\alpha 3}} \alpha_3 - \frac{1}{4}\rho u_0^2 \mathcal{S}_3 l_2 C_{L_{\alpha 3}} \alpha_3$$

Force due to α_4 or α_5:

From Simulation:

$$\frac{1}{2}\rho u_0^2 S_w C_{L_\alpha} \frac{\alpha_4}{4}$$

From Thesis:

$$\frac{1}{2}\rho u_0^2 S_4 C_{L_{\alpha 4}} \alpha_4$$

Moment due to α_4 or α_5:

From Simulation:

$$-\frac{1}{2}\rho u_0^2 S_w l_w C_{L_\alpha} \frac{\alpha_4}{4}$$

From Thesis:

$$\frac{1}{2}\rho u_0^2 S_4 l_1 C_{L_{\alpha 4}} \alpha_4$$

Force due to α_6:

From Simulation:

$$\frac{1}{2}\rho u_0^2 S_w C_{L_\alpha} \frac{\alpha_6}{2}$$

From Thesis:

$$\frac{1}{2}\rho u_0^2 S_6 C_{L_{\alpha 6}} \alpha_6$$

Moment due to α_6:

From Simulation:

$$-\frac{1}{2}\rho u_0^2 S_w l_w C_{L_\alpha} \frac{\alpha_6}{2}$$

From Thesis:

$$\frac{1}{2}\rho u_0^2 S_6 l_1 C_{L_{\alpha 6}} \alpha_6$$

Please note that half of the moment generated by the FPHS and FSHS is considered to be roll generated, while the other half of the moment comes from other moment considerations.

The numerical results of this comparison are presented in Table (5.2). To a great extent, the differences arise mostly due to the fact that the simulation assumed surfaces areas much smaller than the apparent maximum available ones, and overestimate

Angle		*Simulation*	*Thesis*
α_1	Force (lb)	212	1158
	Moment (lb-ft)	34908	58000
α_2	Force (lb)	106.4	367.5
	Moment (lb-ft)	18152.3	9265
α_3	Force (lb)	106.4	367.5
	Moment (lb-ft)	16756	9104
α_4	Force (lb)	109.4	713.1
	Moment (lb-ft)	-17454	35655
α_6	Force (lb)	106.4	529.64
	Moment (lb-ft)	-34908	47310

Table 5.2: Results of Aerodynamic Comparison

the moment arm. However, as the calculated aerodynamic parameters represent the maximum allowable lifting surface area possible within track constraints, it was concluded that the aerodynamic characteristics already present within the simulation are conservative estimates and therefore are suitable for carrying out the modal control effectiveness assessment.

5.1.2 Downwash Considerations

Examination of the maglev configuration provided at the beginnning of this chapter shows that the FVS is directly in front of the rear box wing. Therefore, since the FVS has about the same span as the box wing, there exists the possibility that the incoming flow to the box wing structure will be affected by the vortex shed by the FVS. The purpose of this analysis and subsequent numerical computation is to discover where the vortex moves as it extends along the body of the maglev vehicle, what effect the shed vortex has on the box wing aerodynamics, and whether or not this effect is of a small enough magnitude that it can be ignored.

The strength Γ_0 of the vortex shed by the FVS is obtained from considering the Kutta-Joukowski Theorem [8] for the FVS:

$$\frac{1}{2}\rho V_\infty^2 S \frac{dC_L}{d\alpha}\alpha = s\rho V_\infty \Gamma_0$$

for a constant strength vortex.

Eliminating terms and solving for Γ_0 if $\mathcal{S} = s(c_r + c_t)/2$ gives:

$$\Gamma_0 = \frac{V_\infty}{4}(c_r + c_t)\frac{dC_L}{d\alpha}\alpha \tag{5.1}$$

This expression is the strength of the vortex shed by the FVS. The maximum vehicle speed of 492 ft/s results in the strongest circulation that will be experienced. Using c_r, c_t and $dC_L/d\alpha$ as per the FVS geometry presented in the previous section, and a value of $\alpha = 3^o$ (= .052 rad) gives a circulation of $\Gamma_0 = 318$ ft^2/s.

The location of the shed vortex as it extends down the length of the body, subject to the body effect, is governed by the differential equations for the vortex motion derived in the part of Section 3.1.1 concerning "Half Wing-Body Interactions" in the Analysis Chapter. These equations were integrated using a FORTRAN program [24] presented in Appendix B to determine the position of the vortex when it reached the box wing. The location of the vortex was evaluated for initial conditions $\theta = 0$, $x = 0$, $a_0 = \pi s/4 = 7.46$ ft ([13] and Section 3.2.2), with the FVS located at $x = 0$, and a downstream distance of $x = 102$ ft. Other parameters included the number of steps $n = 200$, and the radius of the body $R = 5$ ft. The program output is non-dimensionalized with respect to the body radius, so the results of the program give the vortex as moving to $\bar{a} = 1.92$ (no radial motion), and $\theta = .15291$ rad. The location of the vortex with respect to the rear wings is portrayed graphically in Figure 5-3.

Now that the position of the vortex with respect to the aft box wing is known, it is possible to calculate the effect that the vortex has on the lifting characteristics of the box wing. The following quantities are defined as in Figure 5-4: $l_z = 10$ ft, which is the distance from the center of the body to the AHS, which is the same as the span of the APVS and ASVS, $l_y = 4.25$ ft, the distance from the vehicle center to the APVS and ASVS, which is also the semi-span of the AHS, $a_0 = 7.46$ ft, which is defined above as the location of the vortex along the z-axis when $x = 0$, $y_0 = 1.1365$ ft, the distance the vortex moves in the y-direction as it proceeds down the body, and

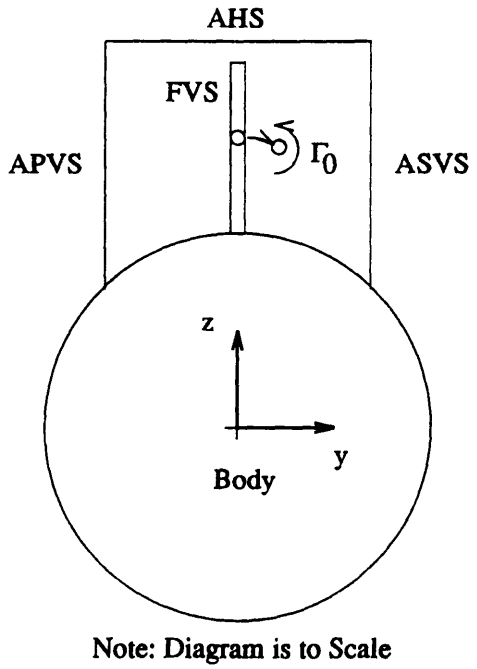

Figure 5-3: Path of Vortex in Y-Z Plane

$z_0 = .0875$ ft, the distance the vortex moves in the z-direction.

The vortex effect is characterized by a change in the local or section angle of attack of the incoming flow. This is due to the fact that the vortex induces a velocity on the surface of each wing that, when superimposed on the incoming flow, changes the flow direction and therefore the angle of attack. This manifests itself in an additional rolling moment that is exerted on the box wings. It is the aim of this numerical analysis to calculate this moment and determine if it must be taken into account in the simulation and subsequent modal control design. Each section of the box wing is considered separately, ignoring edge interactions. The velocities induced on each wing will be calculated, followed by the moments.

The first section of the box wing to be considered is the AHS. As can be seen in Figure 5-5, only the normal component of the induced velocity will have an effect on the flow over the AHS, with the sidewash effect being neglected. Using the expression

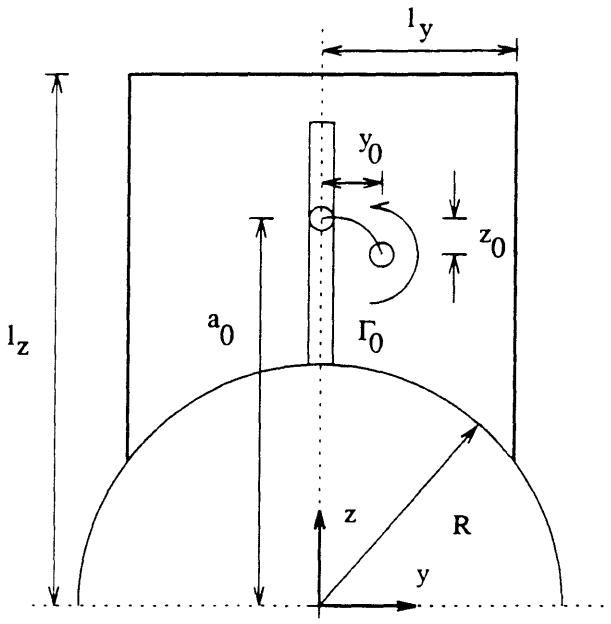

Figure 5-4: Downwash Effect Geometry Definitions

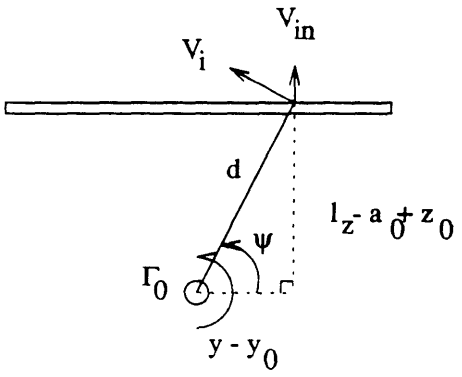

Figure 5-5: Induced Velocity on AHS

for the induced velocity derived in the Analysis Chapter, the induced velocity is:

$$\begin{aligned} V_{in} &= V_i \cos\psi \\ &= \frac{\Gamma_0}{4\pi d}\left(1 + \frac{x_0}{\sqrt{x_0^2 + d^2}}\right)\cos\psi \end{aligned}$$

where ψ is the angle between the y-axis the point that d is considered to be acting at, and d is the distance between the vortex and wing. It is helpful to derive the expression for d in terms of rectangular coordinates y and z, then convert them into a function of ψ alone. From Figure 5-5, it can be seen that

$$d = \frac{l_z - a_0 + z_0}{\sin\phi}$$

and

$$\tan\psi = \frac{l_z - a_0 + z_0}{y - y_0}$$

so, the resulting expression for the induced velocity is

$$V_{in} = \frac{\Gamma_0}{4\pi(l_z - a_0 + z_0)}\left(1 + \frac{x_0}{\sqrt{x_0^2 + [l_z - a_0 + z_0]^2 / \sin^2\psi}}\right)\sin\psi\cos\psi \qquad (5.2)$$

where the bounds on the angle ψ are

$$\begin{aligned} y = l_y \quad ; \quad \psi = 40.16^o \\ y = -l_y \quad ; \quad \psi = 154^o \end{aligned}$$

For the ASVS wing, the section angle of attack will only be affected by the tangential component of the induced velocity. This induced velocity is

$$V_{it1} = -V_i \sin\psi$$

where V_i is as above. The distance d from the vortex to the wing as a function of the

vertical coordinate, z, is

$$d^2 = (l_y - y_0)^2 + (z - a_0 + z_0)^2$$

Using the same procedure as for the AHS, and expression for d in terms of ψ can be obtained:

$$d = \frac{l_y - y_0}{\cos\psi}$$

and, the induced velocity is

$$V_{it1} = \frac{-\Gamma_0}{4\pi(l_y - y_0)} \left(1 + \frac{x_0}{\sqrt{x_0^2 + [l_y - y_0]^2 / \cos^2\psi}} \right) \sin\psi \cos\psi \qquad (5.3)$$

where the bounds on ψ are

$$z = l_z \quad ; \quad \psi = 40.16^o$$
$$z = 0 \quad ; \quad \psi = -67.105^o$$

The final wing section is the APVS. This lifting surface is also only affected by the tangential component of the induced velocity, so

$$\begin{aligned} V_{it2} &= V_i \sin(\pi - \psi) \\ &= V_i \sin\psi \end{aligned}$$

The expression for d is

$$d^2 = (l_y + y_0)^2 + (z - a_0 + z_0)^2$$

but, it is important to remember that

$$\tan(\pi - \psi) = -\tan\psi = \frac{z - a_0 + z_0}{l_y + y_0}$$

so, the expression for d in terms of ψ is

$$d = \frac{l_y + y_0}{\cos\psi}$$

and, the induced velocity is

$$V_{it2} = \frac{\Gamma_0}{4\pi(l_y + y_0)} \left(1 + \frac{x_0}{\sqrt{x_0^2 + [l_y + y_0]^2 \, cos^2\psi}}\right) \sin\psi \cos\psi \tag{5.4}$$

with the bounds on ψ being

$$z = l_z \quad ; \quad \psi = 154^o$$

$$z = 0 \quad ; \quad \psi = 233.85^o$$

In order to calculate the moment induced by this vortex on each surface, it is necessary to calculate the angle of attack resulting from the free stream velocity and the induced velocity. This is accomplised by using the approximation

$$\epsilon = \frac{V_i}{V_\infty} \tag{5.5}$$

This induced angle of attack ϵ is plotted for each wing section of the box wing in Figures 5-6, 5-7, and 5-8.

Now that the modified angle of attack $\alpha_T = \alpha + \epsilon$ is known for each wing, the moments may be calculated as follows: the flow over each surface generates a lift, but that lift is now non-symmetric due to the effect of the downwash vortex. As can be seen in Figure 5-9, instead of acting uniformly upon the wing, the expressions for lift and moment over a differential element dy (or dz for the vertical wings) are given as

$$dL = \frac{1}{2}\rho V_\infty^2 c(y) \frac{dC_L}{d\alpha}(\alpha_T) dy \tag{5.6}$$

$$dM = \frac{1}{2}\rho V_\infty^2 y c(y) \frac{dC_L}{d\alpha}(\alpha_T) dy \tag{5.7}$$

These expressions can be evaluated and integrated for the conditions given for each

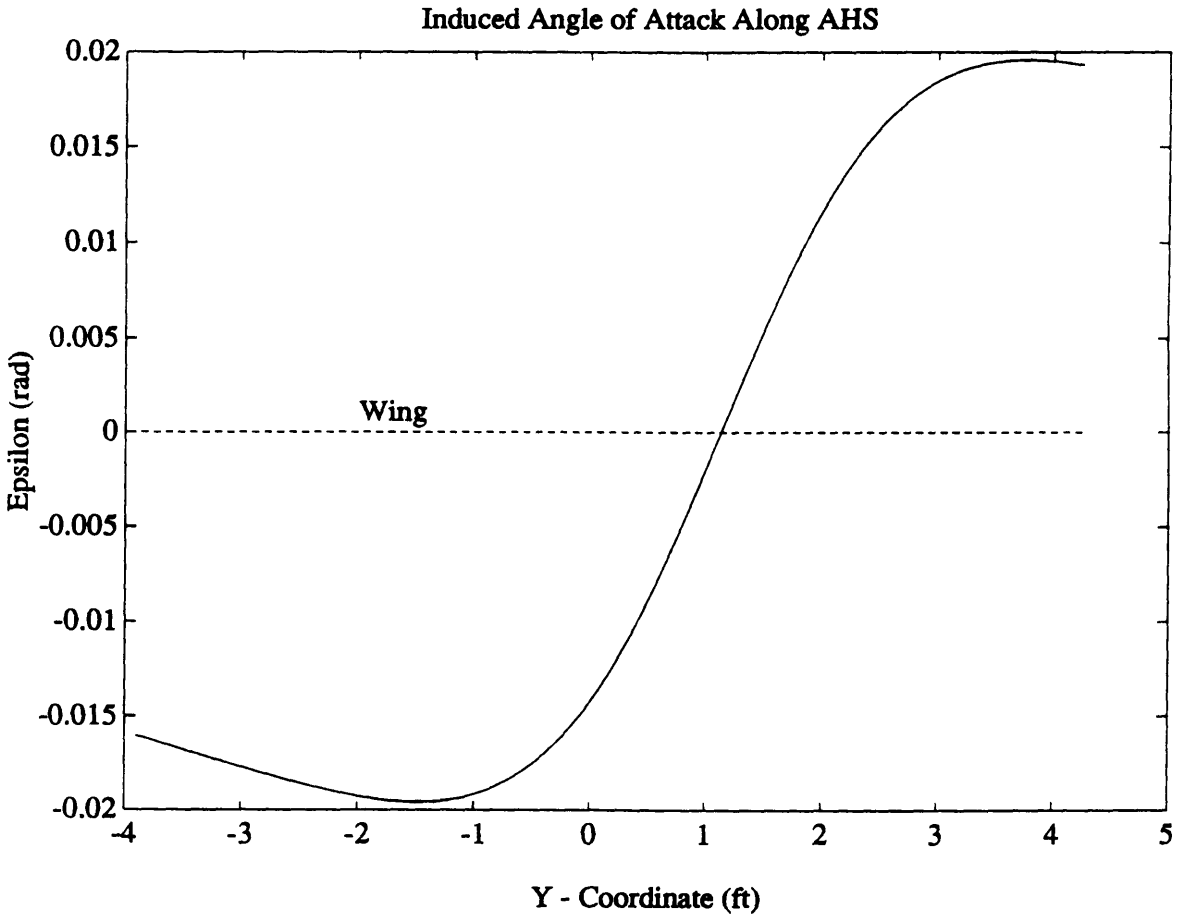

Figure 5-6: Induced Angle of Attack Along AHS

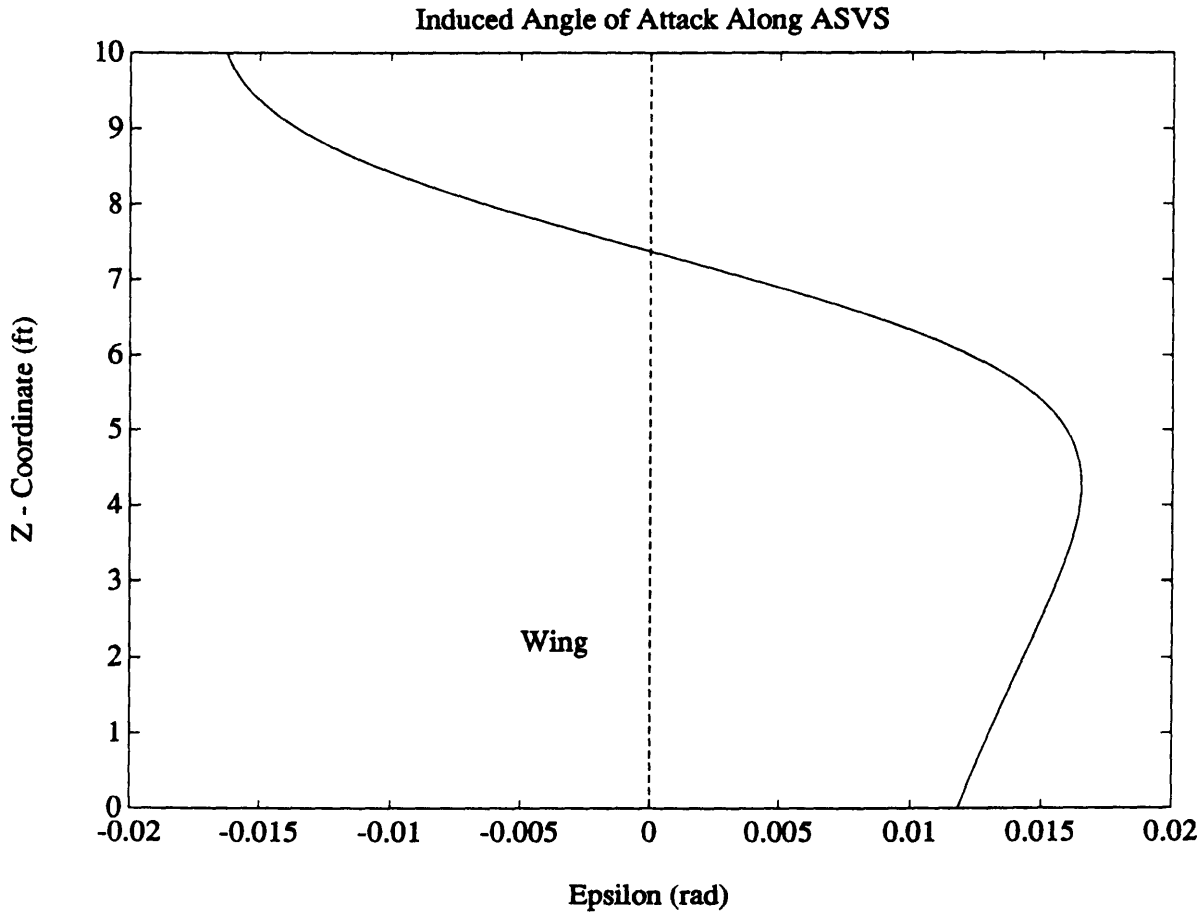

Figure 5-7: Induced Angle of Attack Along ASVS

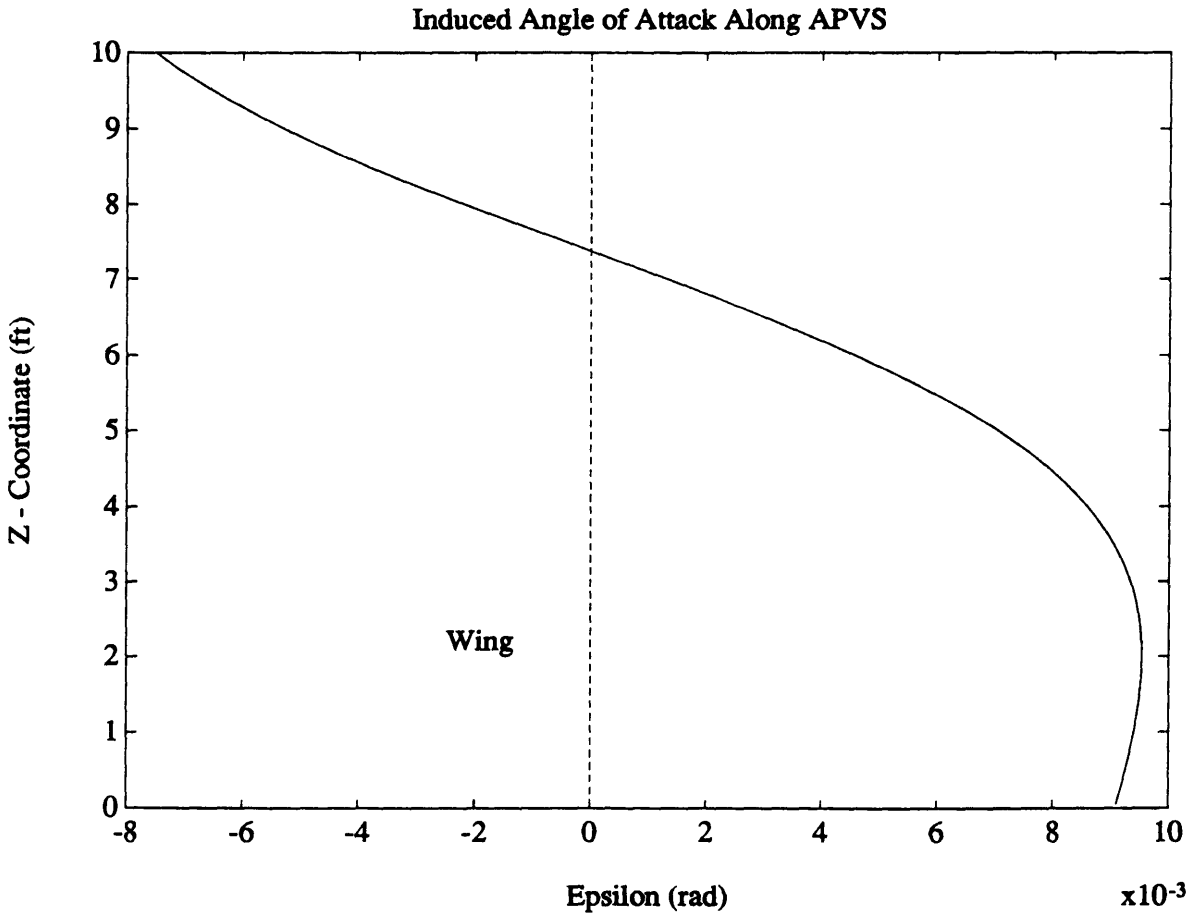

Figure 5-8: Induced Angle of Attack Along APVS

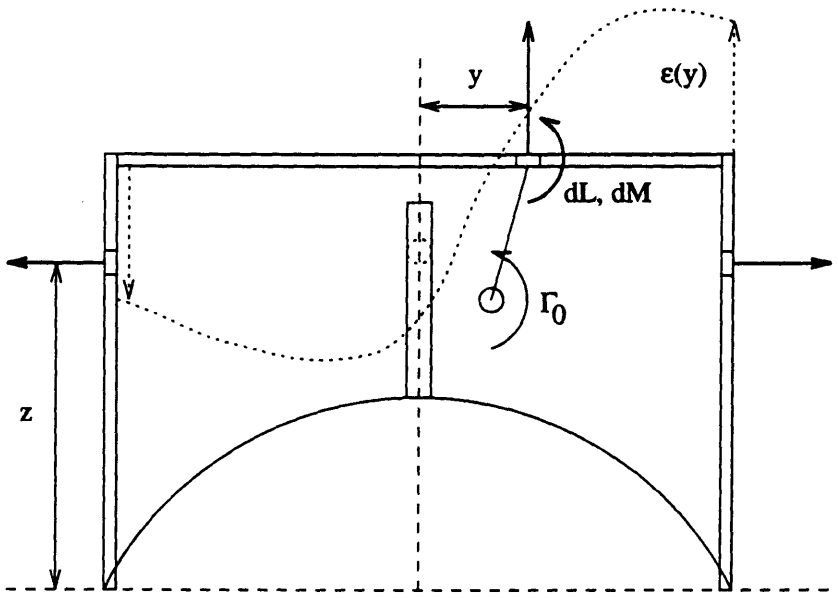

Figure 5-9: Forces and Moments Due to Induced Angle of Attack

wing.

For the AHS, the chord c is constant because the wing is rectangular, and the induced angle of attack ϵ is a function of y. As the integration will be performed over y, one must convert the expression for ϵ back into a function of y by using:

$$\sin\psi = \frac{l_z - a_0 + z_0}{\sqrt{(y-y_0)^2 + (l_z - a_0 + z_0)^2}}$$
$$\cos\psi = \frac{y - y_0}{\sqrt{(y-y_0)^2 + (l_z - a_0 + z_0)^2}}$$

and the resulting expression for $\epsilon(y)$ is

$$\epsilon(y) = \frac{\Gamma_0}{4\pi V_\infty}\left[1 + \frac{x_0}{\sqrt{x_0^2 + (y-y_0)^2 + (l_z - a_0 + z_0)^2}}\right]\frac{y - y_0}{(y-y_0)^2 + (l_z - a_0 + z_0)^2}$$

The equation for M can then be obtained by inserting the expression for ϵ into the

expression for dM to get

$$\begin{aligned} M &= \int_{-l_y}^{l_y} \frac{1}{2}\rho V_\infty^2 c y \frac{dC_L}{d\alpha}(\alpha + \epsilon(y))dy \\ &= \frac{1}{2}\rho V_\infty^2 c \frac{dC_L}{d\alpha}\left[\alpha \int_{-l_y}^{l_y} y dy + \int_{-l_y}^{l_y} y\epsilon(y)dy\right] \\ &= \frac{1}{2}\rho V_\infty^2 c \frac{dC_L}{d\alpha}\int_{-l_y}^{l_y} y\epsilon(y)dy \end{aligned} \tag{5.8}$$

This equation may be numerically integrated to give a value for the moment. The value of the integral is .4328, and the moment produced by the downwash is $M =$ 1575 lb-ft using the values for free-stream and geometric properties presented in the previous section.

For the ASVS, the situation changes slightly. The wing is trapezoidal, so the chord is now a function of z, $c(z) = c_r[1 + (\lambda - 1)z/l_z]$. Also, the angle of attack of the vehicle contributes to the sidewash on the wing, so it can be ignored, and the angle of attack on the wing is solely determined by the induced angle of attack ϵ. The expression for ϵ, obtained using the same methods as above, is

$$\epsilon(z) = -\frac{\Gamma_0}{4\pi V_\infty}\left[1 + \frac{x_0}{\sqrt{x_0^2 + (l_y - y_0)^2 + (z - a_0 + z_0)^2}}\right]\frac{z - a_0 + z_0}{(l_y - y_0)^2 + (z - a_0 + z_0)^2}$$

and, the resulting equation for the moment M as a function of z is

$$M(z) = \frac{1}{2}\rho V_\infty^2 \frac{dC_L}{d\alpha}\int_0^{l_z} z c(z)\epsilon(z)dz \tag{5.9}$$

This may also be integrated numerically, with the value of the integral being 1.0957 and the moment is $M = 839$ lb-ft.

The situation concerning the APVS is much the same as that of the ASVS, except that the induced angle of attack has a slightly different expression

$$\epsilon(z) = -\frac{\Gamma_0}{4\pi V_\infty}\left[1 + \frac{x_0}{\sqrt{x_0^2 + (l_y + y_0)^2 + (z - a_0 + z_0)^2}}\right]\frac{z - a_0 + z_0}{(l_y + y_0)^2 + (z - a_0 + z_0)^2}$$

but the expression for the moment is the same as that of the ASVS. The integral has

a value of 1.371, and the moment induced is $M = 1051$ lb-ft.

Comparison of the results gained from this section with the results of the previous section shows that the moments resulting from the downwash vortex are small when compared to those created by the lifting surfaces. Therefore, the assumption that the simulation makes in ignoring the downwash effect on the rear box wing system is justified.

5.1.3 Modal Control Results

The first set of results that are discussed are those that attempt to establish the validity of the modified maglev simulation when compared to the original simulation. As has been stated before, the original six degree-of-freedom non-linear simulation of the maglev dynamic has been thoroughly tested and has been determined to be an adequate model of the dynamic behavior of the vehicle. Therefore, if one was able to prove that the modified seven degree-of-freedom model reduced to the original model if the extra degree of freedom was somehow removed, then the modified model could be accepted as an adequate approximation to the vehicle dynamics.

The method used to check and see if the seven degree-of-freedom model reduced to the six degree-of-freedom model was to increase the stiffness of the torsional spring represented in the modified simulation, and observe whether or not the behavior approached that of the simulation profile without a flexible mode. The disturbance input used to make the comparison was a 2 cm step response applied to the vertical track disturbance input, which serves to excite all the longitudinal states z, θ, and δ.

The result of this comparison can be seen in Figures 5-10, 5-11, and 5-12. In Figure 5-10, it can be seen that as the torsional spring becomes stiffer, i.e. its natural bending frequency f increases, the z-response for the modified simulation approaches that of the original one. The different trim states are the result of the fact that because a degree of flexibility has been introduced into the system, and the simulation is composed of a non-linear controller operating upon a linear system, the regulation process due to the LQR controller is not complete, so the center of gravity of the vehicle (where the z-state is measured) sags according to the stiffness of the torsional

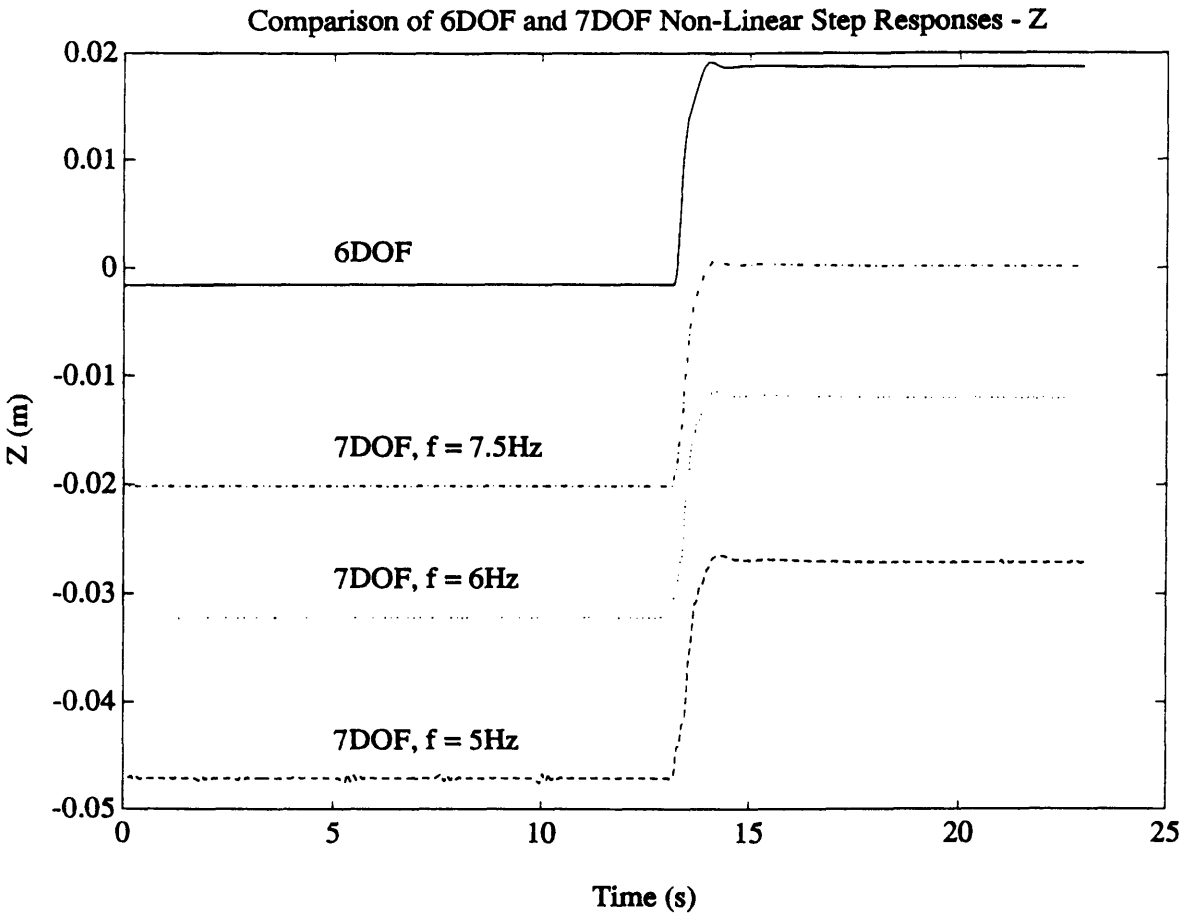

Figure 5-10: Comparison of 6DOF and 7DOF Non-Linear Step Responses - Z

spring.

In Figure 5-11, the θ response in the modified simulation can also be seen to approach the original simulation if the natural frequency is increased. Note that this state also exhibits the same type of steady-state error characteristics as the z-state due to the sagging vehicle center.

In the case of the third longitudinal variable, δ, the original simulation does not take the flexibility into account at all, so the value of δ should be zero. As might be expected, increasing the strength of the torsional spring as in Figure 5-12 reduces the value of the trim delflection, implying an upper bound of zero. From these three Figures, it is concluded that the seven degree-of-freedom simulation is valid with respect to taking the original simulation and adding an extra mode while keeping the other dynamics unchanged.

The next set of results were obtained from the modified simulation using the

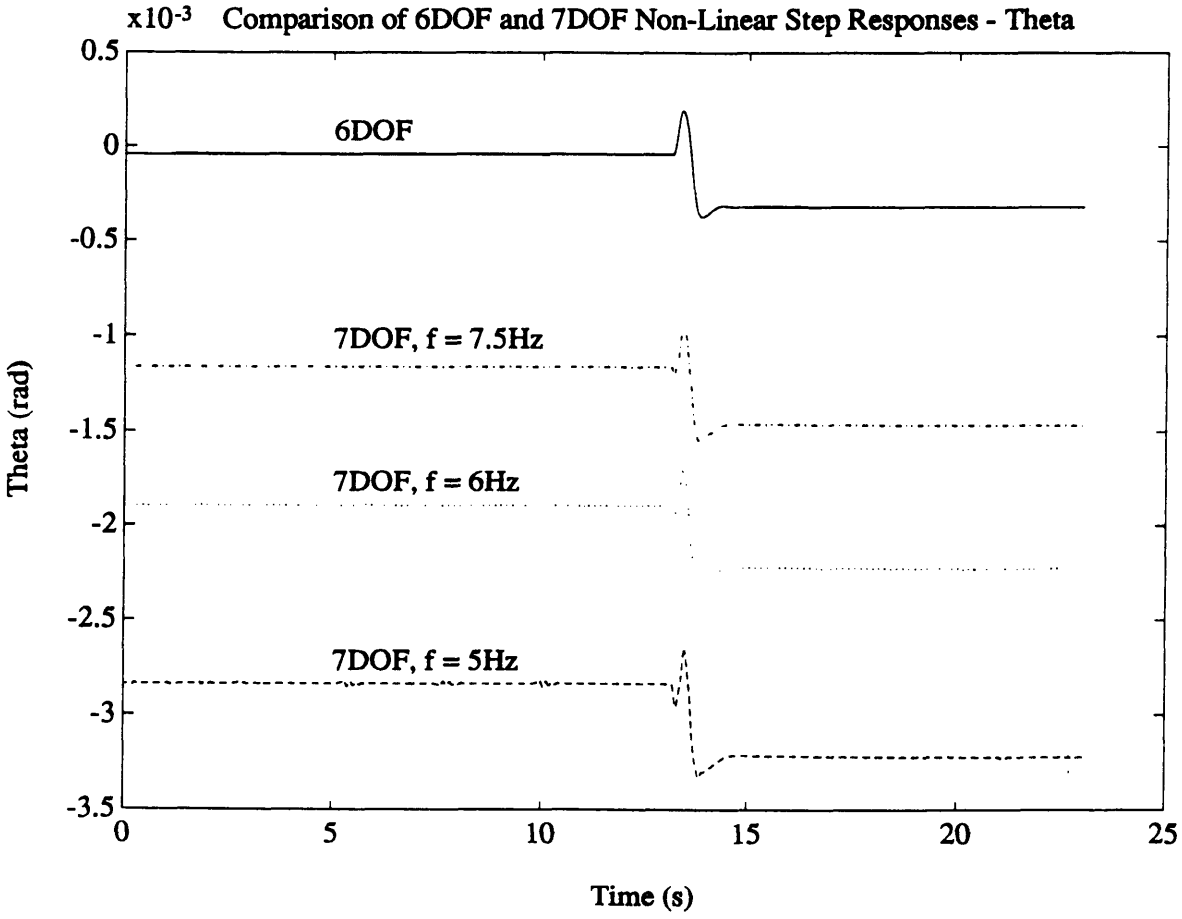

Figure 5-11: Comparison of 6DOF and 7DOF Non-Linear Step Responses - Theta

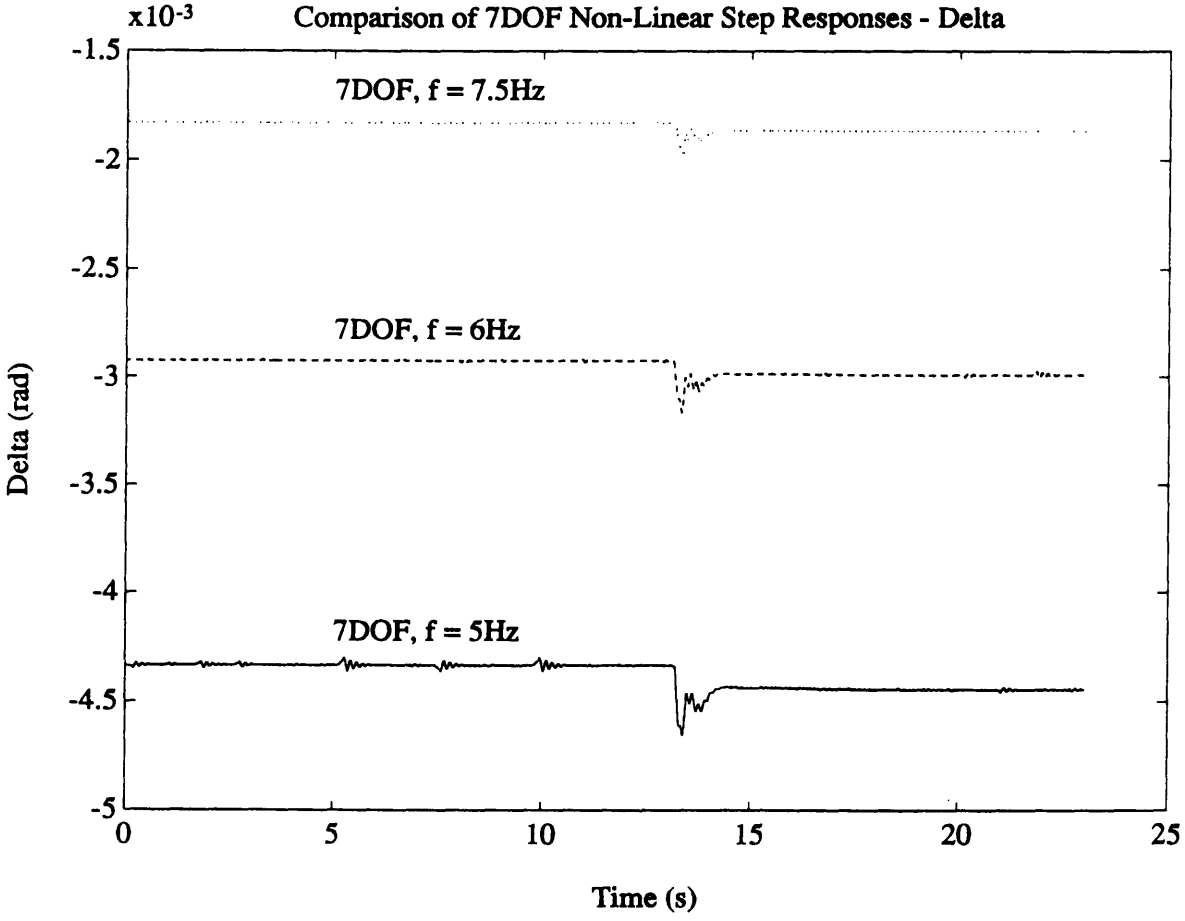

Figure 5-12: Comparison of 7DOF Non-Linear Step Responses - Delta

linearized model of the flexible maglev vehicle. All of these results take the form of Bode plots of the transfer functions from the vertical disturbance to the longitudinal variable in question. The z variable will be of greatest interest, because it is a measure of the ride quality. The value of the torsional spring constant, i.e. the natural bending frequency, was varied parametrically to study the effect of the control design. General assumptions made for all of the control system designs presented are that the system has full state feedback including the flexible mode, and that the only input is in the form of the vertical track disturbance, i.e. all of the responses are closed-loop responses to external disturbances and no tracking is attempted.

The first case studied is that of the model that possesses the flexible mode, senses it, and incorporates it into the feedback, but does not possess an actuator and surface to control it directly. The results of this study for the z-state can be seen in Figure 5-13. The conclusions that one can draw from this Figure are that there is one lightly damped mode present resulting from the flexibility, and the frequency of this mode is decreased if the frequency of the torsional spring is decreased. Also the change in the spring stiffness has a large effect on the low frequency respose, particularly when the bending frequency becomes comparable with the rigid body freqencies. Therefore, the effect of flexibilty is greatest when the bending freqency of the rigid body modes are close, a fact which must be kept in mind when examining the Bode plots of the functions that contain modal control.

The second case examined concerns the effect of weighting the deflection states in quadratic cost functional used to determine the optimal controller. The results shown here in Figure 5-14 are for the z-state with a bending frequency of 1.5 Hz. These results are shown because this is where the largest effect is present; for all of the cases, there was only a small effect on the flexible mode. The conclusion that may be draw from this is that the inclusion of δ and ν in the cost functional $J(\mathbf{x}, \mathbf{u})$ does not have a large effect, so the responses are not sensitive to the δ and ν cost function terms.

The next and most important comparison is that concerning the effects of adding modal control to the system. This control takes the form of the additional control

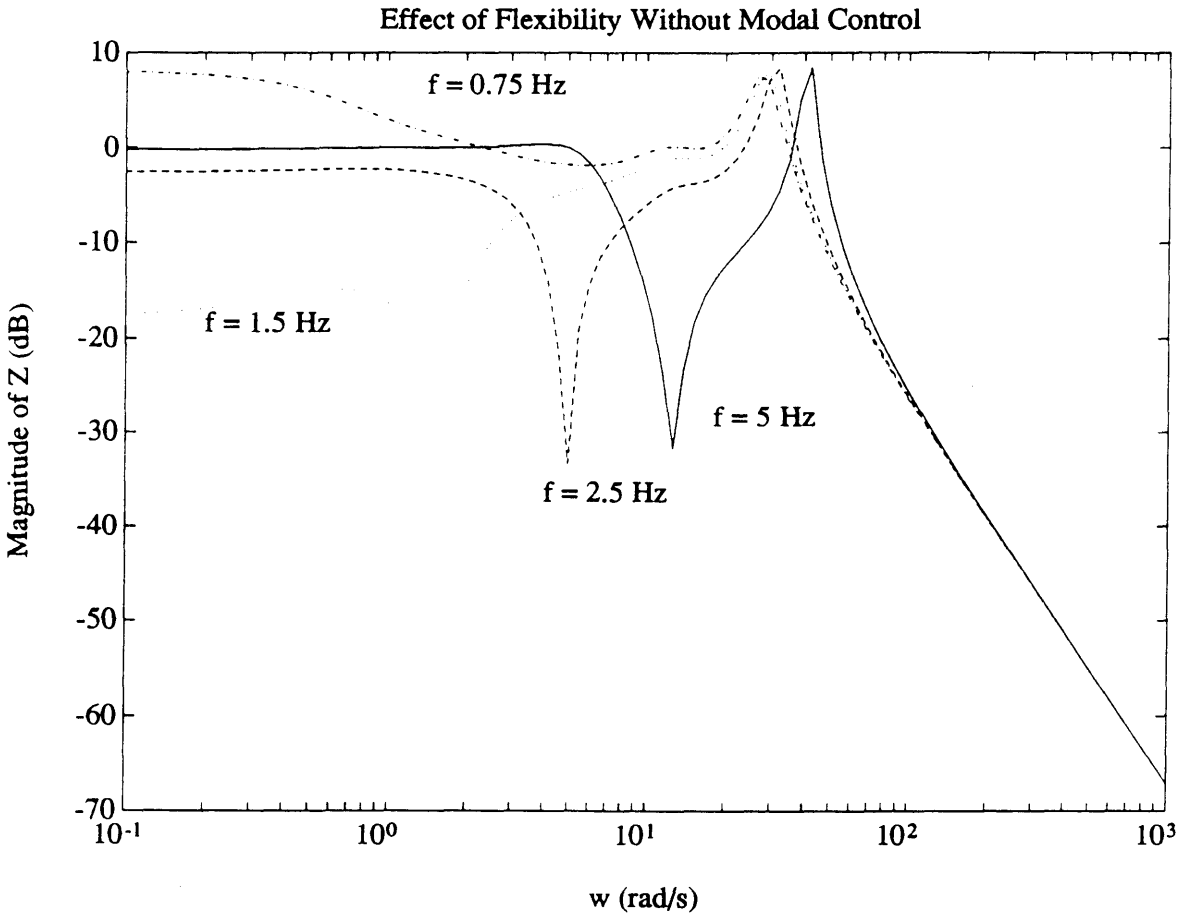

Figure 5-13: Effect of Flexibility Without Modal Control

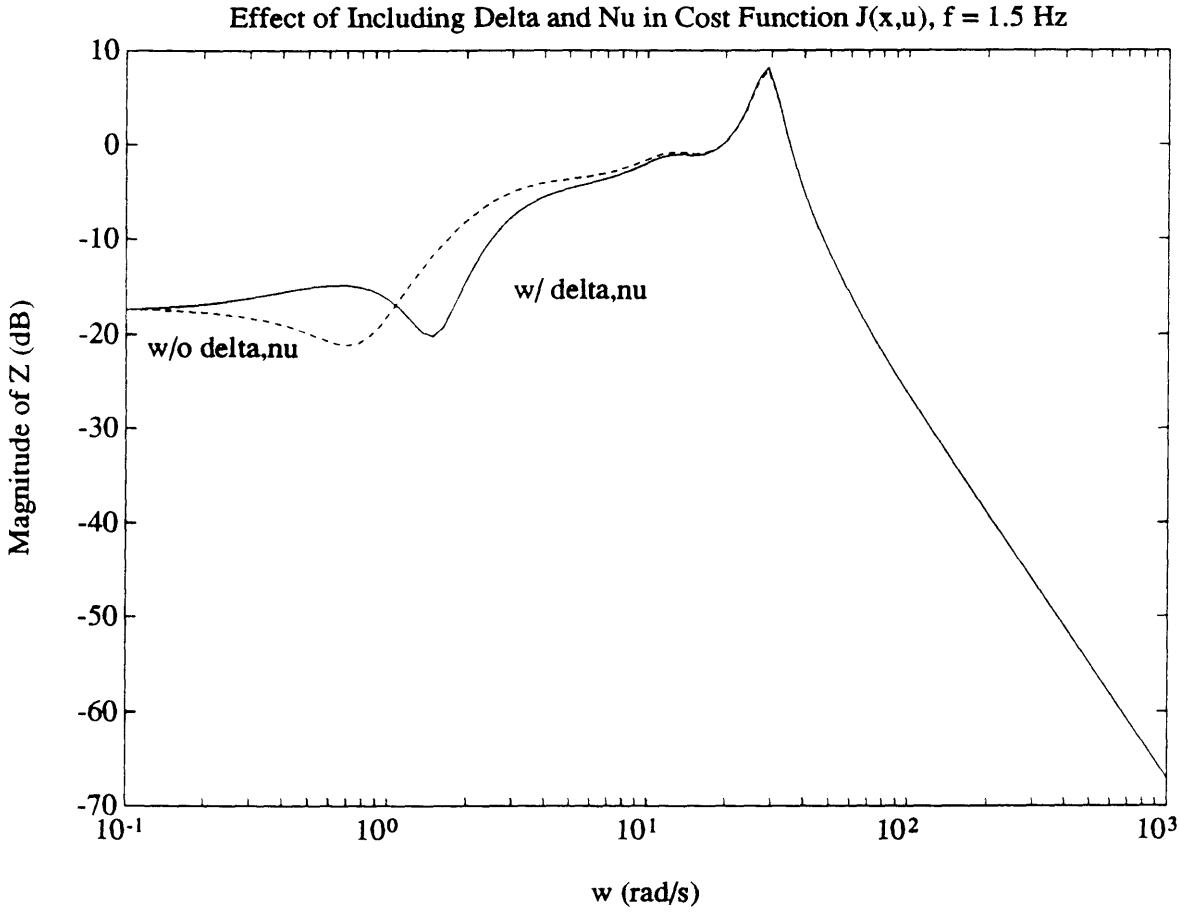

Figure 5-14: Effect of Including Delta and Nu in Cost Function

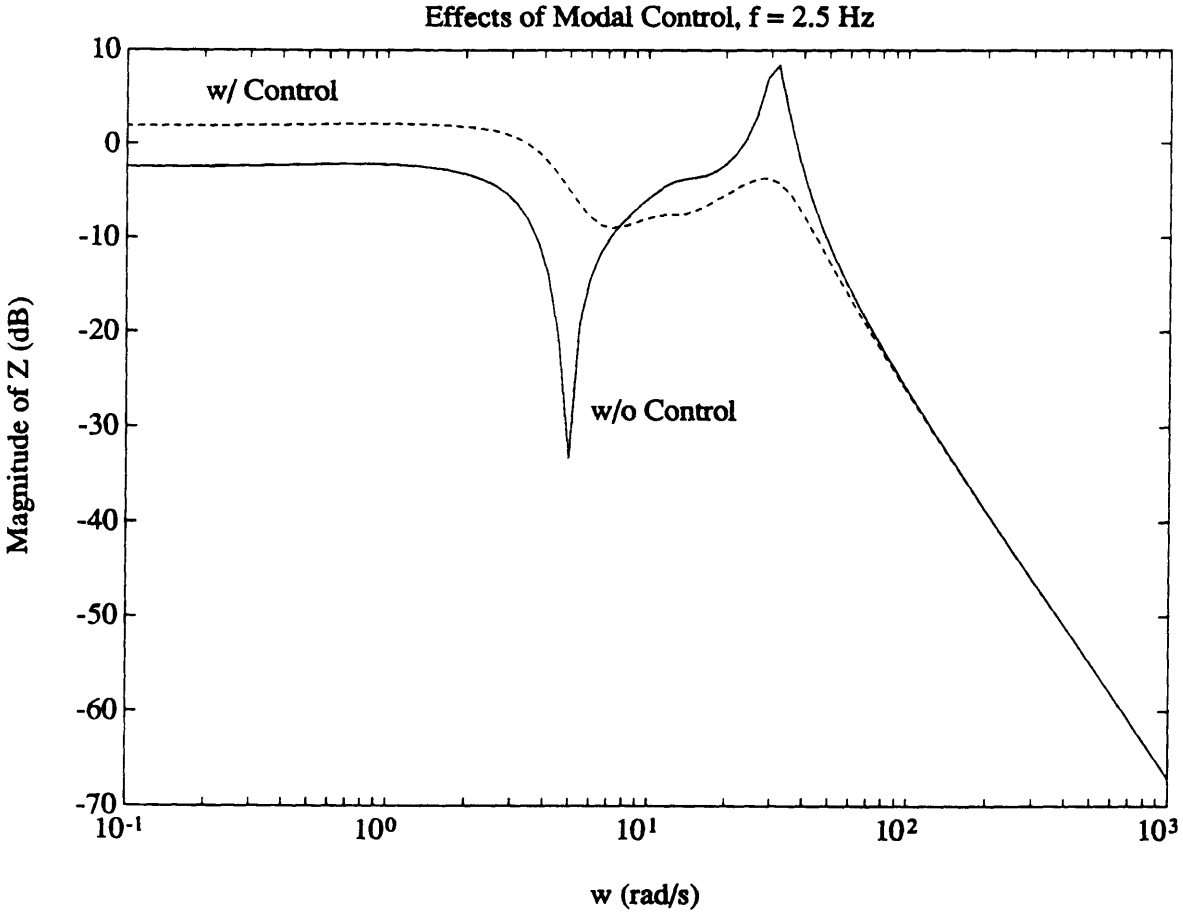

Figure 5-15: Effects of Modal Control, f = 2.5 Hz

deflection α_b. The effects, seen in Figures 5-15 and 5-16 are immediate. In both plots, the addition of modal control is effective in reducing the resonant response. However, there is apparently a mixed effect at low frequencies, with a better response evident in Figure 5-16 at 0.75 Hz as opposed to Figure 5-15 at 2.5 Hz, implying that the modal control is felt to a greater degree when the torsional spring is more flexible. A summary of the Bode plots of the transfer functions including modal control is given in Figure 5-17, where the effects of flexibility with modal control are displayed.

For ride quality improvement, reduction of the resonant mode response is required, and this has been achieved using the modal control. However, the low frequency response is important from a motion sicknes viewpoint. The cost function used in the LQR design could be modified to reflect this requirement, but that has not been implemented here.

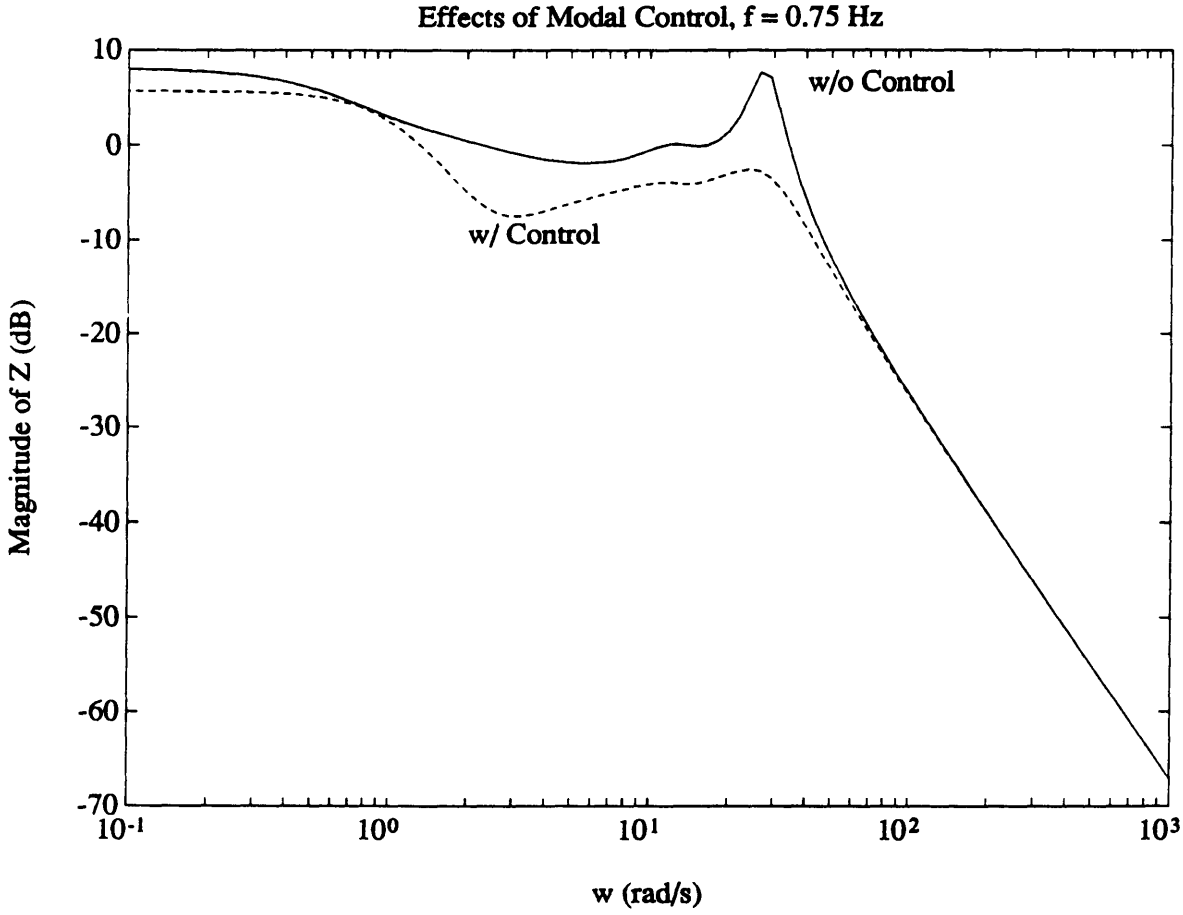

Figure 5-16: Effects of Modal Control, f = 0.75 Hz

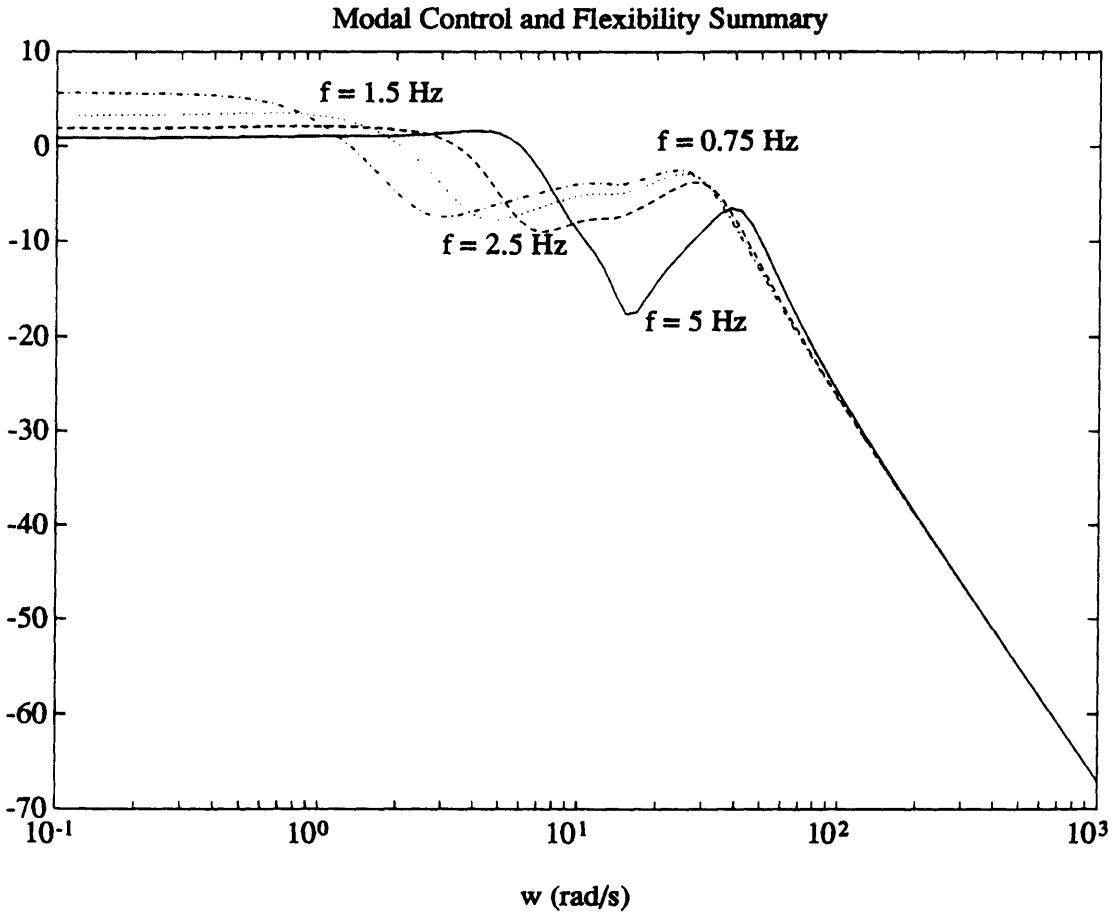

Figure 5-17: Modal Control and Flexibility Summary

5.2 Towed Vehicle

5.2.1 Vehicle Parameters

In order to design a control system for the towed aerodynamic vehicle, it was necessary to formulate the matrices derived in Section 3.3.1.

As displayed in the Examples Chapter, the towed vehicle configuration consists of two annular wings mounted on the fore and aft sections of the vehicle. The fore annular wing, the smaller of the two, has a radius $R_F = 0.32$ m, a chord of $c_F = 0.25$ m, a reference area of $S_F = 2R_F c_F = 0.16$ m^2, and an aspect ratio of $A_F = 2R_F/c_F = 2.6$. The distance from the center of the fore annular wing to the center of gravity of the towed body is $l_F = 0.76$ m. The larger aft annular wing has a radius of $R = 0.52$m, a chord $c = 0.40$ m, a surface area of $S = 0.42$ m^2, and an aspect ratio of $A = 2R/c = 2.6$. The distance form the center of gravity of the vehicle to the center of the aft wing is $l = 0.76$ m.

Other important quantities that require numerical definition are the aft body center of gravity location $c_3 = 0.51$ m, the total body mass $m = 50$ kg, the aft body mass $m_A = 25$ kg, the total body pitch inertia $B = 3.2$ kg m^2, and the aft body inertia about the center of gravity $B_A = B_1 = 1.6$ kg m^2. The flight conditions that will be assumed are an air density of $\rho = 1$ kg/m^3, a true airspeed of $u_0 = 100$ m/s, and a net lift of $L_v = 1470$ N. Using these quantites, one can obtain numerical values for other aerodynamic quanitites presented in the Analysis Chapter, Section 3.3.1, notably $C_{L_v} = .70$, $\left(\frac{\partial C_L}{\partial \alpha}\right)_v = 8.5$, $C_{D_0} = 0.02$, $C_{D_v} = 0.080$, and therefore $D_v = \frac{1}{2}\rho U_0^2 S C_{D_v} = 168$ N.

With all of these numerical values defined, values for the stability derivatives can be evaluated:

$$\begin{aligned} \frac{X_u}{m} &= -0.84 \quad [\text{sec}^{-1}] \\ \frac{X_w}{m} &= -0.32 \quad [\text{sec}^{-1}] \\ \frac{Z_u}{m} &= -0.58 \quad [\text{sec}^{-1}] \end{aligned}$$

$$
\begin{aligned}
\frac{Z_w}{m} &= -3.6 \quad [\text{sec}^{-1}] \\
\frac{Z_\delta}{m} &= 260 \quad [\text{m sec}^{-2}] \\
\frac{M_w}{B} &= -19.2 \quad [\text{m}^{-1}\text{sec}^{-1}] \\
\frac{M_q}{B} &= -32.5 \quad [\text{sec}^{-1}] \\
\frac{M_\delta}{B} &= 3100 \quad [\text{sec}^{-2}] \\
\frac{M_\nu}{B} &= 23.6 \quad [\text{sec}^{-1}] \\
\frac{M_{Aw}}{B} &= -31.0 \quad [\text{m}^{-1}\text{sec}^{-1}] \\
\frac{M_{Aq}}{B} &= -23.6 \quad [\text{sec}^{-1}] \\
\frac{M_{A\delta}}{B} &= 3100 \quad [\text{sec}^{-2}] \\
\frac{M_{A\nu}}{B} &= 23.6 \quad [\text{sec}^{-1}] \\
\frac{M_\eta}{B} &= 676 \quad [\text{sec}^{-2}] \\
\frac{M_\xi}{B} &= 329 \quad [\text{sec}^{-2}] \\
\frac{M_{A\xi}}{B} &= -329 \quad [\text{sec}^{-2}]
\end{aligned}
$$

The final quantity that must be evaluated is the torsional spring stiffness k. This is obtained by eliminating the flexible mode from the equations of motion, finding the rigid-body bending frequency ω_s, and using the frequency to obtain the spring stiffness through the equation $k = \omega_s^2 B_A$. If the torsional spring frequency is located near the rigid-body bending frequency, then it is much more likely that the spring frequency falls within the operational bandwidth of the control system, as the control system is initially design with controlling the rigid-body modes in mind, and the action of the control system with respect to the flexible mode is easier to view. The exact procedure is not detailed here, but the resulting value of the torsional spring stiffness is $k = 2742$ Nm. With these quanities, values of **A**, **B**, and **L** can be defined as follows:

$$\mathbf{A} = \begin{bmatrix} -.84 & -.32 & -29.4 & 0 & 0 & 0 \\ -.58 & 18.23 & 3.4 & 107.5 & -2195 & -12.04 \\ 0 & 0 & 0 & 1 & 0 & 0 \\ 0 & 23.6 & 0 & -17.8 & -1713.7 & 0 \\ 0 & 0 & 0 & 0 & 0 & 1 \\ 085.6 & 0 & 29.4 & -9628 & -47.2 & \end{bmatrix}$$

$$\mathbf{B} = \begin{bmatrix} 0 & 0 \\ 344.76 & -503.37 \\ 0 & 0 \\ 1352 & -1316 \\ 0 & 0 \\ 1352 & -1974 \end{bmatrix}$$

$$\mathbf{L} = \begin{bmatrix} 0 \\ -3.6 \\ 0 \\ -19.2 \\ 0 \\ 0 \end{bmatrix}$$

These are the state-space matrices that correspond to the geometry and flight conditions stated above. The system is now in the form required for application of the LQR control theory.

5.2.2 Modal Control Results

The modal control system of the towed aerodynamic vehicle was tested using two methods: by varying the flexibility of the vehicle about the nominal value ($k = 2742$) and observing the effects, and by observing the response of the system with and without feedback of the ξ control variable, i.e. with and without modal control.

An important assumption that was made for these tests was that the downwash from the forward annular wing did not hav an appreciable effect on the aerodynamics of the aft annular wing. This can be justified by the fact that the aft annular wing has a much greater cross-sectional area with respect to the flow than the forward wing, so the resulting effect of the vortex is small when compared to the effect of the rest of the incident airflow. The results of the downwash analysis for the maglev vehicle in Section 5.1.2 also support this assumption, as the downwash vortex has a small effect on that configuration, even though the geometries of the fore and aft wings are of comparable size.

The results of the comparison are shown in Figure 5-18, 5-19, and 5-20. Each figure shows the effect of adding the extra degree of control on the response from the vertical wind gust disturbance to the vertical velocity, and the results of varying the stiffness of the body are shown from figure to figure. The results are uniformly positive because the peak representing the flexible mode is damped consistently throughout all three cases. The effect of flexibilty is not as immediately apparent, however, and there is no noticeable effect on the controlled response.

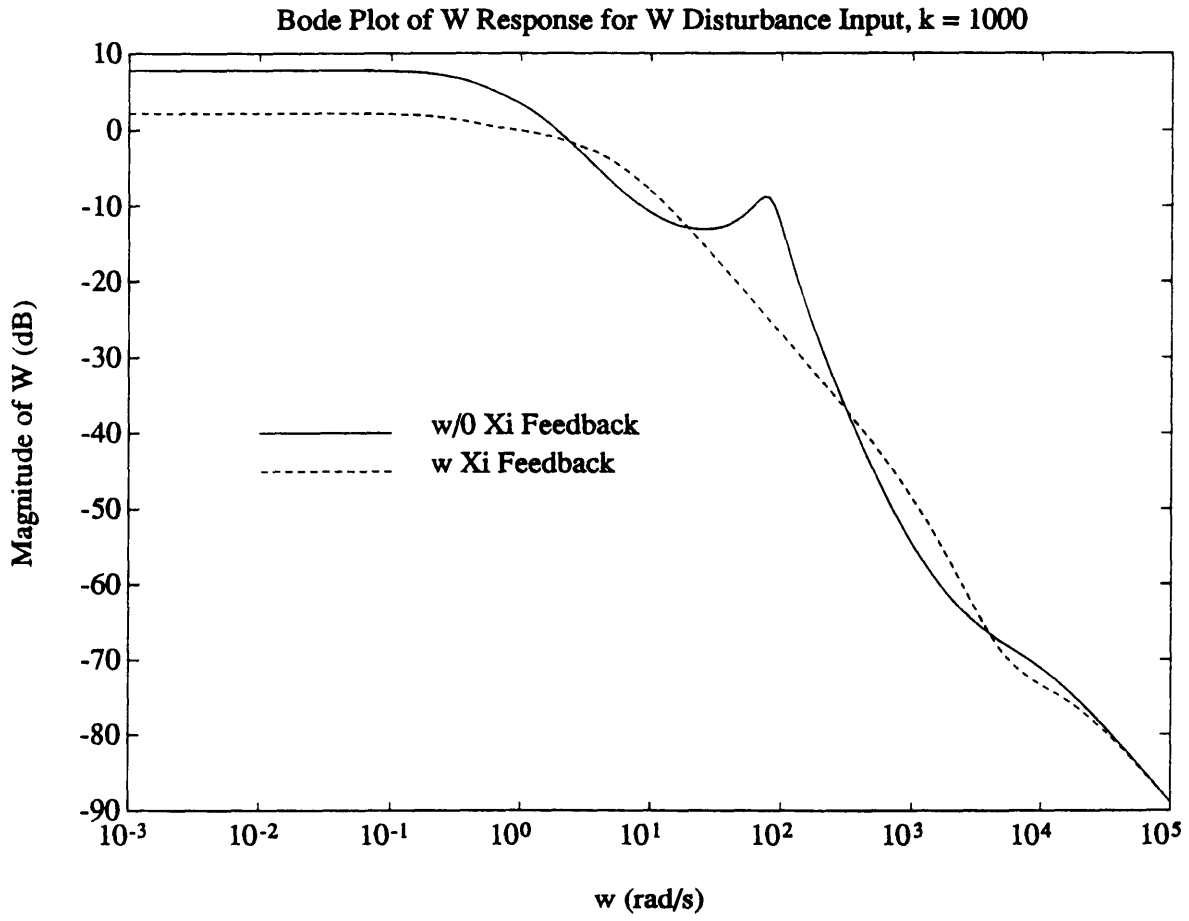

Figure 5-18: Towed Vehicle Modal Control Comparison, k = 1000

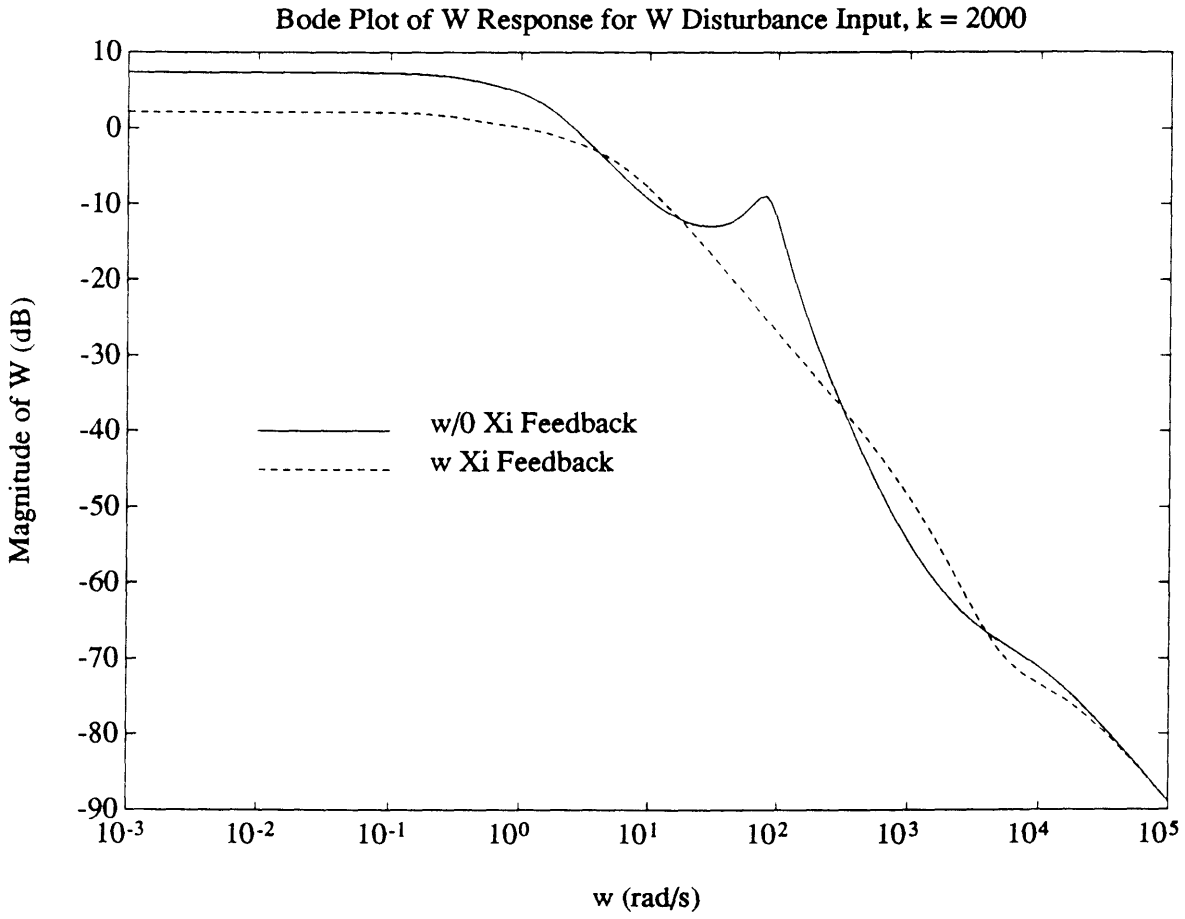

Figure 5-19: Towed Vehicle Modal Control Comparison, k = 2000

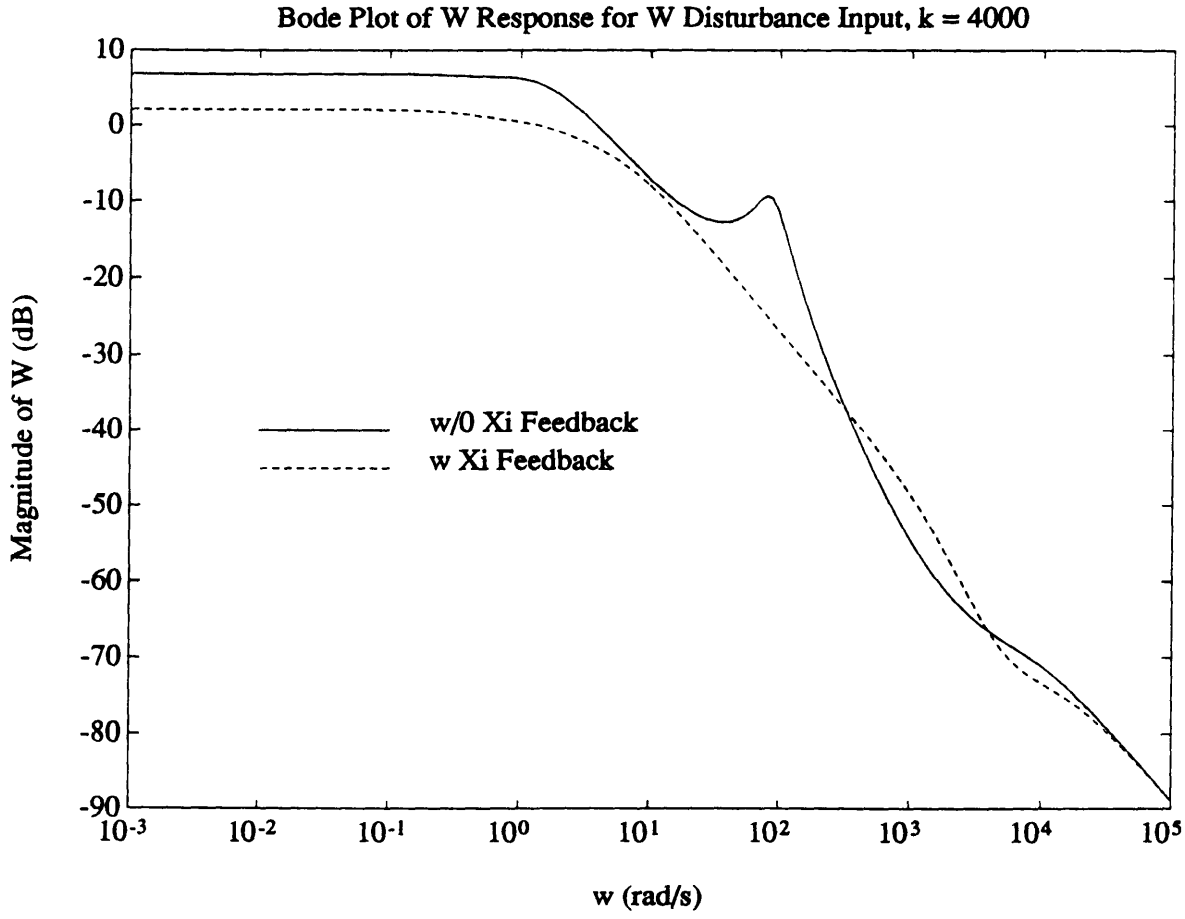

Figure 5-20: Towed Vehicle Modal Control Comparison, k = 4000

Chapter 6

Conclusions

6.1 Conclusion Concerning Modal Control

The issue of modal control as applies to two specific examples of aerodynamic vehicles having a flexible mode was addressed using simulations to model their dynamic behavior. The effectiveness of the modal control was evaluated for specific conditions imposed upon each system, with the results being generally positive. The control was implemented in each example in two ways: through state augmentation to include the degree of deflection and its rate so they would be included in the full-state feedback path of LQR controller, and by adding another control surface whose express purpose it to produce dynamics that control the flexible mode of the vehicle.

The maglev vehicle modal control evaluation consisted of two phases: examination of the aerodynamic properties of the lifting surfaces, and alteration of a previously existing non-linear dynamic simulation to include provisions for modal control. The aerodynamic results were compared with those used in the simulation, and showed good agreement when allowance was made for differences in the geometry. They were deemed adequate for purposes of evaluating the control system. The modified simulation was applied using the linear model of the vehicle dynamics to evaluate the controller performance and check its validity. The conclusion was that the implementation of the additional control surface was effective, and the general effect of the surface was to damp out the flexible longitudinal modes of the vehicle. Other tests

such as the issue of including the flexible states into the LQR cost functional and comparisons of the effects of changing the natural bending frequency of the vehicle did not produce results that were as substantially different, but did serve to show that the effect of the control implemented through additional feedback states and the additional control surfaces was positive.

The study of the towed vehicle dynamics also included the estimation of the aerodynamic properties of the lifting surfaces of the vehicle. The towed aerodynamic vehicle possessed annular surfaces, and the lifting characteristics of this configuration were analysed and compared with other predictions and measured results. The simulation model of the vehicle longitudinal dynamics including the bending mode was formulated. In the dynamic analysis of the towed vehicle, the aerodynamic lifting characteristics were included through the use of stability derivatives. The use of modal control in the towed vehicle proved equally effective in damping the flexible mode, also through the use of an additional control surface.

The issue of modal control of the first flexible mode is one that could find widespread applications, especially in the aerospace field. Proper control of flexible modes requires an idea of the types of motion that occur, and a means to restrict that motion, whether it be through mechanical (torsional spring) or aerodynamic means. Proper implementation gives the engineer control over more aspects of vehicle dynamics, and can therefore result in improved overall vehicle performance.

6.2 Further Work

Although the primary issue of modal control has been described, modelled, and shown to be effective, there are a number of modifications that could be incorporated in the maglev vehicle simulation to reflect the range of control surface geometries that are possible. If exacting specifications concerning the maglev vehicle aerodyanamics were desired, then a lifting-surface analysis of the aerodynamic characteristics is recommended because the current expression used to represent the lift-curve slope of the surfaces is empirical (See Equation 3.1 and [7]) and lifting-line theory is not entirely

appropriate for these surfaces because of their low aspect ratios [13].

Another possible area of expansion concerning modal control would be to attempt to use other types of control schemes, such as robust designs, where the control system would be made robust with respect to modelling errors, $\mathcal{H}_\infty$ designs, where the output of the system would be constrained to fall below a certain maximum gain, and designs were full-state feedback is either not required or not available, such as LQG ($\mathcal{H}_2$) designs or LQG/LTR designs [5], [6].

Appendix A

The integral that requires a solution is:

$$I_n = \int_0^{2\pi} \cos n\theta \cot \frac{\theta - \phi}{2} d\theta$$

This integral may be simplified by substituting $\theta - \phi = x$ and $d\theta = dx$ to obtain:

$$\begin{aligned} I_n &= \int_{-\phi}^{2\pi-\phi} \cos n(x+\phi) \cot\left(\frac{x}{2}\right) dx \\ &= \int_{-\phi}^{2\pi-\phi} \cos nx \cos n\phi \cot\left(\frac{x}{2}\right) dx - \int_{-\phi}^{2\pi-\phi} \sin nx \sin n\phi \cot\left(\frac{x}{2}\right) dx \\ &= \cos n\phi \int_{-\phi}^{2\pi-\phi} \cos nx \cot\left(\frac{x}{2}\right) dx - \sin n\phi \int_{-\phi}^{2\pi-\phi} \sin nx \cot\left(\frac{x}{2}\right) dx \end{aligned}$$

so,

$$I_n = I_1 - I_2$$

It is beneficial to evaluate I_2 first by defining $I_2 = \sin n\phi \; J_n$, where

$$J_n = \int_{-\phi}^{2\pi-\phi} \sin nx \cot\left(\frac{x}{2}\right) dx$$

A recurrance relation for $n \geq 3$ may be obtained as

$$J_n - J_{n-2} = \int_{-\phi}^{2\pi-\phi} \sin nx \cot\left(\frac{x}{2}\right) dx - \int_{-\phi}^{2\pi-\phi} \sin(n-2)x \cot\left(\frac{x}{2}\right) dx$$

and this relation can be transformed into the following integrals (See [14] for the details):

$$J_n - J_{n-2} = \int_{-\phi}^{2\pi-\phi} \cos nx \, dx + 2\int_{-\phi}^{2\pi-\phi} \cos(n-1)x \, dx + \int_{-\phi}^{2\pi-\phi} \cos(n-2)x \, dx$$

which, when integrated, produces a result of $J_n - J_{n-2} = 0$ [14] . Therefore, there are no higher-order terms of J_n, and the only term present is

$$\begin{aligned} J_1 &= \int_{-\phi}^{2\pi-\phi} \sin x \cot\left(\frac{x}{2}\right) dx \\ &= 2\pi \end{aligned}$$

so, $I_2 = 2\pi \sin n\phi$. Now, as for I_1, one can define $I_1 = \cos n\phi \; K_n$, where

$$K_n = \int_{-\phi}^{2\pi-\phi} \cos(n-2)x \cot\left(\frac{x}{2}\right) dx$$

A recurrance relation for K_n for $n \geq 3$ can also be derived [14]:

$$K_n - K_{n-2} = \int_{-\phi}^{2\pi-\phi} \cos nx \cot\left(\frac{x}{2}\right) dx - \int_{-\phi}^{2\pi-\phi} \cos(n-2)x \cot\left(\frac{x}{2}\right) dx$$

and, as before, this integral results in the expression $K_n - K_{n-2} = 0$. The first term K_1, is derived from the expression:

$$\begin{aligned} K_1 &= \int_{-\phi}^{2\pi-\phi} \cos x \cot\left(\frac{x}{2}\right) dx \\ &= \int_{-\phi}^{2\pi-\phi} \cot\left(\frac{x}{2}\right) dx - \int_{-\phi}^{2\pi-\phi} \sin x \, dx \\ &= K_{11} + K_{12} \end{aligned}$$

The solution to K_{12} is $K_{12} = 0$ [14], but the solution to K_{11} is much more involved, as there is a singularity at $x = 0$ that must be integrated around, if $y = x/2$ and $dx = 2dy$:

$$K_{11} = 2\int_{-\phi/2}^{\pi-\phi/2} \cot y \quad dy$$

$$
\begin{aligned}
&= 2\int_{-\phi/2}^{0} \cot y \, dy + 2\int_{0}^{\phi/2} \cot y \, dy + 2\int_{\phi/2}^{\pi-\phi/2} \cot y \, dy \\
&= 0 + 0 + 2\left[\ln \sin y\right]_{\phi/2}^{\pi-\phi/2} \\
&= 0
\end{aligned}
$$

so, the final result is:

$$I_n = -2\pi \sin n\phi$$

Appendix B

```
C     Program 'Vortex1'
C     Programmmed by Ed Walters

      real r,g,vinf,a0,th0,x0,xe,pi
      integer n
      real a(300),th(300),x(300),abar(300),xbar(300)
      open(unit=15,file='vort.inp',status='old')
      open(unit=16,file='vort.out',status='new')
      read (15,10) r,g,vinf,a0
10    format (f5.2,1x,f7.3,1x,f7.3,1x,f5.2)
      read (15,20) th0,x0,xe,n
20    format (f5.2,1x,f5.2,1x,f7.2,1x,i4)
      pi = acos(-1.)
      print *,r,g,vinf,a0,th0,x0,xe,n
      do 25 i = 1,200
          xbar(i) = x(i)/r
          abar(i) = a(i)/r
25    continue
      call heun(xbar,abar,th,x0,a0,th0,xe,n,r,g,vinf,pi)
      write(16,30)
30    format(9x,'x',15x,'a',13x,'theta',/)
      do 45 i = 1,200
```

```
        write (16,40) xbar(i),abar(i),th(i)
40      format (e15.5,1x,e15.5,1x,e15.5)
45  continue
    end

    subroutine heun(xbar,abar,th,x0,a0,th0,xe,n,r,g,vinf,pi)
    real abar(300),xbar(300),th(300)
    real x0,xe,th0,a0,dx,dal,dthl,dar,dthr,ar,thr,f1,f2
    xbar(1) = x0/r
    abar(1) = a0/r
    th(1) = th0
    dx = (xe - x0)/(n*r)
    do 50 i = 1,n
        xbar(i+1) = xbar(i) + dx
        dal = f1(xbar(i),abar(i),th(i),r,g,vinf,pi)*dx
        dthl = f2(xbar(i),abar(i),th(i),r,g,vinf,pi)*dx
        ar = abar(i) + dal
        thr = th(i) + dthl
        dar = f1(xbar(i+1),ar,thr,r,g,vinf,pi)*dx
        dthr = f2(xbar(i+1),ar,thr,r,g,vinf,pi)*dx
        abar(i+1) = abar(i) + .5*(dal+dar)
        th(i+1) = th(i) + .5*(dthl+dthr)
50  continue
    return
    end

    function f1(xbar,abar,th,r,g,vinf,pi)
    real f1,xbar,abar,th,u1bar,u2bar,u3bar,phi,r,g,vinf,pi
    real d1bar,d2bar,d3bar,nu
```

```
      f1 = 0
      return
      end

      function f2(xbar,abar,th,r,g,vinf,pi)
      real f2,xbar,abar,th,u1bar,u2bar,r,g,vinf,pi
      real d1bar,d2bar,nu
C     print *,xbar
      d1bar = (abar**2 - 1)/abar
      d2bar = abar
      nu = g/(4.*pi*r*vinf)
      u1bar = nu*(1+xbar/sqrt(xbar**2+d1bar**2))/d1bar
      u2bar = nu*(1+xbar/sqrt(xbar**2+d2bar**2))/d2bar
      f2 = (u1bar - u2bar)/abar
      return
      end
```

Bibliography

[1] E. Livine, L. A. Schmidt, and P. P. Friedmann. Exploratory design studies of actively controlled wings using integrated multidisciplinary synthesis. *AIAA Journal*, May 1992.

[2] E. Livine, L. A. Schmidt, and P. P. Friedmann. Towards integrated multidisciplinary synthesis of actively controlled fiber composite wings. *Journal of Aircraft*, December 1990.

[3] Tokio Yamamoto. Impact of aircraft structural dynamics on integrated control design. In *Proceedings of the AIAA Guidance, Navigation, and Control Conference*, number AIAA Paper 83-2216, 1983.

[4] Various Authors. Magneplane in-progress review. Technical report, Magneplane International, March 1992.

[5] D. O. Anderson and J. B. Moore. *Optimal Control: Linear Quadratic Methods.* Prentice-Hall, 1990.

[6] Brian L. Stevens and Frank L. Lewis. *Aircraft Control and Simulation.* John Wiley and Sons, 1992.

[7] R. L. Bisplinghoff, H. Ashley, and P. L. Halfman. *Aeroelasticity.* Addison-Wesley, 1955.

[8] Arnold M. Kuethe and Chuen-Yen Chow. *Fundamentals of Aerodynamics.* John Wiley and Sons, third edition, 1986.

[9] John J. Bertin and Michael L. Smith. *Aerodynamics for Engineers.* Prentice-Hall, 1979.

[10] S. Hoerner and Burst H. *Fluid-Dynamic Lift.* Hoerner, second edition, 1985.

[11] H. Glauert. *The Elements of Airfoil and Airscrew Theory.* Cambridge, second edition, 1948.

[12] L. M. Milne-Thompson. *Theoretical Aerodynamics.* MacMillan, fifth edition, 1968.

[13] Schlichting and Truckenbrodt. *Aerodynamics of the Airplane.* McGraw-Hill International, 1979.

[14] Roger Lair Smith. *Aerodynamics of Channel and Ring Wings.* PhD thesis, University of Oklahoma, 1973.

[15] H. S. Ribner. The ring wing in nonaxial flow. *J. Aero. Sciences, Vol. 14*, September 1947.

[16] Johannes von Weissinger. Einige eigebrisse aus der theorie des ringflugels in inkompressibler stromung. *Advances in Aeronautical Sciences*, 1959.

[17] B. W. McCormick. *Aerodynamics of V/STOL Flight.* Academic Press, 1985.

[18] Francois Lammare and Ion Paraschivoiu. Efficient panel method for vortex sheet roll-up. *Journal of Aircraft*, February 1992.

[19] H. S. Fletcher. Experimental investigation of lift, drag, and pitching moment of five annular airfols. Technical Report 4117, NACA, 1957.

[20] Michael Judd. Personal communication. January 1993.

[21] Timoschenko S., D. H. Young, and W. Weaver. *Vibration Problems in Engineering.* John Wiley and Sons, 1974.

[22] Bernard Etkin. *Dynamics of Flight Stability and Control.* John Wiley and Sons, second edition, 1982.

[23] A. E. Bryson and Y. Ho. *Applied Optimal Control.* John Wiley and Sons, 1975.

[24] G. J. Borse. *Fortran 77 and Numerical Methods for Engineers.* PWS-KENT Publishing, second edition, 1991.